UNIVERSITY OF OKLAHOMA

GRADUATE COLLEGE

WIRELESS OPTICAL TRANSCEIVER DESIGN, LINK ANALISYS AND ALIGNMENT CONTROL FOR MOBILE COMMUNICATION

A DISSERTATION

SUBMITTED TO THE GRADUATE FACULTY

in partial fulfillment of the requirements for the

Degree of

DOCTOR OF PHILOSOPHY

By

DAYONG ZHOU
Norman, Oklahoma
2013

WIRELESS OPTICAL TRANSCEIVER DESIGN, LINK ANALISYS AND ALIGNMENT CONTROL FOR MOBILE COMMUNICATION

A DISSERTATION APPROVED FOR THE
SCHOOL OF ELECTRICAL AND COMPUTER ENGINEERING

BY

Dr. Hazem H. Refai, Chair

Dr. Peter G. LoPresti, Co-chair

Dr. William O. Ray

Dr. Curt Adams

Dr. James J. Sluss, Jr.

Dr. Thordur Runolfsson

Table of Contents

List of Tables

List of Figures

Abstract

Pointing, acquisition and tracking of a free-space optical node in a mobile network experiencing misalignment due to adverse factors including vibration, motion and atmospheric turbulence requires a different approach than traditional free-space optical transceivers. A recent fiber-bundle approach for beam steering at the transmitter was investigated to provide continuous beam coverage at the receiver without the application of mechanical devices. Utilizing multiple fibers-lenses sets at the receiver was also proposed to enhance the tolerance of optical link misalignment. In this work, both laboratory experiments and software simulation were implemented to evaluate the optical link performance for different fiber-bundle-based transceiver setups as the link parameters were varied. The performance was evaluated in terms of the coverage area at the receiver, which is a measure of misalignment tolerance and is dependent not only on wavelength but on other key parameters such as link length, transmitted power, the pattern of transmitters, beam divergence, and the receiver construction. The results showed that fiber-bindle-based transceivers reveal significant potential to maximize the up time of the link, and the results also provide guidance on the further development of the overall system. To incorporate the proposed transceiver designs, an alignment control system was developed and evaluated as well. The laboratory results show that the optical control system successfully recovered and maintained the link while the receiver was in motion and the signal coverage at the target area was enhanced significantly.

Chapter 1

Introduction

1.1 Statement of Problem

Free-space optical (FSO) communication can provide a way to establish high-bandwidth links for a variety of applications, including inter-satellite communication, airborne internet, and inter-building communication in urban settings: the latter is commercially available for a range of distances and system requirements [1-3]. In addition to the bandwidth advantages, FSO also provides advantages in security and compatibility with existing systems. Due to the tight alignment requirements for FSO links, it is very difficult to either intercept an FSO signal or to interfere with its transmission without detection by the transceivers or the operators of the link [4]. Therefore, FSO enhances the security of the network. Since FSO operates at optical frequencies, there is little chance of an FSO network interfering with native cellular and other RF networks in the deployment area.

The requirement for high alignment accuracy of the transmitter and receiver to establish a valid link has provided a hurdle to extending the application of FSO networks to a mobile environment, where one or both of the nodes are in motion. The combination of motion with the usual errors associated with pointing, acquisition and tracking devices and vibrations in the physical system produce alignment errors that must be overcome. Other investigators have addressed the problem in cases where the motion was well described by a combination of statistical models (for vibrations) and motion equations

(e.g. satellite trajectories), and the motion was small enough that large, quick positioning modification were not necessary [2, 3, 5].

The size and weight of current long-distance transceivers is another problem impeding the adoption of mobile FSO. A typical commercial system uses a pair of telescopes with large collecting lenses and long focal lengths, and large mechanical systems for stabilizing and pointing the transceivers, all of which add significant size and weight to the system, not including the electronics and the power systems. Some success in this area has been achieved over short distances with advances in "smart dust" technology, where a small optical transmitter and receiver have been integrated onto platforms of one cubic inch in volume. Small, short-distance multi-directional transmitters and receivers have also been tested with some success for mobile communication at lower data rates [6-8]. To date, these systems have limited range and flexibility, and are not suitable for the applications targeted here.

The work described here focuses on building hybrid FSO/RF networks with mobile nodes which require new transmitter and receiver designs that allow a link to remain viable over long distances and given rapid positioning changes. The size and weight of FSO transceivers must be reduced significantly for use in airborne platforms. To accomplish this, it is necessary to develop a transceiver system that is capable of providing sufficient power over a large target area – referred to here as the effective beam coverage – to ensure the link is not disconnected as the transceivers move.

1.2 Summary of Approach

Increasing the effective beam coverage is achieved by making modifications to both the transmitter and the receiver design. At the transmitter, the number of fibers that are transmitting, the beam divergence, and methods for non-mechanical beam steering within a small physical space are all key factors. At the receiver, designs that improve the angular and transverse misalignment provide flexibility in design by providing a sufficient link budget over a larger spatial volume. Earlier work along these directions has demonstrated the promise of the approach [9-12]. Despite these developments, an alignment control system is still required to point the transmitter and receiver in the general direction of each other and to provide fine adjustments to both acquire and maintain the link connectivity.

1.3 Objective

In this wok, experiments and simulation are carried out on a FSO system that combined the novel transmitter and receiver designs discussed and demonstrated individually in past work. Multiple fibers are implemented at the transmitter along with a specifically chosen lens to illuminate a larger area at the target (with all fibers carrying light) or to allow switching of the light from one area to another to track movement of the receiver. The optical parameters that produce the best balance of spatial coverage and range over which the link is viable are explored. A prototype receiver using multiple lens-fiber pairs is used to maximize the ability to collect sufficient optical power to maintain the link despite errors in the alignment between the receiver and transmitter, and thus work with the transmitter design to further increase the working range of the

transceiver system. The interaction of the various design parameters is investigated and demonstrated. To ensure the valid optical link, a link alignment control system is to be proposed and evaluated for accomplishing acquisition and tracking.

Chapter 2 covers the basic concepts and formulas underlying the system design; evaluation of the wireless fiber-bundle-based transceivers and link analysis are presented in Chapters 3 and 4; the attendant mobile transceiver alignment control system is introduced and evaluated in Chapters 5 and 6; Chapter 7 states the conclusions.

Chapter 2

Background

Before the further details of this research in FSO mobile transmitter design are presented, it is necessary to ensure that the reader is provided enough information on background material relevant to this thesis.

2.1 Overview of DAWN System

Recent disastrous events, most notably 9/11 and several major hurricanes have highlighted the vulnerability of the current telecommunications infrastructure to man-made and natural catastrophes. Overwhelming destruction and the subsequent loss of services significantly disrupted or destroyed critical resources and subsequently caused communications systems to fail. These failures highlighted the vulnerability of the telecommunications infrastructure and clearly identified the need for a rapidly deployable communications system to be used in the disaster affected area to support the rescue and recovery efforts. With the destruction of cellular towers, underground coax cables and optical fibers, and telecommunications switches and offices, communication when it is much needed comes to a halt. Lack of communication during disaster recovery efforts can result in a delayed and inefficient rescue and recovery effort that has the potential to increase the probability of loss of lives.

The focus of the ongoing work is the investigation and implementation of a disaster area wireless network (DAWN) using a hybrid free space optical and RF communication systems to provide communication immediately after a natural or

manmade event. FSO is capable of providing high bandwidth, secure, and interference hardened communication, while RF wireless accommodates terminal mobility in the era of portable and pervasive computing. DAWN technology uses helium-filled balloons, securely tethered to the ground, or rapidly deployable towers, to rapidly launch a wireless mesh network and establish communication over the affected area. It uses WiFi technology and widely available WiFi-based applications to provide voice, video, and data communication capabilities to mobile terminals on the ground. It also uses FSO technology to establish an optical backbone between balloons for aggregating and hauling traffic generated in the RF network to the Internet. Connection to the Internet is established by either an FSO terminal or an optical fiber.

Investigations into the hybridization of FSO and RF technology have been performed by various investigators. A portion of this work has been focused on the provisioning of carrier class FSO service through the provisioning of complementary RF links [13]. Through this work, it has been demonstrated that using hybrid FSO/RF technology greatly increases the availability of such a communications system. The increased availability of a hybrid FSO/RF system lends itself to deployment in disaster recovery situations in which the high data rate of FSO coupled with the increased reliability and broadcast nature of RF systems can be used to implement a temporary communications infrastructure. Further work that demonstrates the suitability of hybrid FSO/RF technologies for tactical operations has shown that the two technologies complement each other well as well as introducing several areas of topology control that need to be addressed in order to integrate FSO and RF technologies successfully [14]. Demonstration of hybrid FSO/RF communications links over time periods of up to two

years have been reported [15]. Results such as these further demonstrate the promise of this hybrid technology for disaster communications. However, extensive research is still required to transition from a permanent FSO/RF link to a temporary FSO/RF link in which permanent power needs to be replaced by battery power supplies. The airborne nature of disaster communications systems also needs to be investigated, along with the investigation of methods to tie a temporary disaster communication area back into fully operational backbone networks. It is noted that even though FSO/RF hybrids will provide excellent coverage for a disaster area, coordinators of the relief efforts are not necessarily stationed in the immediate area, so integration of the temporary communications structure to the undamaged infrastructure is essential.

2.2 Basic Optical Link Concepts

2.2.1 SONET

Synchronous optical networking (SONET) is a multiplexing protocol for transferring multiple digital bit streams using lasers or light-emitting diodes (LEDs) over the same optical fiber. The method was developed to replace the Plesiochronous Digital Hierarchy (PDH) system for transporting larger amounts of telephone calls and data traffic over the same fiber wire without synchronization problems [16]. SONET protocol is widely used in the U.S. and also utilized in the experiments conducted as part of this research.

SONET uses a basic transmission rate, called the synchronous transport signal level-1(STS-1) that is equivalent to 51.84 Mb/s. Higher-rate signals (STS-*N*) are *N* integer multiples of the STS-1 rate. For example, STS-3 rate is 155.52 Mb/s which is

three times the rate of STS-1[17]. STS is an electrical signal which may exist only in SONET equipment. The interface to other equipment is usually a scrambled version of the STS signal in optical form. The optical form corresponding to the STS-*N* rate is called OC-*N* (optical carrier-*N*). The common SONET rates are shown in Table 2.1. Other rates (OC-9, OC-18, OC-24, OC-36, and OC-96) are referenced in some of the standards documents but were never widely implemented [18].

Optical Level	Electrical Level	Bit Rate (Mb/s)
OC-1	STS-1	51.84
OC-3	STS-3	155.52
OC-12	STS-12	622.08
OC-48	STS-48	2488.32
OC-192	STS-192	9953.28
OC-768	STS-768	39,813.12

Table 2.1: SONET Rates

The SONET layer consists of four sublayers—the path, line, section, and physical layers. Figure 2.1 shows the top three layers. The path layer is SONET's highest level layer. It takes data to be transmitted and transforms it into signals required by the line layer, and adds or modifies the path overhead bits for performance monitoring and protection switching. The line layer ensures reliable transport of the payload and overhead generated by the path layer. It provides synchronization and multiplexing for multiple paths and modifies overhead bits relating to quality control. The section layer is concerned with generating proper STS-*N* frames which are to be transmitted across the

physical medium. It addresses issues such as proper framing, error monitoring, section maintenance and orderwire. The physical layer is SONET's lowest level layer. It deals directly with transmitting the bits on the physical medium. It creates the proper optical carrier format signals from the electrical STS signals used in the other layers. It concerns itself with low-level issues such as pulse shaping, power levels, and wavelength [19].

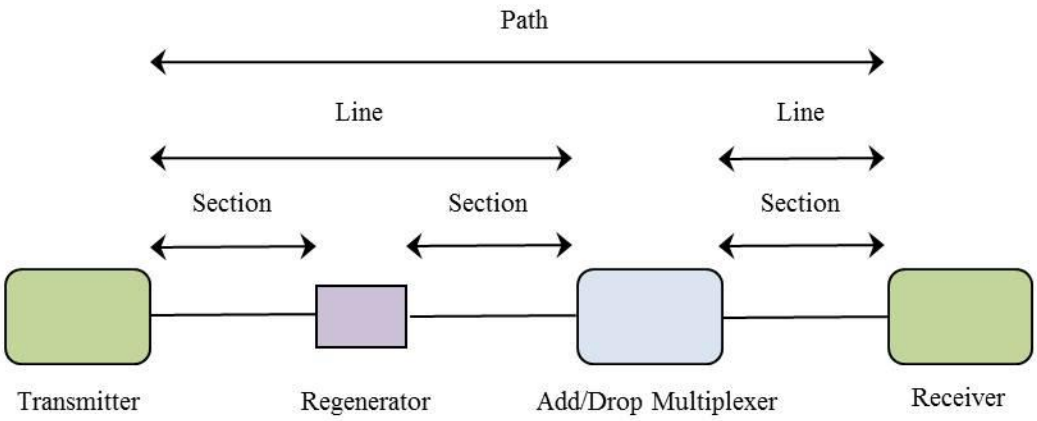

Figure 2.1: SONET Layers

A SONET STS-*N* frame is obtained by byte-interleaving N STS-1 frames, as shown in Figure 2.2. A standard STS-1 frame is 125μs in duration and consists of 810 bytes, conceptually arranged in a two-dimensional matrix. Each column of the matrix is 9 bytes high, and each row of the matrix is 90 bytes wide [19]. The first three columns of the frame contain the transport overhead that includes section and line overhead bytes. The remaining columns are used for the data payload bytes which include one column of the path overhead bytes [20]. Overhead bytes provide key management functions that allow simpler multiplexing and greatly expanded operations, administration, maintenance, and provisioning capabilities [17].

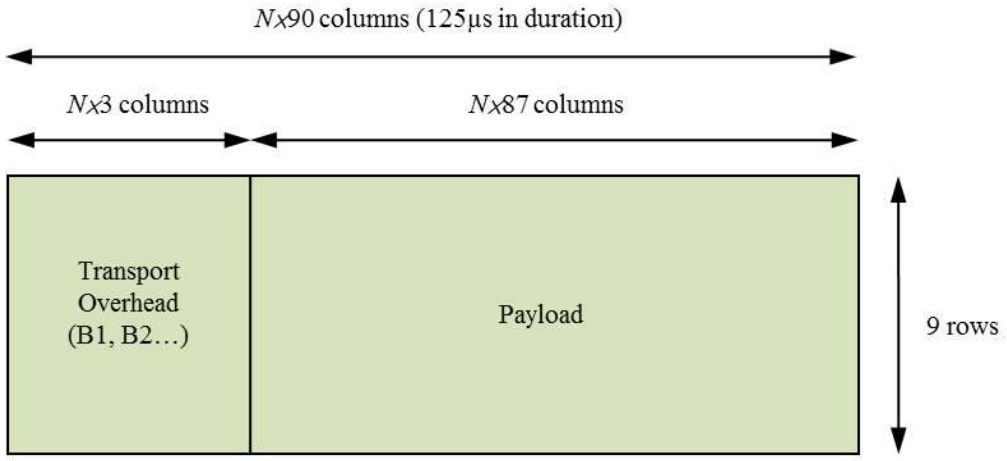

Figure 2.2: SONET Frame Structure

Since in the laboratory experiments there were no other line terminations in use between transmitter and receiver, monitoring the statistics of the B2 byte, a line overhead byte, was chosen to check the link error rate.

2.2.2 BER, BBER and BERT

In telecommunication transmission, the bit error rate (BER) is the percentage of bits that have errors relative to the total number of bits received in a transmission, usually expressed as ten to a negative power. For example, a transmission might have a BER of 10 to the minus 6, meaning that, out of 1,000,000 bits transmitted, one bit was in error [21]. The BER is the key performance attribute in a viable communication link, and a smaller number is better. In a SONET frame, the B2 byte consists of parity check bits by which the bit error rate (BER) can be computed. Each bit of the B2 byte is computed by performing a parity check over all of the corresponding bits in each byte of the payload. In a manner similar to the BER, the byte bit error rate (BBER) is defined as the

percentage of bits in the B2 byte that have errors relative to the total number of bits received in B2 bytes. Since the B2 byte is a measure of the error rate in the line, the BBER is a close measure of the base BER of the link.

A BERT (bit error rate tester) is a device that measures the BER or BBER for a given transmission. The BERT produces a randomized signal for the data stream, inserts this data into a SONET frame, transmits the data, and then analyzes the return signal using the SONET standard measures. The BERT used in the experiments also provides measurement of the received average power, which is often an easier reference point to use in setting up an experiment than the BBER.

2.2.3 Single-mode Fiber vs. Multi-mode Fiber

Single-mode fiber is a dielectric waveguide that has a small light carrying core of 8 to 10 microns in diameter, and allows only one solution (i.e. one mode) of the electromagnetic equations to propagate for a given wavelength range. It is normally used for long distance transmissions with laser diode based fiber optic transmission equipment [22]. Single-mode fibers can have a higher bandwidth than multi-mode fibers [23]. Multi-mode fiber has a relatively large light carrying core, usually 62.5 microns or larger in diameter, and thus allows multiple solutions (modes) to propagate. It is usually used at receiving end to capture more light or used for short distance transmissions with LED based fiber optic equipment.

2.2.4 Switch and Coupler

Figure 2.3: Optical Switch and Coupler

In fiber optics, an optical switch is a switch that enables signals in optical fibers to be selectively switched between fibers. A fiber optic coupler is a device that can distribute the optical signal (power) from one fiber among two or more fibers [24]. A fiber optic coupler can also combine the optical signal from two or more fibers into a single fiber. Fiber optic couplers attenuate the signal delivered to an output port much more than an optical switch because the input signal is divided among the output ports. For example, with a fiber optic coupler, each output is no more than one-half the power of the input signal (a 3 dB loss). By comparison, a switch can easily have a loss of only a few tenths of a dB or less between the input port and the selected output port. Figure 2.3 shows a 1 ×2 switch and a 1 ×2 coupler.

2.3 Optical Propagation

2.3.1 Transmitter Lens

At a standard FSO transmitter, the optical components consist of a single-mode fiber cable and a collimating lens. The divergence of the transmitted optical beam depends on the distance z_{fl} between the end of the fiber and the lens, the focal length f of the lens, and the initial field distribution at the end of the fiber. Using an appropriate

degree of divergence in the transmitter can optimize the beam area at the receiver assuming the distance to the receiver and the power budget of the link are known [25].

The fiber tip is usually placed inside the focal length of the transmitter lens. There are two main reasons for this. First, it is easy to control the divergence angle θ_d by changing z_{fl}. For a biconvex lens, as shown in Figure 2.4, when the light source is inside the lens' focal length, the beam divergence increases as the light source gets closer to the transmitter lens. Second, it is unreasonable to place the light source right on or outside the lens' focal point in our transmitter design. When the light source is right on the focal point, ideally there is no beam divergence in propagation and the actual beam coverage is not large enough to catch a moving receiver in our case. When the light source is outside the focal length, the propagating beam is gathering somewhere on the axis behind the lens and the high intensity of gathering point may cause nonlinear effects in air. Also, depending on the lens parameters chosen, the overall length of the transmitter system can become large which could be detrimental in practical applications.

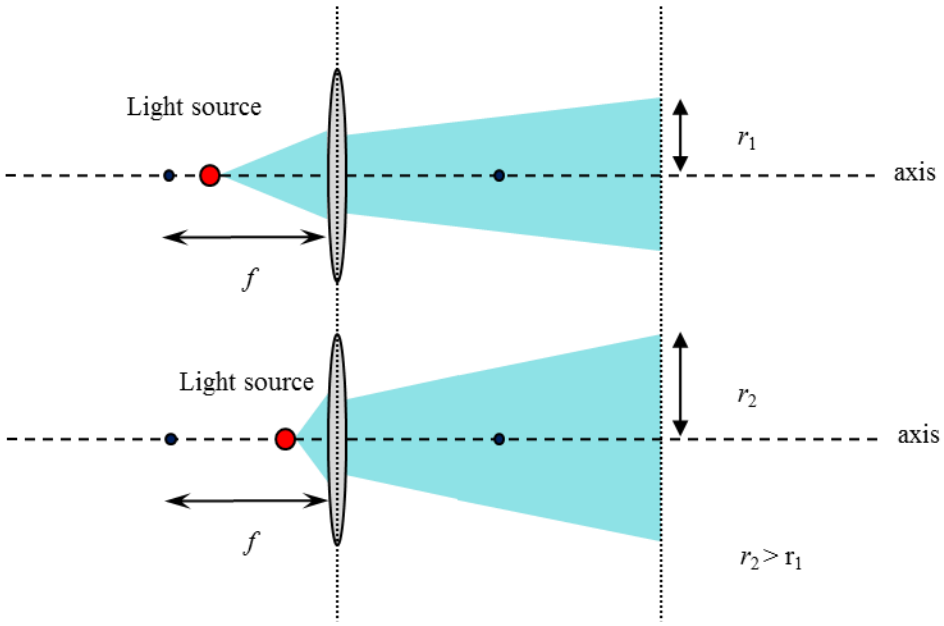

Figure 2.4: Beam Divergence

The power at any point beyond the lens depends on the divergence, the field distribution, and the initial power P_i at the end of the fiber. As the field distribution at the output of a single-mode optical fiber closely approximates a Gaussian profile, the theory of Gaussian beam propagation is used to analyze the output of the module.

2.3.2 Transmission

Using Gaussian beam propagation theory [26], the distribution of optical intensity *I* at any point *z* from an initial collimated point is given by

$$I(r) = \frac{2P_i}{\pi w} \exp(-2r^2 / w^2) \tag{2.1}$$

where *w* is the beam waist and *r* is the radial distance from the optical axis. The beam waist and the radius of curvature *R* of the optical beam for any distance *z* are given by

$$w(z) = w_o \left[1 + \left(\frac{\lambda z}{\pi w_o^2} \right)^2 \right]^{\frac{1}{2}} \tag{2.2}$$

$$R(z) = z \left[1 + \left(\frac{\pi w_o^2}{\lambda z} \right)^2 \right] \tag{2.3}$$

where w_o is the beam waist where R is infinite (the beam is collimated). The distance z is equal to zero at w_o. For the transmitter, w_o occurs at the output plane of the fiber. The typical value of w_o is 5.2 m for standard single-mode fiber (Corning SMF-28).

The ABCD law for Gaussian beams is then used to propagate the beam through the collimating lens. The transfer matrix for a biconvex lens with focal length f is

$$\begin{bmatrix} A & B \\ C & D \end{bmatrix} = \begin{bmatrix} 1 & 0 \\ -1/f & 1 \end{bmatrix}. \tag{2.4}$$

The transfer matrix is applied to the parameter $q(z)$ of the Gaussian beam, given by

$$q(z) = \left(\frac{1}{R(z)} - i \frac{\lambda}{\pi w^2(z)} \right)^{-1}. \tag{2.5}$$

The relationship between the value of $q(z)$ at the input to the lens q_1 and the value at the output of the lens q_2 is given by

$$q_2 = (Aq_1 + B)/(Cq_1 + D). \tag{2.6}$$

Using equations (2.5) and (2.6) with the matrix elements in equation (2.4), the relationships between the input values of the beam waist and curvature (w_1, R_1) and the values w_2 and R_2 after the lens are

$$R_2 = \left(R_1^{-1} - f^{-1} \right)^{-1}, \quad w_2 = w_1. \tag{2.7}$$

To propagate the beam beyond the lens using equations (2.2) and (2.3), the new values of w_{OL} and z_2 for the effective collimation (image) point of the lens (see Figure 2.5) are calculated from R_2 and w_2. Performing this operation gives

$$w_{OL} = \frac{w_2}{\sqrt{(\pi^2 w_2^2 / \lambda^2 R_2^2) + 1}} \approx \frac{R_2 \lambda}{\pi w_2} ,$$
$$z_2 = \frac{\pi w_{OL}^2}{\lambda} \left((w_2^2 / w_{OL}^2) - 1 \right)^{\frac{1}{2}} . \tag{2.8}$$

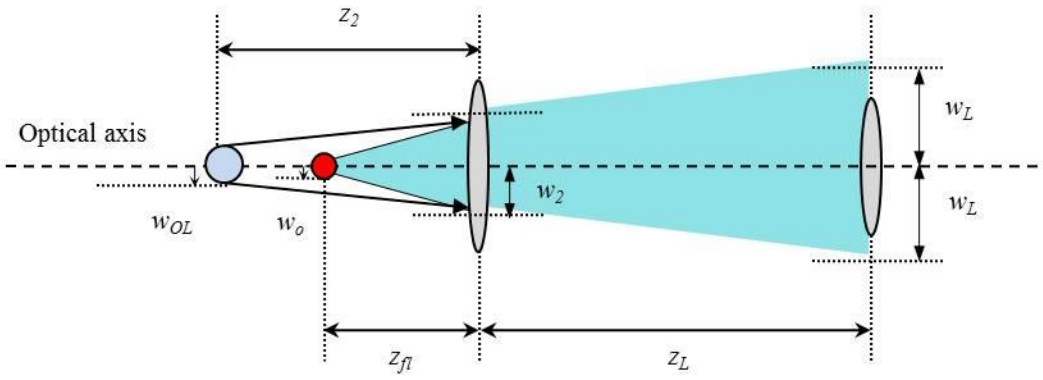

Figure 2.5: Basic Geometry for the Beam Propagation Calculations

For most conditions, $\pi^2 w_2^2 / \lambda^2 R_2^2 >> 1$, and therefore the approximate expression for w_{OL} is used without contributing significant error. Combining equations (2.2) and (2.8) gives the equation for the beam waist w_L at any distance z_L from the lens

$$w_L(z_L) = w_{OL} \left(1 + \left(\frac{\lambda (z_2 + z_L)}{\pi w_{OL}^2} \right)^2 \right)^{\frac{1}{2}} . \tag{2.9}$$

The divergence angle θ_d of the beam after the lens can then be calculated by

$$\theta_d = \frac{\lambda}{\pi w_{OL}} \tag{2.10}$$

2.3.3 Power Collected by Receiver Lens

At the receiver, a lens is used to collect the optical power and focus it onto the receiving fiber. The amount of power collected depends on the radius of the lens and the intensity distribution of the optical beam over the area of the lens. From equations (2.1) and (2.9), the intensity distribution at a distance z_L between the transmitting lens and the receiving lens is given by

$$I(r) = \frac{2P_i}{\pi w_L^2} \exp(-2r^2 / w_L^2). \tag{2.11}$$

The power collected by the receiving lens, assuming minimal effects from diffraction, is then given by

$$P_{collected} = \iint_{Lens\ Area} I(r)\, r\, dr\, . \tag{2.12}$$

If the power collected by the receiving lens is sufficient for the receiver to achieve a desired bit-error rate, then a link can be established.

2.3.4 Coupling into Fiber

The environment for this calculation is shown in Figure 2.6. The optical beam emitted by an FSO transmitter arrives at the receiver at an angle to the optical axis of the receiver, either through physical misalignment or deflection due to turbulence.

For practical transmitters, this is a Gaussian beam of the form

$$E_{in} = E_o \sqrt{\frac{2}{\pi}} \frac{w_o}{w_L} \exp\left[ik(x^2 + y^2)/2R_L\right] \cdot \exp\left[-(x^2 + y^2)/{w_L}^2\right] \tag{2.13}$$

where w_L is the e^{-1} waist at a distance z_L from the original focal plane (radius of curvature R = ∞) and where w_o is the initial beam waist. The Gaussian beam has a curved wave front with a radius of curvature R_L.

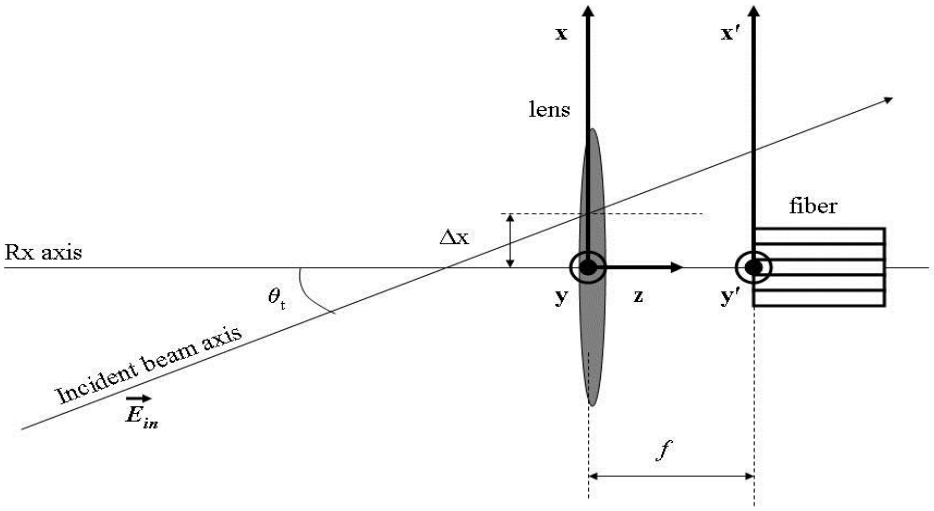

Figure 2.6: Coupling into Fiber [27]

At the receiver, for initial analysis, the beam is assumed to enter at a deflection angle θ_t with the x-axis only, with its propagation parallel to the x-z plane.

The collecting lens intersects a portion or the entire transmitted beam and concentrates that portion of the light into a focal spot, ideally on the core of the collecting fiber or fiber bundle.

When z_L is very large, w_L can be much larger than the radius of the collecting lens. In this case, the Gaussian beam can be approximated closely as a plane wave. For the plane wave, the field equation under the condition in Fig. 2.6 is given simply by

$$E_{in} = E_Z \exp(ik \sin(\theta_t)) \exp(ik \cos(\theta_t)) \tag{2.14}$$

where E_z is the field amplitude and θ_t is the tilt angle with respect to the x axis. To find the transfer function of the lens, the phase retardation of the lens is calculated. Since the beams under study enter the lens at an angle and intersect the entire lens area, the full geometrical effects of the lens are considered, resulting in a phase retardation given by

$$\phi_{lens} = (2\pi / \lambda) * \{z_o + (n-1)(z_o - R_1[1 - \sqrt{1 - \rho^2 / R_1^2}] - R_2[1 - \sqrt{1 - \rho^2 / R_2^2}])\} \tag{2.15}$$

where z_o is the maximum thickness of the lens, n is the refractive index, R_1 and R_2 are the curvatures of the first and second surface, respectively, and $\rho^2 = x^2 + y^2$. To simplify calculations and reflect typical experimental conditions, the lens is assumed biconvex ($R_1 = R_2 = R$) with a refractive index of 1.5, under which conditions the focal length $f \approx R$. The field just after the lens is then given by

$$E_{out} = E_{in} \cdot \exp(i\phi_{lens}) \tag{2.16}$$

To propagate this field to the fiber plane (x′, y′), a convolution integral is calculated using the spatial impulse response. The resulting equation for the field at a distance *f* behind the lens is given by

$$E_{fiber} = \iint_{Area} E_{out}\left(\frac{-i}{\lambda f}\right)\exp\left(\frac{ik}{2f}((x'-x)^2+(y'-y)^2\right)dxdy \tag{2.17}$$

where the integral is over the entire area of the lens and is repeated for each point (x′, y′) in the fiber plane. The intensity distribution at the fiber plane is then proportional to the magnitude squared of the electric field.

As a measure of how much light is collected by the receiver fiber(s), the overlap between the incoming beam profile and the fundamental mode of the optical fiber was calculated. Equation 2.18 shows the calculation performed using the overlap integral.

$$O = \frac{\int_{-\infty}^{\infty}\int_{-\infty}^{\infty} |E_{fiber}|^2 |E_{fund}|^2}{\int_{-\infty}^{\infty}\int_{-\infty}^{\infty} |E_{fiber}|^2 \int_{-\infty}^{\infty}\int_{-\infty}^{\infty} |E_{fund}|^2} \tag{2.18}$$

where E_{fiber} is the power distribution of light hitting the fiber from the lens and E_{fund} is the power distribution in the fundamental mode of the fiber. The greater the value of this integral, the better the overlap between the field profile and the fiber mode profile, and thus more light is coupled into the fiber. This calculation assumes that the wave is entering the fiber at an angle smaller than the acceptance angle of the fiber, which is the case for the range of angles investigated. For the fiber bundle, the overlap integral was

calculated for each fiber intercepting some part of the incoming field, and the results added to estimate the total coupling of power to the fiber array [27].

Chapter 3

Evaluation of Fiber-bundle-based Optical Transceiver Design

In this chapter, both experimental and simulation-based evaluations were executed to investigate the feasibility of applying multiple fibers at the transceivers to improve the transmission performance on tolerating link misalignment.

3.1 Laboratory Evaluation Overview

Two series of laboratory experiments were implemented to compare the optical link robustness for different transceiver setups as the fiber-lens distance (z_{fl}) was varied to modify the beam divergence: multi-fiber transmitter working with single-fiber-lens receiver and multi-fiber transmitter working with multi-fiber-lens receiver.

3.1.1 Overview of Proposed Transceiver System

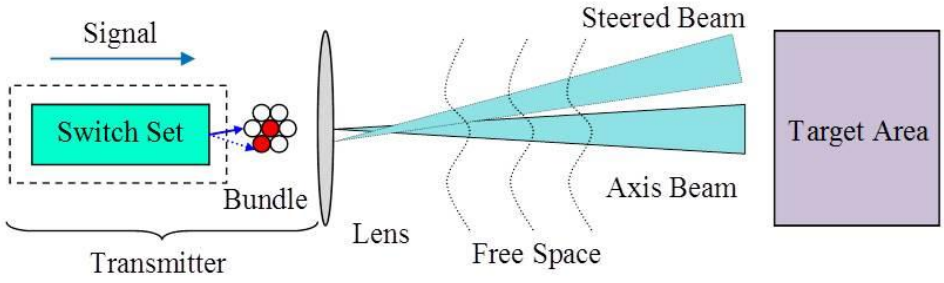

Figure 3.1: Proposed Transceiver System.

The proposed transceiver system is depicted in Fig. 3.1. A signal to be transmitted is directed to one (or more than one) of seven fibers arranged in a hexagonal geometry at the transmitter. A signal directed to the central fiber propagates along the central axis of

the transmitter. If the transceivers are misaligned, the signal can be directed to a fiber away from the axis. Light from such a fiber is deflected at an angle from the axis by the action of the lens, effectively steering the beam through that angle. The distance from the fibers to the transmitting lens is varied to control the divergence of the transmitted beam while still satisfying a certain power budget. Light is collected at the receiving end and appropriately processed to recover the transmitted signal.

3.1.2 Beam Coverage

The goal of using a transmitting fiber bundle is to achieve a large usable coverage area at the receiving end with few or no gaps when power margin is accounted for. Figure 3.2 illustrates the desired effect of using a fiber bundle instead of a single fiber to transmit the beam. In order to achieve a continuous, overlapping beam area, the distance between the adjacent beam patterns provided by the transmitting fiber bundle, *s*, must be determined at a distance *L* from the transmitter. From this, the required separation Δd between fibers in the bundle can be found. To find s, it is assumed that the fibers in the bundle are arranged in a standard hexagonal packing scheme. This results in centers at the vertices of an equilateral triangle.

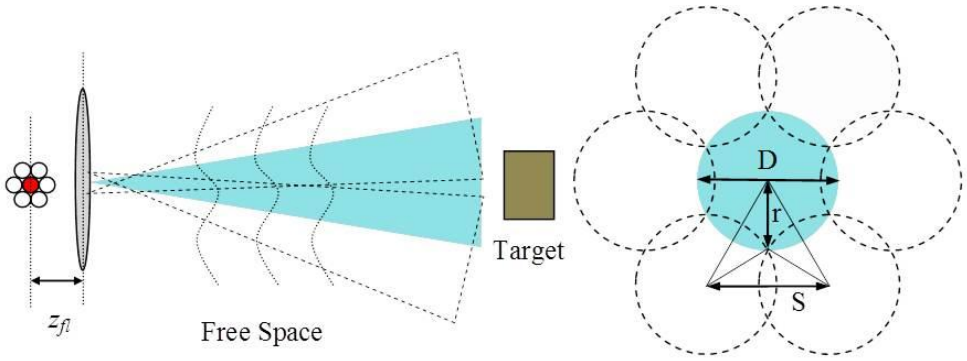

Figure 3.2: Ideal Continuous Beam Coverage Provided by an Optic Fiber Bundle.

To obtain complete coverage, there is a minimum required case shown in Figure 3.2. From geometry, the separation s is given by $s = (\sqrt{3})r$, where r is the radius of the beam. If the calculated Δd is greater than the diameter of the fibers to be used in the bundle, then a bundle that provides the desired coverage can actually be constructed. Using matrix theory for geometrical optics, the equation is given by

$$\Delta d = \frac{(\sqrt{3})r}{1 - L/f} \tag{3.1}$$

where f is the focal length of transmitter lens. In experiments, SMF-28 was used, where the diameter of the fiber without its protective jacket is 125 μm which limits the minimum Δd.

There are three main factors that impact the beam radius. The first factor is the required transmitter power which is the sum of minimum required receiver power (P_{MR}) and Power margin (P_{margin}). The second factor is the transmission geometry; including focal length of lens (f), fiber-lens distance z_{fl} and transmission distance L. The third factor is the receiver geometry; including the lens power (focal length, lens diameter, thickness), the size of the collecting fiber, and the beam incident angle θ_{def}, which is equivalent to the beam deflection angle at the transmitter.

The trade-off between coverage area and required transmitter power limits the use of divergence to improve the coverage area. A larger divergence eventually causes the power to become too spatially dispersed and the connection is lost at larger values of L.
At the transmitter, the focal length of the transmitting lens and fiber-lens distance z_{fl} influence the beam diameter just after the lens, the possible steering angles, and the divergence that can be achieved. Based on earlier theoretical work [28, 29], an optimal z_{fl} range certainly exists to allow the power collected by the lens to satisfy power-margin

requirements with maximum beam coverage. The distance to the target and the desired coverage area in turn restrict the separation between fibers within the bundle, especially when considering the power budget requirements and not just the illuminated area in space.

3.1.3 Receiver

The base receiver concept evaluated in this work is depicted in Figure 3.3. Prior investigations have shown that a high power (short focal length) lens maintains a focal spot closer to the optical axis, and thus to the core of the receiving fiber, for larger alignment errors [30]. For reasons of construction, high power lenses have a smaller diameter and thus a smaller area for collecting incoming light, resulting in less power coupled to the fiber. The design in Fig. 3.3 utilizes an array of high power lenses to increase the effective collection area of the receiver while retaining the advantages of the individual lenses. The signals collected from the lenses must then be combined into a single optical signal for detection by the receiver electronics. Competing receiver concepts differ in lens size, the number of lenses and fibers used, the lens focal length, and method used for combining signals. The method shown in Fig. 3.3(b) will be used in this investigation, based on prior work where this method was demonstrated to provide the best misalignment tolerance [30].

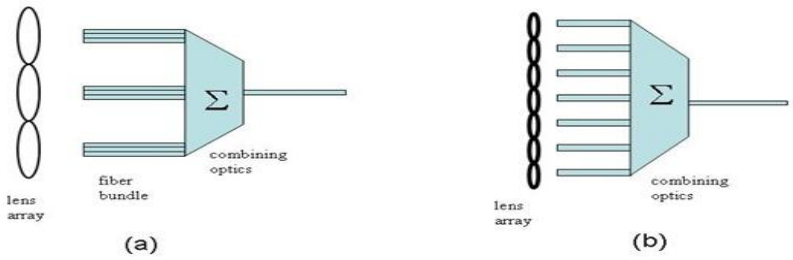

Figure 3.3: Proposed receivers (a) Large lenses, 7-fiber bundles. (b) Array of smaller lenses, single fiber per lens.

3.2 Experimental Procedure of Laboratory Evaluation

In the experimental investigation, the effects of single and multiple receiver sets on the FSO transmission performance while changing z_{fl} at transmitter was explored. Generally, the experiments consist of two parts: received power tests and byte bit error rate (BBER) tests.

3.2.1 Received Power Test

In the received power test, experiments measured simply the power collected by the receiver for different settings of the transmitter parameters. The experimental configuration is shown in Figure 3.4. A fiber-coupled, continuous wave laser at 1550nm was used as the source and passed through a power amplifier. The output power from the amplifier was split using a 50/50 coupler and delivered to two fibers. The transmitter consisted of the two fibers mounted on a motorized translation stage at a point behind a fixed lens. The lens focal length was 75mm and its radius was 12mm. The distance z_{fl} between the fiber ends and the lens was controlled by the motorized stage that was in turn controlled by a laptop computer. The receiver consisted of two lenses, each lens coupled to one output of a multimode combiner (a 50/50 splitter used in reverse), and the output of the combiner measured by a fiber-coupled power meter. The lenses had a radius of 6mm and a 20mm focal length. While the intention was to have the two lenses adjacent to each other, there was a 4mm gap between the edges of the lenses due to limitations of the positioning structures. The entire receiver was mounted on a moving plate controlled by a micropositioner. This configuration allowed the receiver unit to be misaligned with the optical axis of the transmitter in a controlled manner. The receiver and transmitter

were 1.95 meters apart (lens to lens) and the total power out of the source and amplifier was 29.9mW.

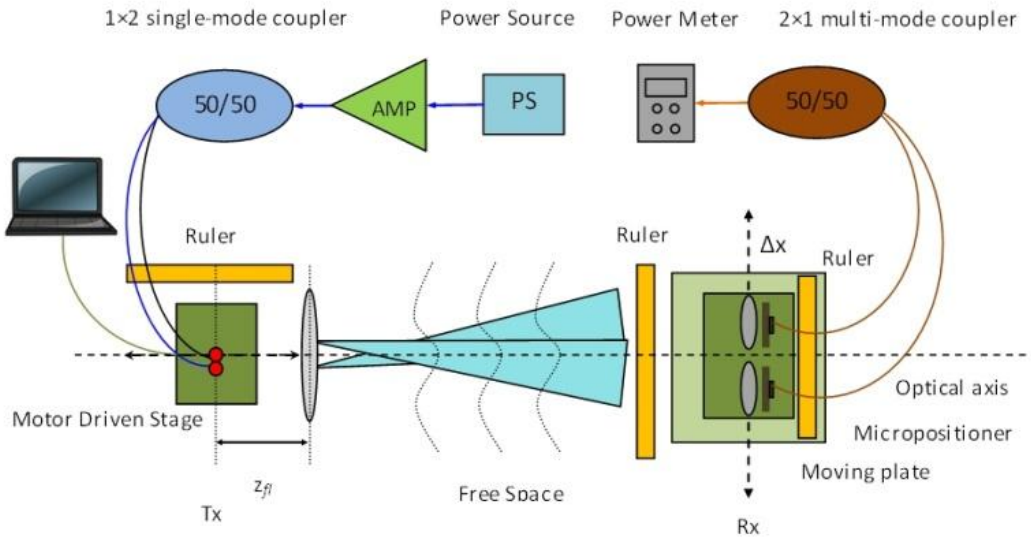

Figure 3.4: Received Power Test Setup at 1550nm Wavelength.

For the experiment, the power collected by the receiver was monitored as a function of the misalignment between the transmitter and receiver optical axes and as a function of the transmitted beam's divergence. Changing the value of z_{fl} controlled the divergence of the beams. Figure 3.5 shows the dependence of the beam divergence on z_{fl} when a visible light source was employed. As z_{fl} increases, the two visible circular contours become smaller and present a trend of separating from each other. Initial alignment of the axes was achieved by adjusting the receiver position until the maximum power was observed from the upper lens in Figure 3.4 on the power meter when z_{fl} was chosen to produce a collimated beam from the transmitter. This value of z_{fl}, called $z_{fl\text{-}initial}$, was the starting point for each experiment. Using the micropositioner, the receiver

was translated perpendicular to the optical axis at 1mm intervals and the received power was recorded. The value of z_{fl} was changed incrementally and the process repeated at the receiver for each new value of z_{fl}. Experiments were performed using only one lens for the receiver (the other lens is blocked) and using both lenses for the receiver.

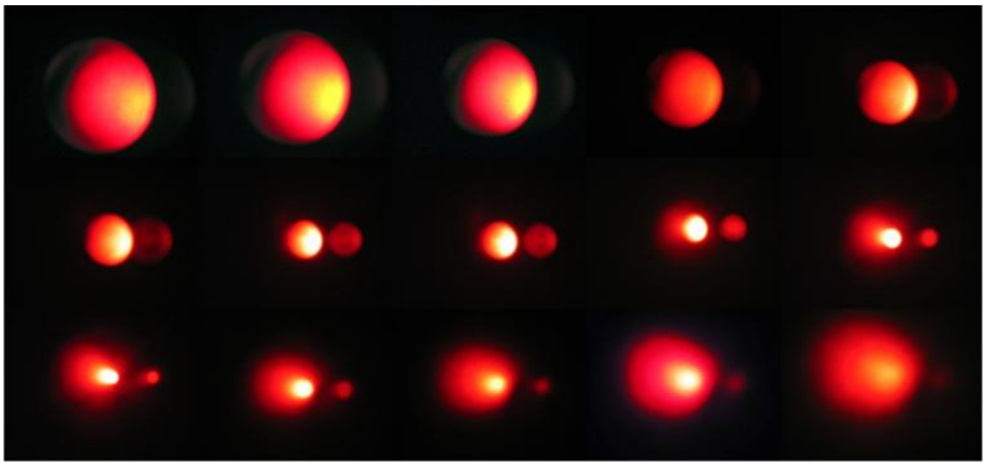

Figure 3.5: Beam Patterns at Receiver End for Varying z_{fl} Using Visible Light.

3.2.2 BBER Test

Differing from the power test, the BBER test measured not only the power collected by the receiver but also the BBER as a function of link performance for different settings of the transmitter parameters. The experiments in the BBER test shared a similar platform, operation procedures, and many of the same parameters with the power test. Instead of the power source and amplifier in the previous test, a SONET-based bit-error-rate tester (BERT) was used as the transmitter operating at 1310nm wavelength. The transmission power was 1.12mW. The BERT used in the experiments also provides measurement of the received average power and analyzes the return signal using the SONET standard measures. Each BBER measurement was operated in a three-

minute run. Similar to the power test, experiments were performed using a single lens for the receiver (the other lens is blocked) and using double lenses for the receiver.

3.3 Experimental Results

3.3.1 Power Measurement at 1550nm Wavelength

In the power test at the wavelength of 1550nm, seven z_{fl} points were used, including the initial fiber-lens distance point. An increment of 0.5mm was used between two adjacent points. Thirty-two misalignment reference points were picked between the transmitter and receiver optical axes with an interval of 1mm. The motion axis of the stage controlling z_{fl} was not exactly perpendicular to the plane of the transmitting lens, which led the center of the coverage area to drift slightly as z_{fl} was varied. To better compare the data obtained from each z_{fl} point, the data was re-aligned using anchor points.

Figure 3.6(a), Figure 3.6(b) and Figure 3.6(c) show the power test results at 1550nm wavelength with two single lenses separately and the combination of these two single lenses. For the convenience of description, one receiving lens was named as lens No.1, corresponding to the lower-most lens in Figure 3.4, the other was lens No. 2 and the combination of two adjacent lenses is called double lenses. The x-axis indicates the sample misalignment over a 31mm adjustment range at the receiver end. The y-axis indicates the total received power at the output of the combiner. The blue circular, red square and green triangle markers stand for the results for 0.5mm, 2mm and 3.5 mm z_{fl} increment respectively at the transmitter. To represent each trend clearly, the relative markers are connected by the solid lines.

The results in Figure 3.6(a) can be directly related to the beam pattern trends of Figure 3.5. The results of Δz_{fl} at 0.5mm represent most nearly the second pattern of the first row in Figure 3.5, where the overlapping of the two beam outputs from the transmitter results in a more flat power distribution between the beam centers at the receiver. The results of Δz_{fl} at 2.0mm represent most nearly the first pattern of the second row in Figure 3.5, where the peak power gets higher and the power distribution gets narrower with less overlap in the center. The results of Δz_{fl} at 3.5mm are more like the last pattern of the second row in Figure 3.5, where the peak power is the highest and the power distribution is the narrowest, as the two individual peaks are becoming more distinct. The uneven peak powers are caused by the imperfect system alignment and the mechanical restriction of the lens mounting hardware used. A slight downward adjustment of the receiver platform would cause a swap of the power distribution on the graphs, with lens No.1 having a much lower power and lens No.2 a much higher one.

Compared with the results of the power test with lens No.1, the test with lens No.2 shows similar trends but with smaller peak powers due to the alignment issue. In Figure 3.6(c), the results show that with the double lenses, the range for which the received power remains non-zero is much larger than that achieved with either of the lenses alone.

More importantly, there is evidence of interference occurring between the light collected by the two lenses. This evidence is shown in Figure 3.7, which shows the results for Δz_{fl} as 0.5mm, where the effects of interference were most pronounced. The black circles represent a direct sum of the data recorded from experiments on each lens individually, while the red squares is the data taken when both lenses contributed to the

output power from the combiner. At Δx = 25mm, which corresponds to the receiver position where there are significant contributions from both lenses, the power measured from the combiner when light was being combined from both lenses is just 53.4% of the value obtained from summing the data points from the single lens experiments. This indicates that, for our current experimental arrangement at least, there is contribution to the results from interference that may be occurring between the light received from the two different optical paths originating at the transmitter's splitter and ending at the combining point at the receiver.

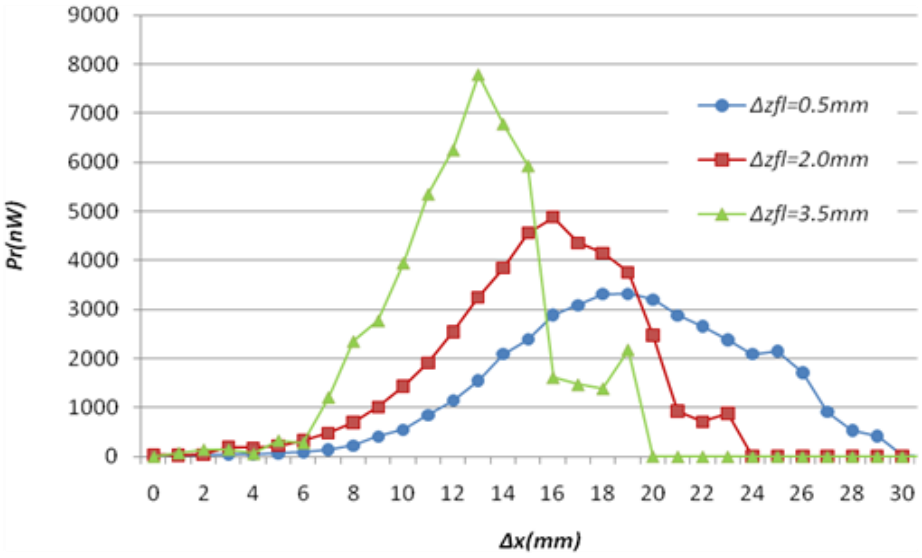

(a)

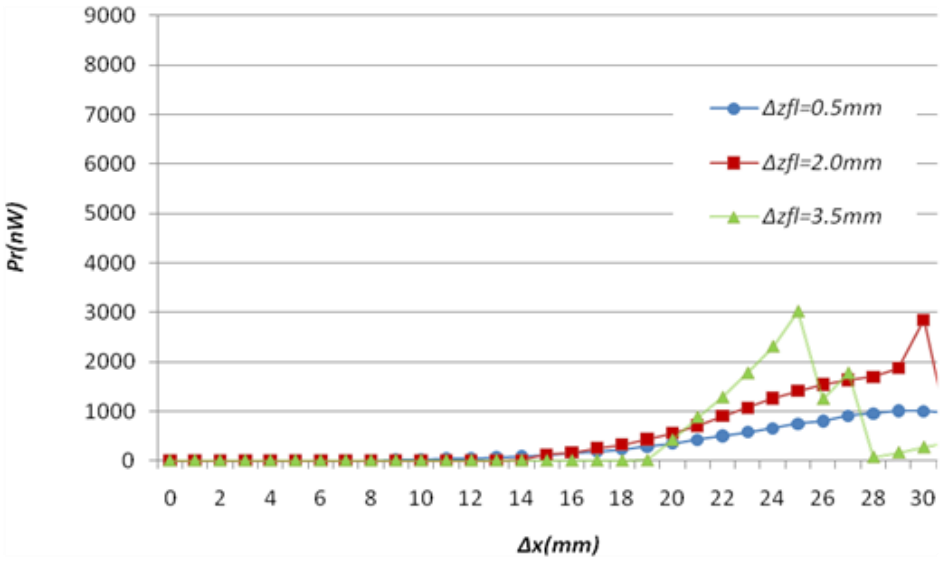

(b)

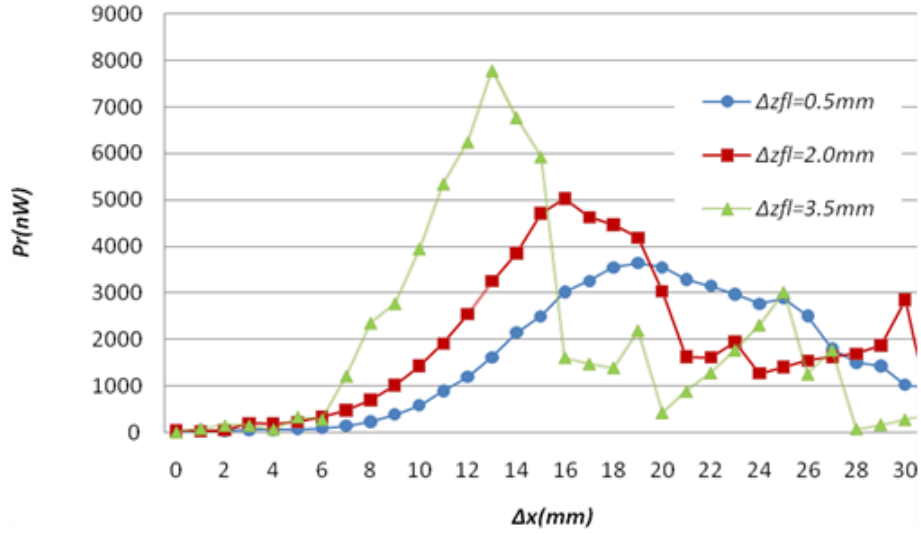

(c)

Figure 3.6: Power Test at 1550nm (a) for only lens number 1, (b) for only lens number 2, (c) for both lenses operating simultaneously

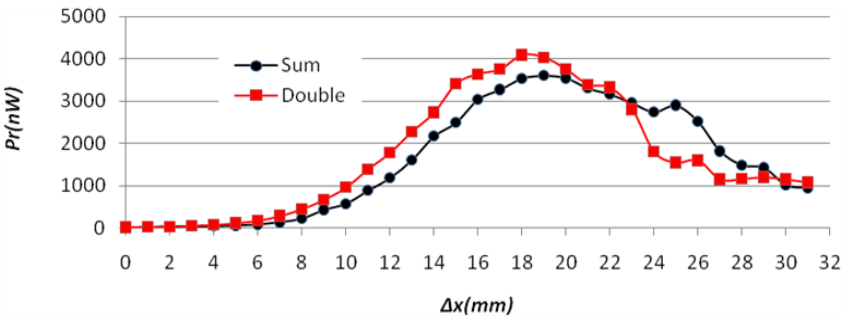

Figure 3.7: Comparison between the Summing Data and the Lens-Combination Data.

3.3.2 Power Measurement at 1310nm wavelength

Four different z_{fl} points with increment of 0mm, 0.5mm, 1mm, and 1.5mm from $z_{fl\text{-}initial}$ were chosen in power tests at 1310nm wavelength. The same thirty-two Δx sample points used in the 1550nm power test were used at 1310nm. Experimentally, the only differences were the source and detector, which were combined in the BERT instead of using stand-alone devices. Figure 3.8 demonstrates the power measurement results for 1310nm. The x-axis is again the misalignment sample points and the y-axis is the received power in dBm.

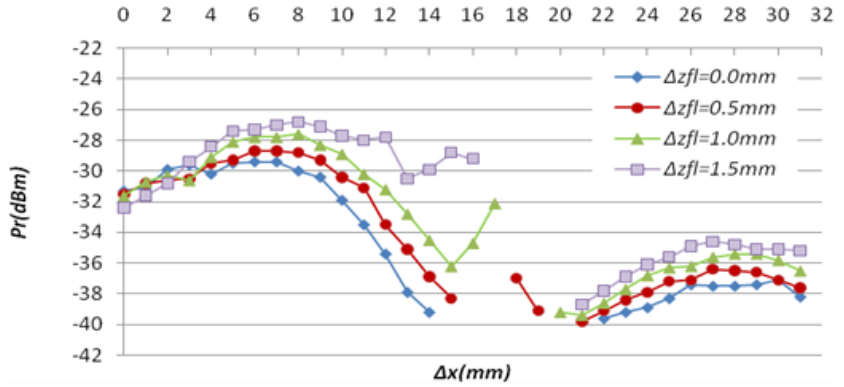

Figure 3.8: Power Test at 1310, Showing the Result Obtained with Both Lenses Receiving Light.

Owing to the absence of an available power amplifier at 1310nm, the total transmitted power of the source is 1.12mW or 0.5dBm, which is much lower than the power available at 1550nm. For this reason, there are values of Δx for which no data is shown, as the power level was below the detection threshold of the BERT. The results of the power test with lens No.1 do not show the left edge of the power distribution in Figure 3.8 due to the limited range of the moving plate at the receiver. However, the data present the same trend as in the previous test at 1550nm that the peak power increases while increasing the fiber-lens distance at the transmitter, and with double lenses, the total power coverage was significantly enlarged. The discontinuity of the curves in Figure 3.8(c) is caused by the gap between the edges of the two receiver lenses, which greatly reduces the captured power, and the low initial power of the source.

3.3.3 BBER Measurement at 1310nm Wavelength

Measurements of the BBER as a function of the receiver position were taken concurrently with the power test at 1310nm. The results of the BBER test are displayed in Figure 3.9(a), Figure 3.9(b) and Figure 3.9(c). A BBER value of 1 was assigned to those cases where there were continuous errors on the link, and the BERT no longer logged the BBER. A BBER of 0 in the tests was replaced by a value of 10^{-10} for graphing purposes. The data rate was set as OC-12. Independent tests on the BERT alone found that the minimum received power required to record a BBER other than "1" was -36 dBm, and determined the expected BBER for a given input power, assuming minimal signal distortion between the transmitter and receiver. Given this information, the BBER results were compared to the power measurement results to see whether or not there was

a direct correlation between the two results. If continuous errors occurred before the received power fell below -36 dBm, or if the BBER for a given power was higher than expected, then the receiver configuration was negatively impacting the signal. In particular, it was of interest whether the combining of the two signals – either at the lens plane of

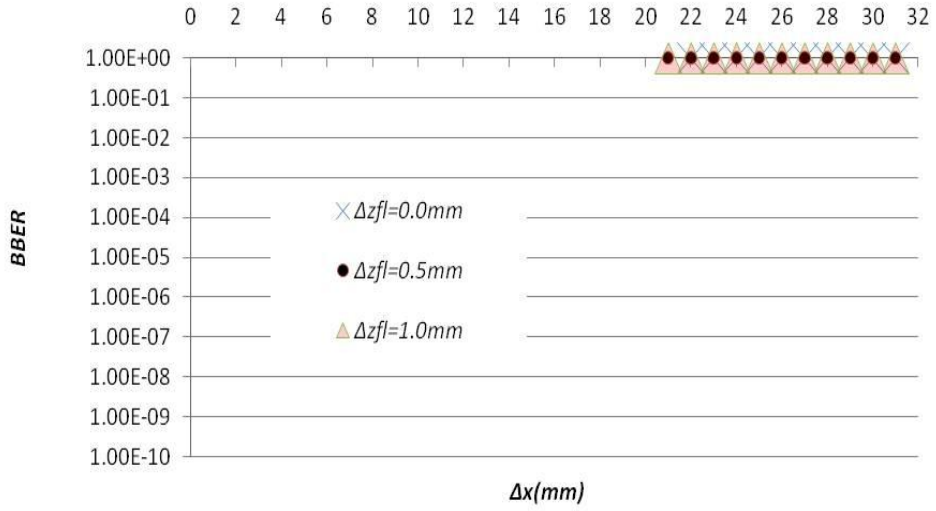

(a)

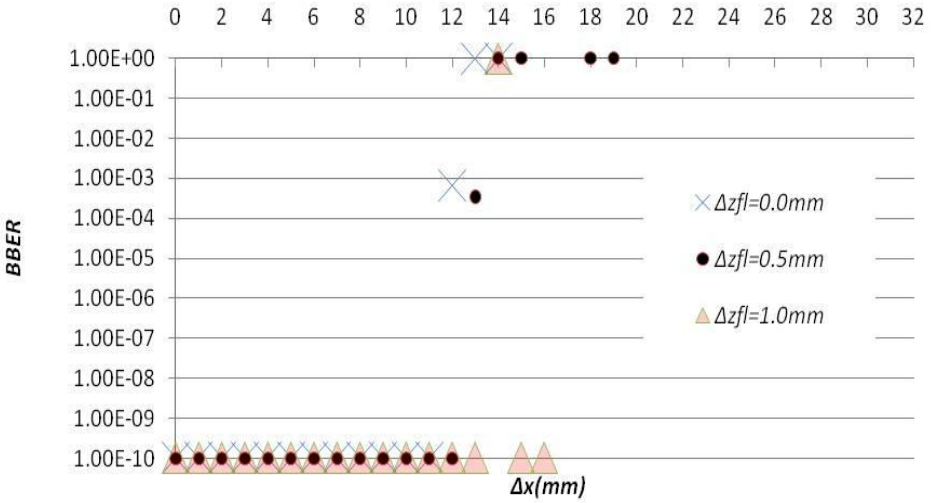

(b)

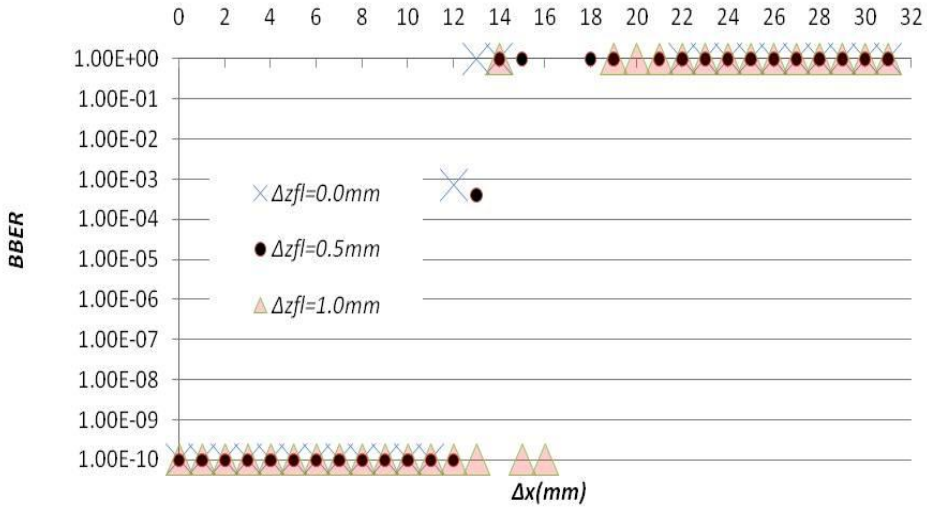

(c)

Figure 3.9: BBER Test at 1310nm with (a) only lens 1 collecting light, (b) only lens 2 collecting light, (c) both lenses collecting light simultaneously.

the receiver or at the output of the power combiner – would negatively impact the signal quality as evidenced by a higher BBER. Comparing the BBER data to that from the power experiment, no consistent, statistical increase in the BBER was observed, and continuous errors occurred at the positions where the collected power fell below -36 dBm. As before, the results of the double lens experiment demonstrate the increased coverage capabilities over a single lens arrangement.

Extrapolation of the experimental results to the overall transmitter design shown in Figure 3.2 provides insight on the potential performance characteristics of the overall design. Experimentally, the two fibers at the transmitter were adjacent to one another, producing two fairly closely spaced beams at the transmitter, as indicated in Figure 3.5. The coverage area of the overall transmitter may be enhanced by separating the fibers

slightly while increasing the beam divergence as well to ensure some power overlap between the outputs of the individual fibers. This would come at the cost of a lower peak power available at the receiver, and it would be possible to separate the transmitter fibers so much that the loss in peak power would cause gaps in coverage, resembling the gap seen in Figure 3.9 between the two lenses. That is, even though there was light from one or more fibers at the point where their respective output beams intersected, and thus the point is "covered" by light, there may be insufficient optical power to maintain the desired link BER. The best balance between the transmitter fiber separation and the beam divergence results in the maximum coverage area achieved by the transmitter.

Simultaneously illuminating multiple fibers in the transmitter bundle would provide a larger coverage area for any one setting of the transmitter. This approach could reduce the number of switching events required to track a receiver and reduce the link down time due to the switch, depending on how the switch is executed. The data suggests that a potential drawback of this approach may be increased interference at the overlap points as more optical beams are combined at the receiver end. If interference is severe enough, gaps in the achieved BER could occur even if optical power is present over the entire area, which would degrade the overall system performance. Thus, the fill factor, defined here as the emitting area (the total of the fiber core areas) divided by the overall area of the transmitting fiber array, needs to be properly chosen to obtain the best performance, in terms of coverage area at the receiver, for the transmitter.

3.4 Conclusion of Laboratory Evaluation

The series of laboratory experiments present three crucial results on the investigation of deploying multiple fibers on both the transmitter and the receiver. First, the results of power test at 1550nm wavelength shows the overlapping of the two beam outputs from the transmitter could result in a flat power distribution between the beam centers at the receiver, and the beam coverage was extended by the utilization of two lens-fiber pairs at the receiver instead of a single pair. This correlates well with earlier experiments performed with a single transmitting fiber and fixed z_{fl} [11], and the power distribution with Δx is almost the same, despite the use of a more optimal lens-fiber coupling system (higher efficiency, no gap) in the earlier work. Second, the beam coverage improvement was also observed in the power and BBER test at 1310nm wavelength; however, the results were not ideal due to the imperfect alignment, weak transmission power and the separation between the receiver lenses. Third, interference that might be caused by the transmitter's splitter and the beam coupler at the receiver was discovered, which could impair the advantages of deploying the multiple fibers at transceivers. Efforts are ongoing to determine the sources of interference, such as phase shifts at the splitter and combiner, and to minimize their effects.

3.5 Simulation-based Evaluation Overview

The dependence of the coverage area on key parameters such as transmitter power, number of fibers in the transmitting fiber that are illuminated, beam divergence and system length is investigated via simulation and compared to prior observations of these dependencies to verify the efficacy of the model used in the simulation. The results

obtained from the simulation are also verified by direct comparison with current experimental data.

The system to be modeled by the simulation is shown in Figure 3.10. The optical power from a signal source is delivered to a distribution fabric for coupling to the fibers in the transmitter array.

The distribution fabric may consist of power splitters, optical switches, or some combination thereof in order to illuminate single fibers or combinations of two or more fibers to achieve a desired coverage area at the receiver [11]. The outputs from the transmitter fibers are coupled to a convex lens for the current study, although an optical telescope can be easily substituted. The separation between the transmitter fibers and the distance z_{fl} between the fiber tips and the lens control the deflection angle and the divergence of the beam respectively, with both dependent on the choice of focal length and structure of the lens. The light transmitted by the lens propagates through space to the receiver. At present, the effects of turbulence were neglected, but will be included in a later study. At the receiver, an array of lenses captures the transmitted light, with each lens coupled to its own optical fiber. For the results reported here, the number of lenses in the array was limited to three to reduce computational time. The outputs of the individual fibers are summed together to arrive at the total power collected by the receiver.

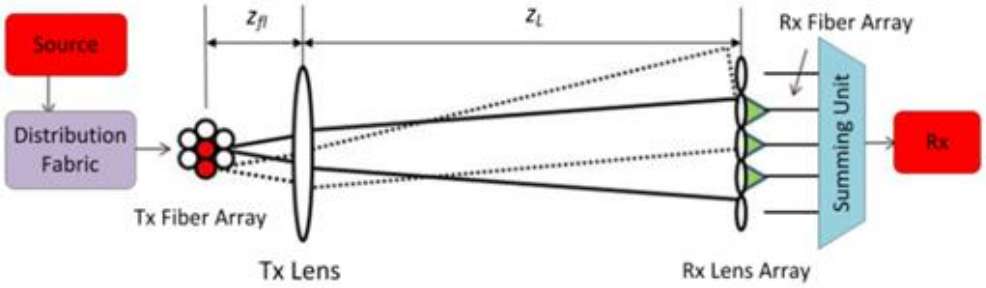

Figure 3.10: System under Study for the Simulation.

3.6 Simulation Components

3.6.1 Calculating Field at Receiver Plane

The first part of the simulation calculates the electric field and intensity distributions at the input plane of the receiver using a combination of Gaussian beam propagation and geometrical optics. The output field from one of the transmitting fibers, which are single-mode fibers in practice, is approximated as a Gaussian distribution with initial beam waist equal to the radius of the fiber core (denoted w_o) and infinite radius of curvature. For a given choice of the transmitter power, the peak values of the intensity (I_o) and field (E_o) distributions can be calculated from the Gaussian distribution. The field at the receiver is then calculated using the matrix method for Gaussian propagation, given by

$$E(r, z_L) = E_o \frac{w_o}{w(z_L)} \exp\left(\frac{-\mathrm{r}^2}{\mathrm{w}^2(\mathrm{z_L})}\right) \exp\left(-\mathrm{ikz_L} - \mathrm{ik}\frac{\mathrm{r}^2}{2\mathrm{R}(\mathrm{z_L})}\right) \tag{3.1}$$

$$q(z_L) = (Aq_o + B)/(Cq_o + D) \tag{3.2}$$

$$\begin{bmatrix} A & B \\ C & D \end{bmatrix} = \begin{bmatrix} 1 & z_L \\ 0 & 1 \end{bmatrix} \begin{bmatrix} 1 & 0 \\ -1/f_{Tx} & 1 \end{bmatrix} \begin{bmatrix} 1 & z_{fl} \\ 0 & 1 \end{bmatrix} \tag{3.3}$$

$$\frac{1}{q(z_L)} = \frac{1}{R(z_L)} - i\frac{\lambda}{\pi w^2(z_L)}; \quad \frac{1}{q_o} = -i\frac{\lambda}{\pi w_o^2} \tag{3.4}$$

where f_{Tx} is the focal length of the transmitter's lens and $k = 2\pi/\lambda$. For the center fiber, no modification of the distribution equations is necessary. For the side fibers, the field distributions must reflect the deflection of the beam due to bending of the rays by the transmitting lens. To approximate this deflection at the receiver plane, the matrix method for geometric optics is used, given by

$$\begin{bmatrix} r(z_L) \\ \theta(z_L) \end{bmatrix} = \begin{bmatrix} A & B \\ C & D \end{bmatrix} \begin{bmatrix} r_{fiber} \\ 0 \end{bmatrix} \tag{3.5}$$

where the ABCD matrix is given by equation (3.3) and r_{fiber} is the position of the transmitting fiber with respect to the central axis of the fiber array. The field contribution from the side fiber at the receiver array is then approximated by

$$E(r, z_L) = E_o \frac{w_o}{w(z_L)} \exp\left(\frac{-((\mathrm{x}-\mathrm{x_L})^2+(\mathrm{y}-\mathrm{y_L})^2)}{\mathrm{w}^2(\mathrm{z_L})}\right) \exp\left(-\mathrm{ikz_L} - \mathrm{ik}\frac{((\mathrm{x}-\mathrm{x_L})^2+(\mathrm{y}-\mathrm{y_L})^2}{2\mathrm{R}(\mathrm{z_L})}\right) \tag{3.6}$$

where $r(z_L)^2 = x_L^2 + y_L^2$ and the values of x_L and y_L are determined by the geometric position of the transmitting fiber with respect to the center of the transmitting array. For the simulations presented here, the side fibers are chosen to be along the x direction only,

so that $x_L = r(z_L)$, with the appropriate choice of sign, and $y_L = 0$. If more than one transmitting fiber is emitting light, the field contributions from all of the light-carrying fibers are added together, and the intensity at the transmitting plane is given by

$$I(r, z_L) = \frac{\varepsilon_o c}{2} \left| \sum_{i=1}^{N} E_i \right|^2 = \frac{\varepsilon_o c}{2} |E_{total}|^2 \tag{3.7}$$

where N is the number of fibers transmitting power.

3.6.2 Calculating the Collected Power

To determine the amount of optical power collected by the each fiber in the receiver's lens-fiber array, the electric field distribution at the fiber tip must first be calculated. This field is calculated using Fourier Transform methods and a one-step propagation method [31]. The basic equation for this method is given by,

$$U_{out} = \frac{1}{i\lambda f_{Rx}} \exp\left(\frac{ik}{2f_{Rx}}(x_f^2 + y_f^2)\right) \mathcal{F}\left(U_{in} \exp\left(\frac{ik}{2f_{Rx}}(x_{in}^2 + y_{in}^2)\right)\right) \tag{3.8}$$

where f_{Rx} is the focal length of the receiver, x_f and y_f are the coordinates at the fiber tip, x_{in} and y_{in} are the coordinates at the output plane of the receiver's lens, and U_{in} is the field at the output plane of the lens, given by

$$U_{in} = E_{total} * T_{lens} \tag{3.9}$$

and T_{lens} is the phase transfer function of the lens given by [32]

$$T_{lens} = \exp(ikn_{lens}t)\exp\left(-ik(n_{lens}-1)*(R_l - R_r)\right) \tag{3.10}$$

$$R_{l,r} = R_{1,2}*\left(1-\sqrt{\frac{1-(x_{in}^2+y_{in}^2)}{R_{1,2}^2}}\right) \tag{3.11}$$

where R_1 and R_2 are the radii of curvature for the left surface and right surface of the lens, respectively, and t is the lens thickness. If the receiver lens is not centered about the central axis of the system, then equation (3.8) and (3.11) are modified such that

$$x_{in}^2 + y_{in}^2 \rightarrow (x_{in}-x_0)^2 + (y_{in}-y_0)^2$$

where x_0 and y_0 are the coordinates of the center of the lens. The power collected by the fiber is then determined by integrating the intensity of U_{out} over the area of the collecting fiber's core.

3.6.3 Implementation

The above calculations were performed using the MATLAB software package. All of the field distributions were calculated in square arrays of discrete points. In the simulation, the Fourier Transform in (3.8) is performed using a FFT, and the spacing and number of input grid points is selected such that the dimensions of U_{out} describe a square with the same width as the core diameter of the collecting fiber [31]. The power collected

is approximated by numerically integrating the sampled intensity of U_{out} over the output grid using a cubic spline to estimate the intensity distribution from the data grid.

3.7 Simulation Results

3.7.1 Simulation Parameters

Several common configurations and parameters were used throughout all of the simulations performed. The transmitter consisted of three transmitting fibers lying in a line along the horizontal axis of the transmitting lens, with the center fiber aligned to the center of the lens. The fibers were assumed to be single-mode fibers in the infrared with a core radius of 5.6 μm and a cladding diameter of 125 μm. Following the configuration used experimentally, the fibers were stripped of the jacket and placed in contact with each other so that the spacing between cores was 125 μm. The transmitting lens was biconvex with a focal length of 50 mm. For most of the reported results, z_{fl} = 48.5 mm, unless otherwise noted. The receiver consisted of three plano-convex lenses, each coupled to a multimode fiber. The receiver lenses were also arrayed along the horizontal axis, had a focal length of 3 mm, radius of curvature of 0.045 inches, and center-to-center spacing of 0.09 inches. The source had a maximum power of 3 mW at a wavelength of 1.31 μm. The two transmission distances reported here are 15 m and 25 m, which were used to explore dependence on transmission distance while reducing the computation time.

3.7.2 Number of Transmitting Fibers

The first study examined how the number of transmitting fibers that emitted power impacted the coverage area at the receiver. While the coverage area is expected to expand, the division of the source power amongst the multiple fibers and the possibility of interference between the beams can both serve to reduce the actual area over which sufficient power is collected to maintain the link. Sample outputs for one, two, and all three transmitter fibers emitting power are shown in Figure 3.11 for a transmission distance of 25 m. The graphs represent the power collected by the receiver as it is scanned over an 8.5 cm by 8.5 cm area centered on the optical axis of the transmitter. The reduction in power collected as the source is divided amongst multiple fibers is clearly visible when comparing the results for three fibers to both the single fiber and two fiber cases.

Although the coverage area generally increases as the number of fibers increases, the increase observed in the coverage area then strongly depends on the minimum required power to meet the BER requirements for the link. If, for example, the minimum power was 15 μW (1.5 on the vertical axis in the graphs), the increase is from four grids (20 mm) along the direction of the receiving lens array to 13 grids (65 mm). Increases are less significant if the minimum required power is lower, however the collected power would remain higher for a wider range of misalignment, which would be desirable assuming the summing is ideal as is assumed here.

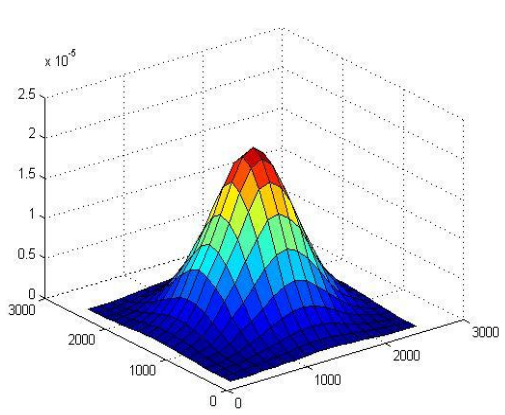

(a)

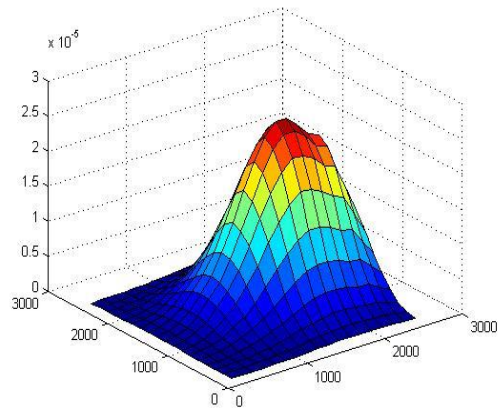

(b)

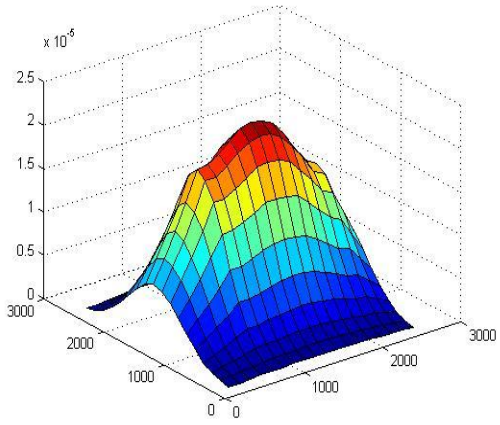

(c)

Figure 3.11: Simulation Results for (a) center fiber only, (b) center and one side fiber, and (c) all three fibers emitting. Vertical axis is power (x 10^{-5}). The scan area is 8.5 cm x 8.5 cm. The grid spacing is 5mm in both scan directions. z_L = 25 m.

3.7.3 Power and Divergence

The simulation for the three transmitting fiber case was repeated for different source power and beam divergence (z_{fl}). Sample results are shown in Figure 3.12. In Figure 3.12(a), the power per transmitting fiber was reduced from 1 mW to 0.25 mW, with all other parameters unchanged. Comparing to Figure 3.11(c), the power collected has been reduced proportionally by the same factor of four. In Figure 3.12(b), the distance between the lens and the tips of the transmitting fibers was increased by 1 mm to 49.5 mm, just 0.5 mm from the focal length of the transmitting lens. The reduction in divergence is quite noticeable, with the contributions from the three transmitting fibers easily distinguished. The peak power collected by the receiver increased to almost 50 μW, but the coverage area is much reduced as most of the power is concentrated in a small area at the receiver. Increasing the divergence by decreasing the distance between the fiber tips and the transmitting lens will increase the overlap between the beams at the expense of decreased peak power. Earlier work demonstrated that an optimum divergence exists for maximizing the coverage are when working with a single transmitting beam and a single receiving lens [28], and so further extensive application of the simulation is expected to find a similar behavior.

3.7.4 Transmission Length

Transmission length impacts the operation of the link in two ways. First, the beams at the transmitter are separated by a different distance, with the distance increasing with increasing transmission length. Second, the beam waist due to divergence will increase with increasing transmission length. For systems with different lengths or

different ranges of transmission length over which they are expected to operate, several parameters of the system must be chosen carefully, including the divergence, the power of the transmitting lens, and the separation between the transmitting fibers. All three of these factors can impact the power collected and coverage area achievable at the receiver.

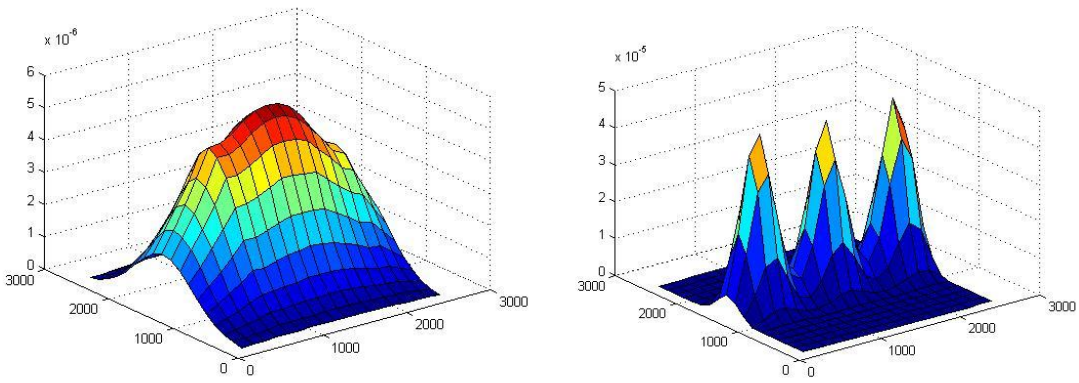

(a) (b)

Figure 3.12: Three Fiber Transmitting Cases from Figure 2(c), with the Following Changes: (a) P_{Tx} = 0.25 mW per fiber instead of 1 mW per fiber; (b) z_{fl} = 49.5 mm instead of 48.5 mm.

Figure 3.13 shows one example comparing the three transmitting fiber case for systems of two different transmission lengths. The peak collected power is significantly higher for the 15 m length in Figure 3.13(b), but again at the cost of a reduced coverage area due to reductions in beam separation and divergence. At the 15m distance, the system designer could maximize the coverage area by increasing the spacing between the fibers in the transmitter bundle and increasing the divergence. If this design is performed

carefully, the peak power could be maintained at least at the 25 m system level and produce a significantly larger coverage area.

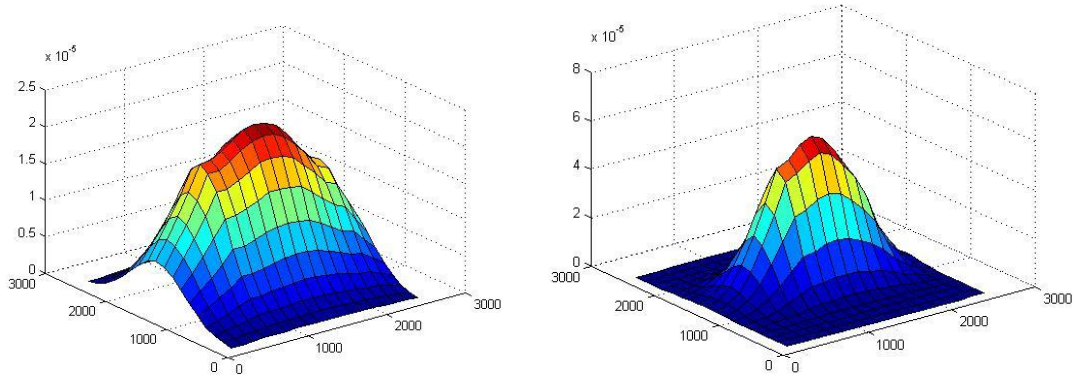

(a) (b)

Figure 3.13: Comparison of Collected Power for Three Transmitting Fiber Case, z_{fl} = 48.5 mm, and Transmission Lengths of (a) 25 m and (b) 15 m.

3.8 Summary of Simulation

A simulation has been developed that models the operation of a novel optical wireless link that utilizes fiber bundles at both the transmitter and receiver to achieve beam steering and improved misalignment tolerance respectively. The initial results presented here demonstrate the fundamental behaviors of the system that have been observed experimentally in previous work. Extensive application of the simulation is presented in Chapter 4 to explore how the coverage area depends on wavelength diversity and other key system parameters, and therefore identify best design choices of such links under a variety of operating requirements and conditions.

Chapter 4

Design Analysis of Fiber-bundle-based Mobile FSO Link

Through theoretical modeling and experimental assays in previous work [11, 33-37], the effectiveness of designs that use fiber optic bundles to improve the misalignment tolerance of FSO transceivers has been demonstrated, and such designs have shown the potential for producing a compact, lightweight FSO communication system that can maintain a quality link under a variety of adverse operation conditions. However, a more detailed exploration is required to determine whether these new designs are more tolerant of changes in the operating wavelength, and what design choices allow for a broader wavelength operating range. Ideally, the power budget and misalignment tolerance for the link would vary only slightly with a variation in wavelength.

4.1 Design Challenge and Solution

The mobile optical wireless transceiver design is complicated by the presence of atmospheric turbulence and weather, which can cause signal fade or complete signal loss even in well-designed systems. Simple solutions such as increasing the transmitter power (for overcoming attenuation due to rain or fog) and increasing the effective collection area of the receiver (for reducing turbulence effects) have practical limitations, especially for mobile platforms where size, weight, and power consumption are more constrained [9, 38, 39]. Robust and innovative approaches to tracking have been able to reduce the number and duration of signal fades due to turbulence, including turbulence caused by motion of the transceiver and its host platform, but there remains ample room for further

improvement. Therefore, different or complementary solutions are needed to further mitigate the effects of turbulence and weather.

Wavelength diversity has shown promise as a complementary solution for counteracting the effects of turbulence [40, 41]. For a given turbulence condition, characterized by its inner and outer scale for turbulent eddies, the amount of diffraction and refraction of the optical beam is strongly dependent on the wavelength of the radiation. For wavelengths on the same order as the outer dimension, diffraction and refraction effects are strong, and distortion and displacement (or deflection) of the beam profile are significant. As the wavelength of the radiation increases, the diffraction and deflection effects are reduced which can improve the ability of the receiver to collect sufficient power to maintain signal quality [40]. Another potential benefit of wavelength diversity is the difference in absorption by water (rain or water vapor) and other airborne substances at different wavelengths. Therefore a wavelength may be chosen to reduce weather effects or turbulence effect, or in the ideal case reduce both effects.

A potential concern with the use of wavelength diversity is the wavelength dependence of the optical components in both the transmitter and receiver. In particular, the lenses that control the beam divergence at the transmitter and the condensing of light onto the collecting fiber(s) at the receiver have refractive properties that are strong functions of wavelength. Even small variations in the imaging properties of the lens can have a strong negative impact on the optical power throughput of the link. This is especially true at the receiver, where the coupling of light by a lens into a core of an optical fiber requires precise alignment to be efficient. For wavelength diversity to be a viable option, then, the design of the transceivers must properly address this concern.

This chapter investigates the interrelationships between key design variables and their impact on design choices for an FSO transceiver that must operate in a system employing wavelength diversity. The investigation builds upon a previously developed theoretical simulation of a link constructed from transceivers that use fiber bundles at both the transmitter and receiver [36]. The dependence of the coverage area, defined as the area over which the receiver can move and still collect sufficient power to maintain the link, on the wavelength and other key parameters such as transmitter power, number of fibers in the transmitting fiber that are illuminated, number of lenses in the receiver array, beam divergence and link length is investigated and the results are used to suggest design choices for the transceiver.

4.2 System Overview

The system to be modeled here by the simulation has been introduced in Section 3.5, which is shown in Figure 3.10. The theoretical formulism and implementation method are also explained in Section 3.6. For this study, a lossless summing method is assumed, designs for which have been developed and will be reported elsewhere.

To study the similarity between the results obtained experimentally and theoretically, a series of laboratory experiments were conducted first. The experimental system used in the investigation is shown in Figure 4.1. A laser supply operating at either 1310 nm or 1550 nm wavelength was used as the signal source for the link, and the output was passed through an amplifier to control the transmitted power and then delivered to a 1×4 coupler with 0.25 splitting ratio. A power meter was connected to one coupler output for the purpose of monitoring the transmitted power.

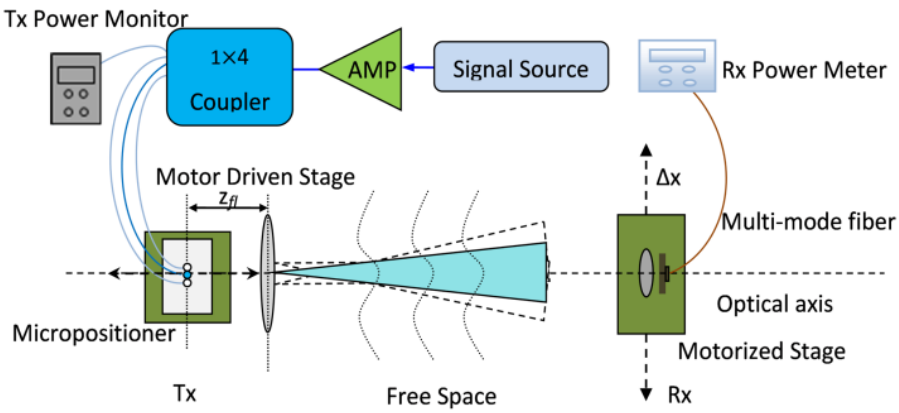

Figure 4.1: Experimental System Setup showing Major Transmitter and Receiver.

The transmitter consists of three standard single-mode fibers cemented together in a linear configuration, a coupling lens (biconvex, 75mm focal length), and micropositioners to control the alignment between the fiber ends and the lens. Each fiber in the transmitter is connected to one output of the coupler when all three transmitter outputs are needed during tests; only center fiber is connected to one coupler output when only a single transmitter output is required. The fiber core radius is 5.6 μm and the cladding diameter is 125 μm, the refractive index difference between the core and claddings is 0.36%, and the fibers were stripped of their jackets and placed in direct contact so that the spacing between cores was 125 μm. A motorized linear translation stage controlled the distance between the fiber ends and the lens, denoted by z_{fl} in Figure 4.1, and this controlled the beam divergence and hence the overlap between the power distributions of the transmitting fibers at the receiving plane. The transmitting power for each fiber output was set as 3 mW.

The receiver consists of a single, graded-index, multi-mode fiber aligned behind a single collecting lens (15 mm focal length, 12.7 mm diameter, 7.7mm radius of curvature,

plano-convex). Since the incident beam on the receiver was divergent in most cases, the curved side of the lens was placed towards the collecting fiber to minimize the spherical aberration. The fiber was connected to the power meter for reading. The receiver was assembled on a motorized stage and located 2.1 meters from the output lens of the transmitter.

4.3 Results

Both experiments and simulations were performed with certain link parameters held constant. For all of the wavelengths used, the receiver was assumed to have a threshold for error-free operation of -31.4 dBm, which is the threshold value obtained for the BER test equipment, operating at 1310 nm, OC-48 / 2.5G SONET in bit rate, used in the laboratory.

4.3.1 Experimental Results

For the experiments, the power received by the collecting fiber was recorded as the number of transmitter fibers, the fiber-to-lens distance at the transmitter, wavelength, and the lateral alignment between the transmitter and receiver were varied. The results are compiled in Figure 4.2. In Figures 4.2 (a) and (b), the 1310 nm wavelength was used, and the 1550 nm wavelength was used for the results in Figures 4.2 (c) and (d). In some cases, only one of the coupler outputs was connected to the central fiber in the transmitting array, while in other cases all of the transmitting fibers were connected to coupler outputs. The results are normalized by the highest collected power in order to more easily compare the experimental results to the theoretical results. Only data points

for which the collected power was above threshold for an error-free link are plotted in the graphs.

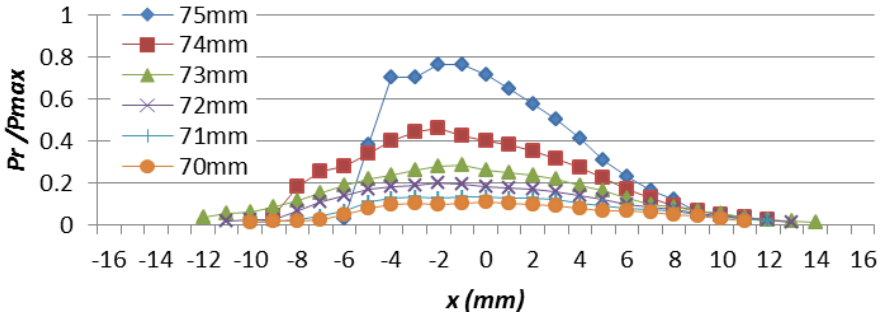

(a)

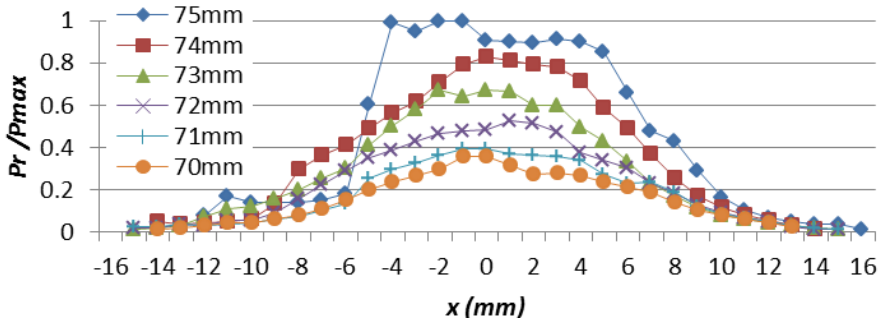

(b)

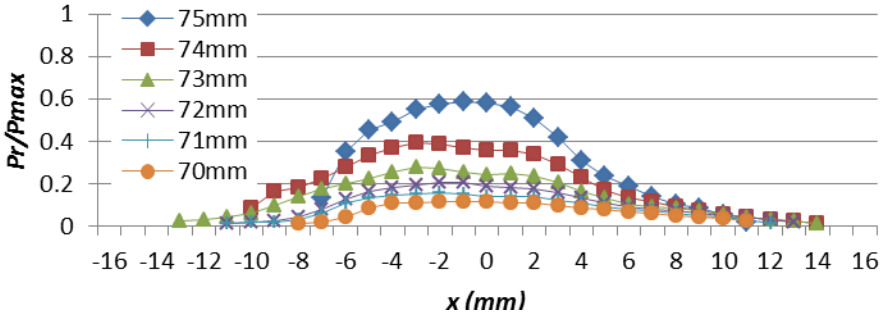

(c)

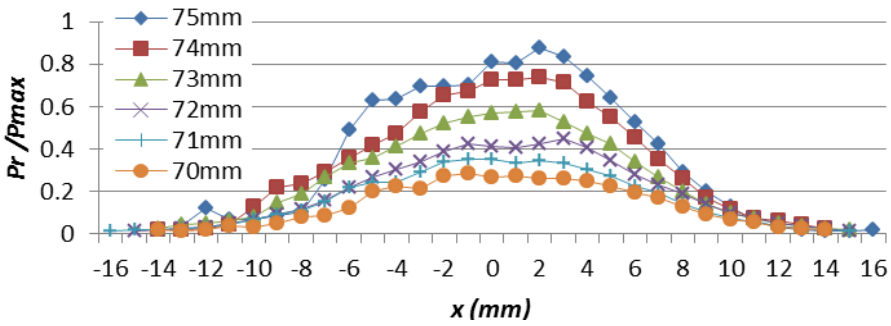

(d)

Figure 4.2: Received Power Measured Experimentally with Different z_{fl} Values for (a) one transmitter output at 1310nm (b) three transmitter outputs at 1310nm (c) one transmitter output at 1550nm (d) three transmitter outputs at 1550nm.

From the experimental data, several trends are observed that are expected to appear in the simulation output to verify that the simulation is an acceptable model of the FSO system. First, the range of *x* for which the collected power is above threshold (called the coverage range from here on out), and the peak collected power, should be larger when three fibers are lit simultaneously. Second, the coverage range should first increase, then decrease as the distance between the fiber tip and the lens decreases. This indicates the trade-off between larger area illuminated and lower local power that occurs as the beam divergence increases. Third, the coverage range should, in general be larger for 1550 nm than for 1310 nm when all other aspects of the system are held constant

4.3.2 Simulation Results

The results obtained for simulations performed using the exact same parameters as the experiments are shown in Figure 4.3.

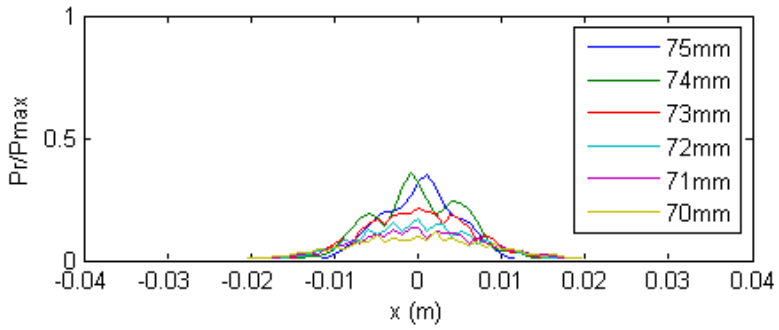

(a)

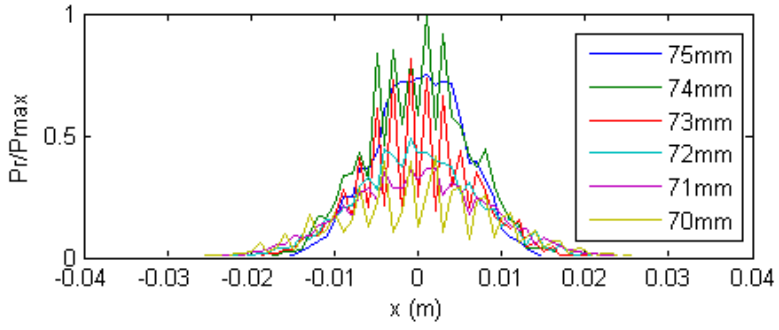

(b)

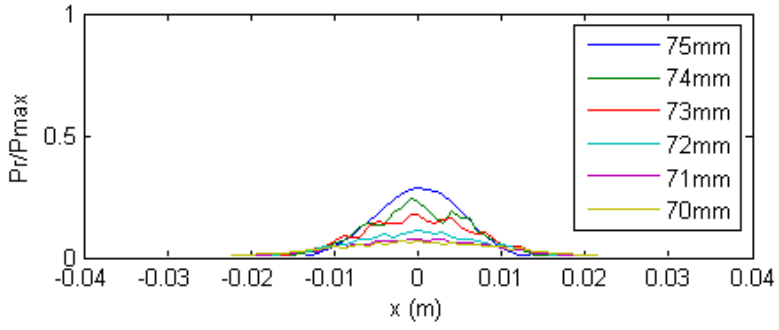

(c)

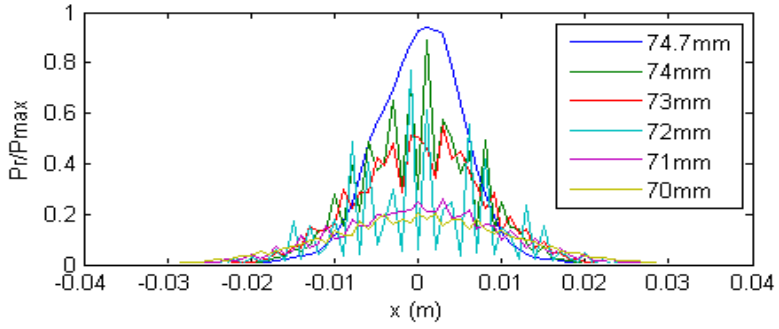

(d)

Figure 4.3: Collected Power Simulated with Different z_{fl} Values for (a) one transmitter output at 1310nm (b) three transmitter outputs at 1310nm (c) one transmitter output at 1550nm (d) three transmitter outputs at 1550nm (z_{fl}=74.7mm).

The simulation results are found to compare favorably to the experimental data. The coverage range and peak power are calculated to be larger for the three-fiber case compared to the single-fiber case, validating the first targeted trend. For the simulation results, the range of z_{fl}'s, combined with the difference in effective focal length, did not allow the trade-off between larger area illuminated and lower local power to be observed, as the trend towards smaller coverage area occurred at larger z_{fl}. It must be noted that, in Figure 4.3(d), the effective focal length of the coupling lens in the simulation was 0.3 mm shorter than that encountered experimentally, which is why the maximum z_{fl} = 74.7 mm for the simulation. This difference occurs due to assumptions made in the theoretical derivations about the light emanating from the fiber ends and in the modeling of the coupling lens itself. The coverage range for 1550 nm was slightly larger than that for 1310 nm, as most easily observed by comparing Figures 4.3(a) and (c), which correlated with the experimental data. While unexpected, the magnitude of the coverage range also compared favorably with the experimental data, indicating that the model used for the receiver optics was of useful accuracy. Based on these comparisons, the model was deemed sufficiently accurate for investigating the performance of the overall system as key parameters were changed without further experimental verification.

4.3.3 Simulation Extending to Other Conditions

For the extended simulation study, more key parameters were varied, most notably the wavelength of the transmitter, and the performance of the link was evaluated for each combination of parameters. The wavelengths studied were 850 nm, 1310 nm,

and 1550 nm. Besides wavelength, the key parameters investigated were the fiber-to-transmitting lens distance z_{fl}, the distance between the transmitter lens and the receiver lens z_L, the number of transmitting fibers, the transmitter power P_t, and the number of lenses along the horizontal axis of the receiving lens array. Note that the distance between the output surface of the receiving lens and the input surface of the collecting fiber was always set equal to f_{Rx}, and therefore the distance was different for each wavelength used. For consistency with the experiments, when more than one transmitting fiber was used, the total power available from the optical source was divided equally between all of the transmitting fibers in use.

The transmitting lens was biconvex with a focal length of 50 mm at a wavelength of 1550 nm. The lens array at the receiver consisted of plano-convex lenses lined up along the horizontal axis, with each lens having a focal length of 3 mm, radius of curvature of 1.143 mm, and center-to-center spacing of 2.286 mm. The lenses used were based on one of the experimental systems used in the laboratory.

For analyzing the link, the parameter chosen as a figure of merit was the coverage area. Here, the coverage area is defined as the area over which the receiver can be moved, transverse to the optical axis, and receive a power greater than the -31.4 dBm threshold power assumed for error-free communication. The simulation output produced a grid of points, with each grid square having a dimension of 5 mm by 5 mm, or an area of 25 mm^2. For each square in the grid, the average power over the grid, calculated from the values at the four grid corners, is compared to the minimum value of -31.4 dBm (0.724 W). If the average power of the grid square equals or exceeds this value, 25 mm^2 is added to the total coverage area available to the link. The grid squares that meet or

exceed the threshold level are counted, and the coverage area obtained by multiplying the number of grid squares by the area of the squares. For the initial comparison, whether or not the grid squares meeting the minimum criteria were spatially contiguous (no gaps between squares) was not considered.

The results of the simulation are shown in Figures 4.4 through 4.7. In Figures 4.4, 4.6, and 4.8, the coverage area is plotted as a function of the key parameters mentioned previously, and is also dependent upon the number of collecting lens-fiber pairs used at the receiver. A common trend amongst all of the results is the appearance of two optimum points, one with respect to distance and one with respect to divergence. For larger divergence (z_{fl} → 48.25 mm) a clear maximum is observed at shorter distances, with the optimum distance increasing with increasing optical power collected (either more transmitted or more collecting lenses) and decreasing wavelength. A second maximum in the coverage area occurs at longer distances for beams with little divergence (z_{fl} → 50 mm), as might be expected from recent long-distance communication trials [38, 39, 42].

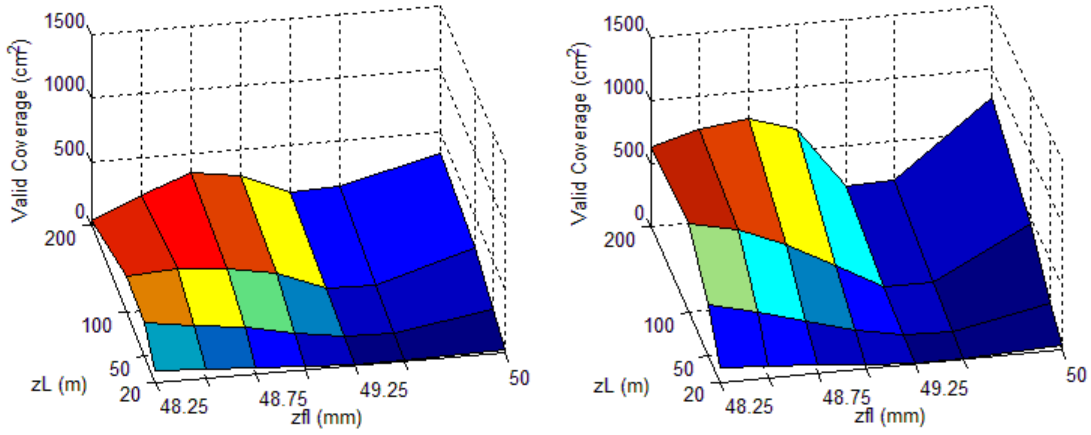

(a) (b)

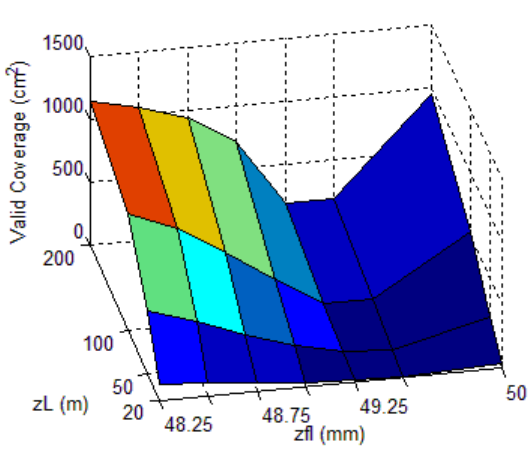

(c)

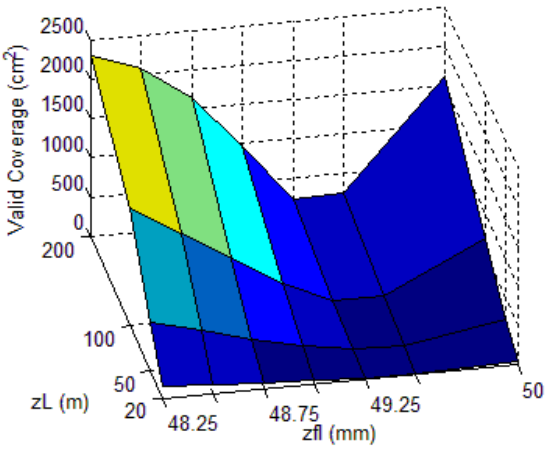

(d)

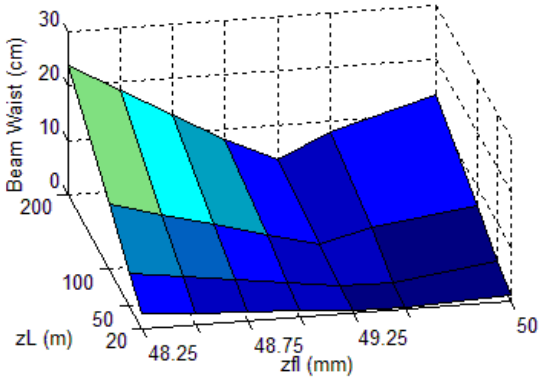

(e)

Figure 4.4: Coverage Area at 850 nm. (a) 2mW, 3 lenses. (b) 5mW, 3 lenses. (c) 2mW, 7 lenses. (d) 5mW, 7 lenses. (e) Beam waist at 850 nm.

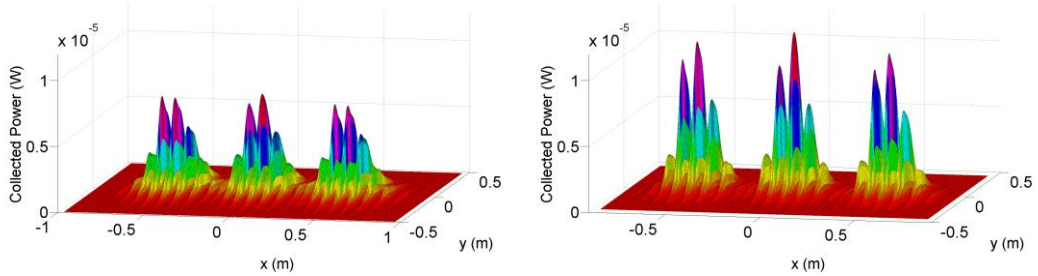

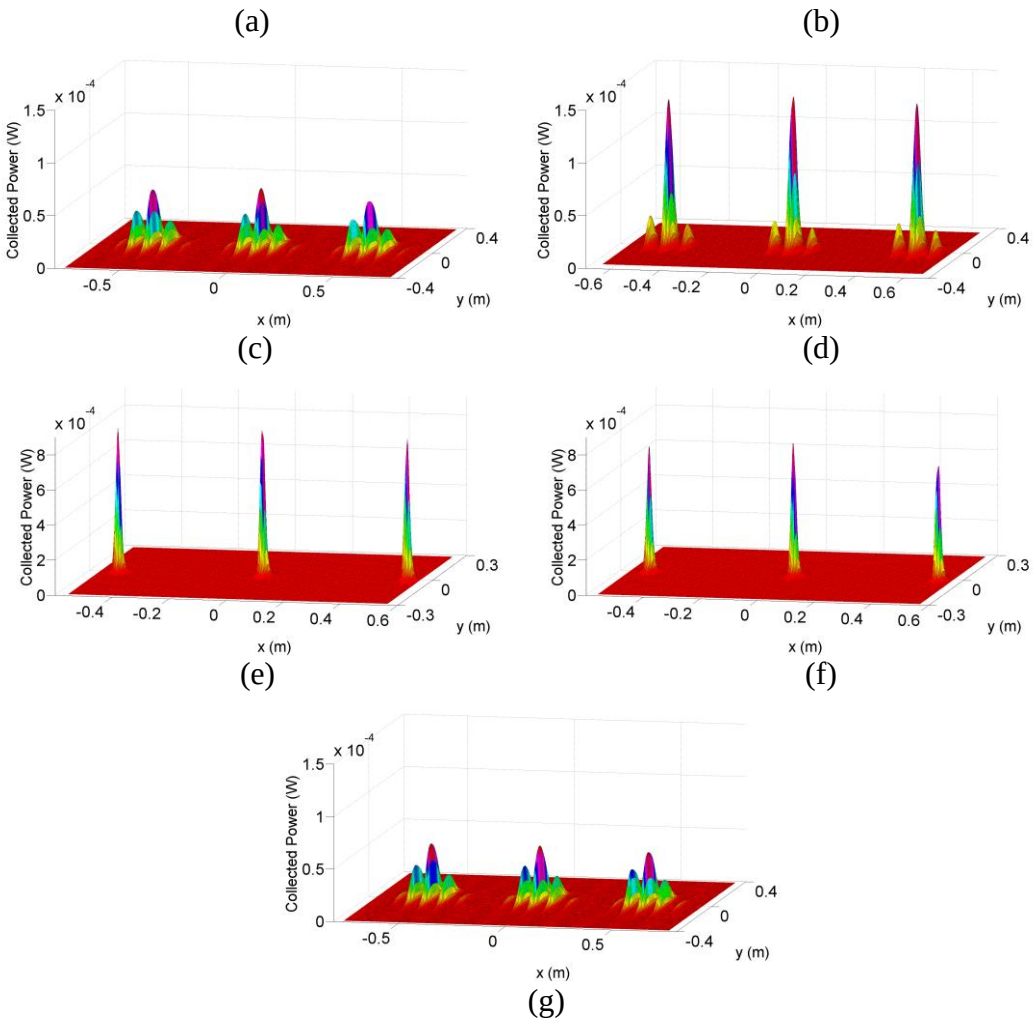

Figure 4.5: Calculated Power Collected by the Receiver at 850nm as a Function of Horizontal and Vertical Translation (lower left and lower right axes, respectively) of the Receiver's Optical Axis with respect to the Optical Axis of the Transmitter. For All Cases the Transmitted Power is 5 mW, z_L = 200 m, and Number of Receiver Lenses is 7. (a) z_{fl} = 48.25 mm. (b) z_{fl} = 48.5mm. (c) z_{fl} = 48.75 mm. (d) z_{fl} = 49 mm. (e) z_{fl} = 49.25mm. (f) z_{fl} = 49.5 mm. (g) z_{fl} = 50 mm.

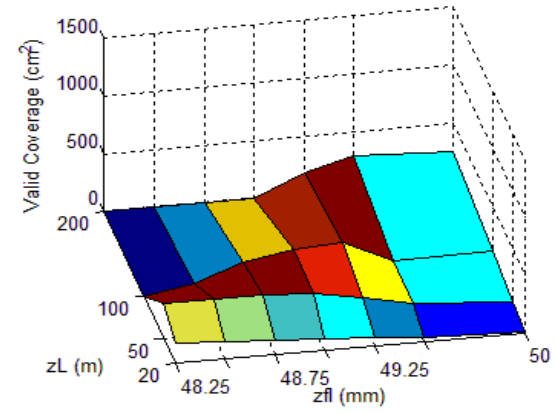

(a)

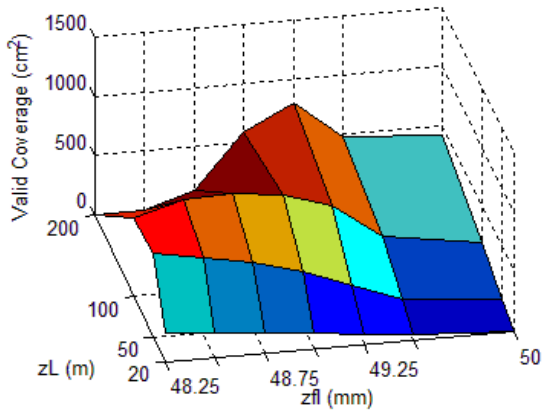

(b)

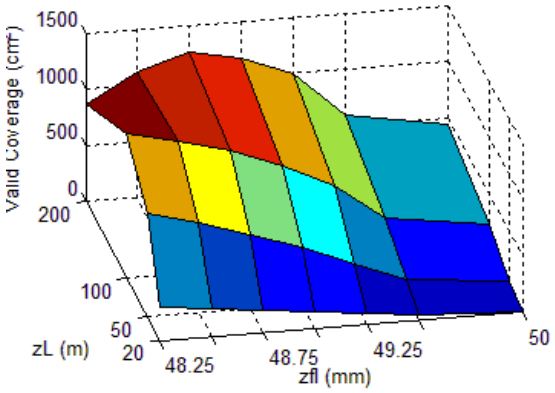

(c)

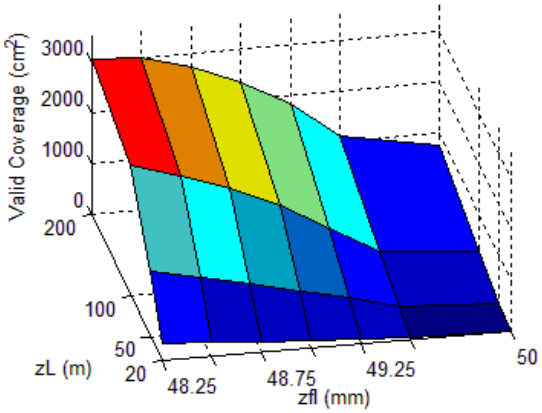

(d)

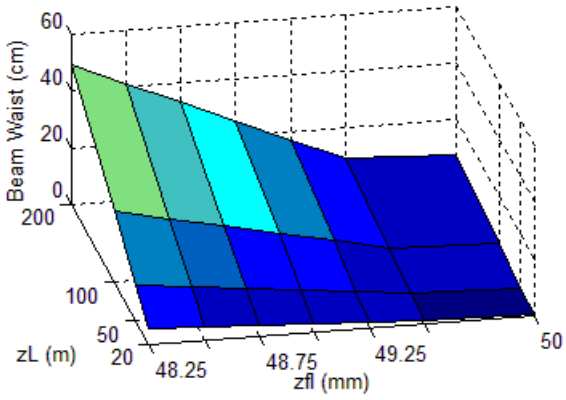

(e)

Figure 4.6: Coverage Area at 1310 nm. (a) 2mW, 3 lenses. (b) 5mW, 3 lenses. (c) 2mW, 7 lenses. (d) 5mW, 7 lenses. (e) Beam waist at 1310nm.

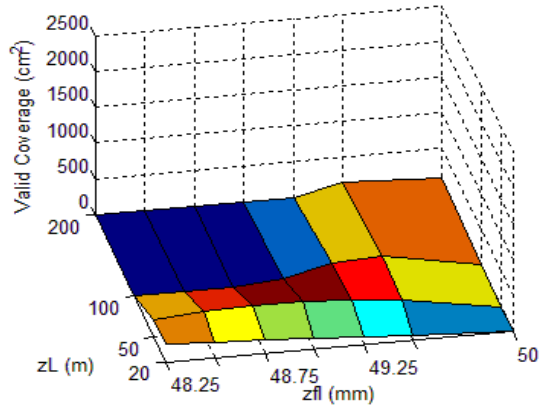

(a)

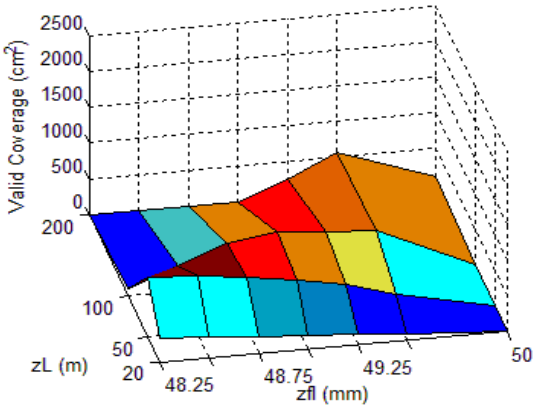

(b)

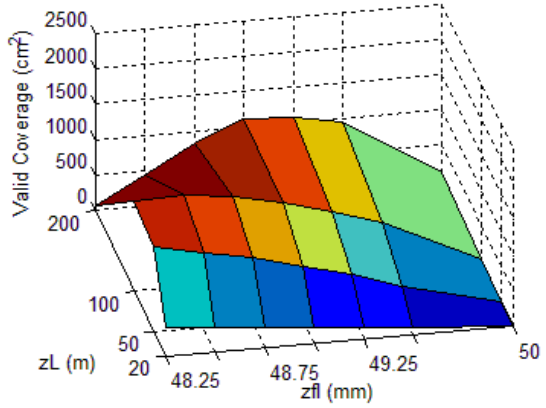

(c)

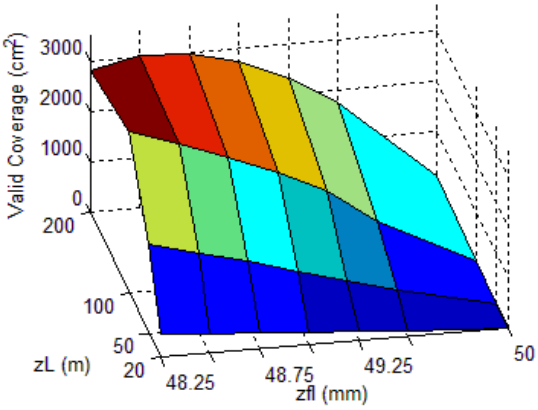

(d)

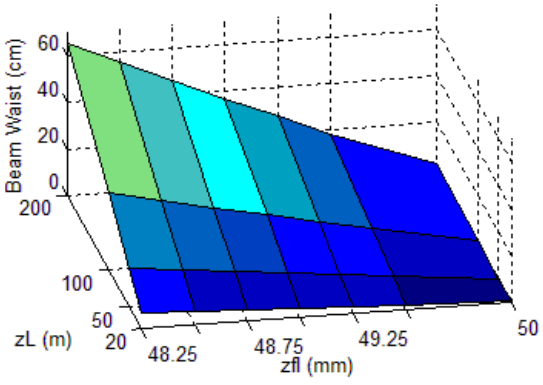

(e)

Figure 4.7: Coverage Area at 1550 nm. (a) 2mW, 3 lenses. (b) 5mW, 3 lenses. (c) 2mW, 7 lenses. (d) 5mW, 7 lenses. (e) Beam waist at 1550nm.

Of interest here is the transition between the two extreme cases. When the transmitting power is low or the collecting area is small, the optimum distance remains fairly constant for a wide range of beam divergence settings, as demonstrated in Figures 4.7(a), 4.6(a) and 4.6(b), and then increases sharply when the fiber output is very near to the focal length of the transmitting lens. When the collected power is large, the optimum distance shifts in a more gradual parabola with a change in divergence. This dynamic would be more favorable from a control perspective, as more gradual changes are easier to implement than large discrete changes. An object that was not only moving laterally to the transmitter but also moving towards or away from the transmitter would be easier to track, and thus the link more easily maintained, when the collected power is optimized.

Throughout the prior discussion, the focus was on the magnitude of the coverage area, and the contiguity of the coverage area was neglected. Figure 4.5 provides information on contiguity in relation to the numerical magnitudes in Figure. 4.4. The conditions for the plots in Figure 4.5 correspond to the back edge of the plot in Figure 4.4(d). It is observed that, as the magnitude of the coverage area decreases, in general the contiguity also decreases. While there is some overlap between the beam distributions in Figures 4.5(a) and (b), there appear dead spaces between the distributions where no link can be established. Therefore, when defining the control curve that links the transmission distance and the beam divergence, it is crucial to also consider whether the contiguity of the power distribution is maintained throughout the control curve. It needs to be noted that, due to index dependence on wavelength, the focal length was smaller for 850nm wavelength, and this is why in Figure 4.5(g), the beam starts to spread again at $z_{fl} = 50$ mm, which then caused a sharp coverage increase shown in Figure 4.4 at this z_{fl}.

The contiguity is also affected by the beam deflection angle created by the separation between the transmitting fibers and the design of the optical telescope used at the transmitter. Instead of using a single transmitter lens, as was the case in this study, a transmitting telescope consisting of multiple lenses can be used to concurrently design the beam divergence range and the beam deflection angle to optimize contiguity and smooth the control curve for targeted ranges of transmission distance. For example, in Figure 4.5, if the deflection angle was changed such that the center of the power distributions for each transmitting fiber were now 0.25 meters apart, contiguity could be maintained for a wider range of divergences and optical powers. The price for this increase in contiguity is a reduction in the coverage area achieved. The designer must strike a careful balance between these parameters to achieve the most effective design of the link.

Although the analyses in this work focused primarily on commonly-used wavelengths for telecommunication, there exists interest in using other wavelengths for mitigating the effects of weather and turbulence. The simulation equations can be used in a manner similar to that employed here to determine the appropriate choices of transmitter power and divergence to maintain a viable link. The main limitations in using shorter or longer wavelengths appear to be ones of practical implementation. Earlier work [40, 41] indicated that far infrared wavelengths, for example in the 3400 nm range, would have benefits in this regard. The primary limitation of this wavelength range is the high absorption of glass in this region, and thus a single system that incorporated both the far IR and other wavelengths together would require optics (and fibers) that have low loss at these wavelengths, for example those based on ZnSe. The concern would be the

increased cost of using such components over fairly low-cost glass optics and fibers. For wavelengths below 850 nm (visible up through the commonly available 780 nm), one concern is the increasing susceptibility to even relatively small refractive index eddies caused by turbulence in the atmosphere. Another issue is that these wavelengths, particularly in the visible, often require a different detector material (Si for visible, GaAs, etc. for mid to far infrared), and so two paths would be needed, or some other accommodation, to allow smooth switching between wavelengths without incurring signal drops of long duration. Therefore, to use these other wavelength ranges, implementation challenges must be solved before the use of these ranges becomes practical.

4.4 Summary

In this chapter, a numerical simulation was described and used to investigate how the link length, beam divergence, transmitted power, and the number of collecting lenses at the receiver interact and influence the design and control of a mobile FSO link. The power distribution of the transmitted beam at the receiver input plane provides an upper limit on the coverage area attainable for the link. The optical power available at any point within the distribution determines what percentage of the maximum coverage area is actually available for establishing error-free transmission between the transmitter and receiver. The results suggest that the link can be designed or controlled to operate at the absolute optimal set of parameters, corresponding to the largest possible coverage area, or to operate error-free despite variations in the operating parameters in order to reduce the physical and control demands of the optical systems. Preliminary experimental work has

demonstrated some of the basic features observed in the simulation calculations. More extensive application of the simulation is needed to provide more comprehensive understanding of the total system behavior, and further experimental work is needed to verify and fine tune the simulation.

Chapter 5

Control Algorithm Development for Mobile FSO Nodes Alignment

This chapter investigates a novel control algorithm within different transmitter designs in FSO mobile networks. The fiber bundles are utilized so that the beam deflection properties of a lens can be exploited to affect beam steering. After acquiring and processing the data from GPS, a fisheye alignment assistance system and the receiver, the adaptive control system would help track the mobile receiver and providing optimum coverage over the target area. The performance of a first implementation of elements of the proposed control algorithm is evaluated. Feedback from the receiver node was used by the transmitter to make decisions on which elements of the transmitting fiber array were chosen to deliver power. The efficacy of the control algorithm in maintaining a viable connection between the transmitter and receiver is investigated as a factor of both transmitter and control algorithm parameters. The results provide guidance for further development and design of both the transmitter and the control systems to improve the overall performance of the link.

5.1 Overview of DAWN System Alignment Levels

A conceptual diagram of a DAWN system using two mobile nodes is shown in Figure 5.1. A propulsion system in manual mode allows the system's ground operator to make directional adjustments and manipulate flight from one GPS waypoint to another. Data are transmitted to the fixed network via FSO, WiFi, or Cellular network, respectively.

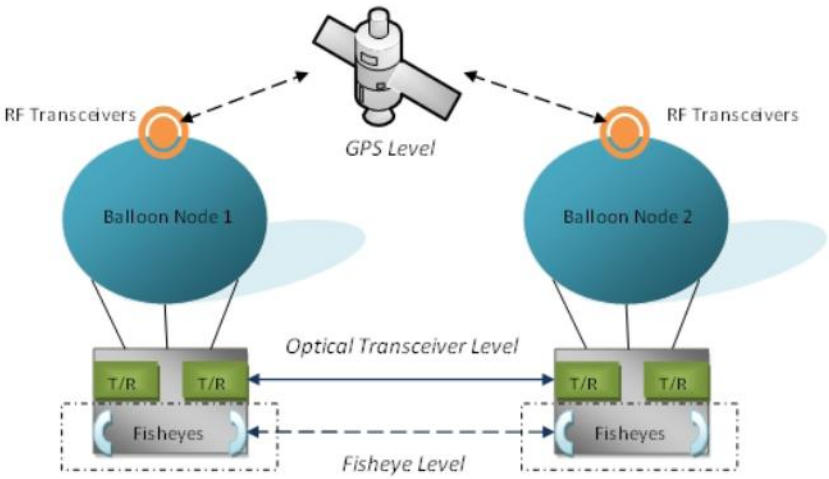

Figure 5.1: Overview of DAWN System Alignment Levels

On the basis of expected accuracy, the FSO alignment system can be divided into three levels. The first level is the GPS level, which collects and processes the location information for each node from GPS satellites. The GPS data for potential target nodes is either obtained from a GPS data repository (satellite or other stable node fixture) or from exchanges between the nodes over an RF management channel. Knowledge of the node locations enables the Balloon Control System (BCS) to initially adjust the balloon orientations to roughly align the respective transceivers. At the second level, an optical alignment system based on a standard fisheye lens and quadrant detector, simply referred to as the fisheye system, provides a method to obtain the data required to make finer alignment modifications. With an over 180 degrees field of view, a fisheye lens has the ability to capture incoming beams from a larger range of directions than optical transceiver lenses. The output from the electronic quadrant detector guides the BCS and Optical Control System (OCS) to correct alignment. The third level of alignment is the optical transceiver level which directs the last step of alignment through beam control. By

adjusting the beam divergence and achieving optical beam steering in a small physical space, the link can exhibit a greater tolerance for alignment error by providing a sufficient link budget over a larger spatial volume. In this work, it is assumed that optical fiber bundles combined with appropriate optical components choices are used [11]. This design is able to generate continuous coverage of a target area without the weight and stabilization issues of mechanical systems.

According to the optical components in use, the relevant designs are organized into three basic groups: "All Couplers" designs, "All Switches" designs and "Couplers/Switches Hybrid" designs. "All Couplers" designs distribute optical power over all of the seven fiber outputs, meaning that the maximum beam coverage can be achieved at the target area without switching between fibers, preventing switching time from becoming an issue. Figure 5.2(a) illustrates one "All Couplers" design, which contains a single power source working with one 1×8 coupler. As Figure 5.2(b) shows, "All Switches" designs concentrate the optical power to only one fiber output so that the highest power density can be achieved at the receiver and there is no unnecessary power loss to the other fiber outputs that do not connect with the receiver. The benefits that are achieved are a result of the switch's ability to steer the signal. One of the "Couplers/Switches Hybrid" designs in Figure 5.2(c) consists of a single power source, one 1×2 switch and two 1×4 couplers. This kind of design is expected to combine the larger beam coverage from the "All Couplers" design and lower power loss from the "All Switches" Design.

Prior investigations of these designs [11] demonstrated that, in general, a coupler and switch combination provided the best compromise of power budget and tracking

time. Some applications, however, would be best served by an all-coupler or all-switch design, depending on whether power or switching speed is the dominant factor.

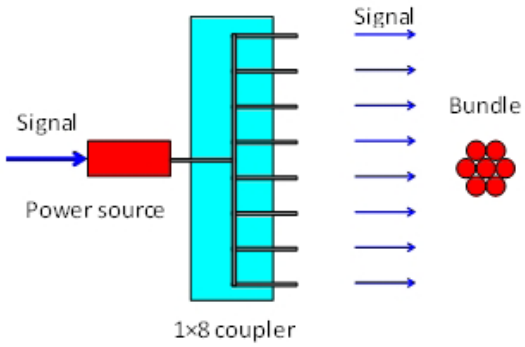

(a)

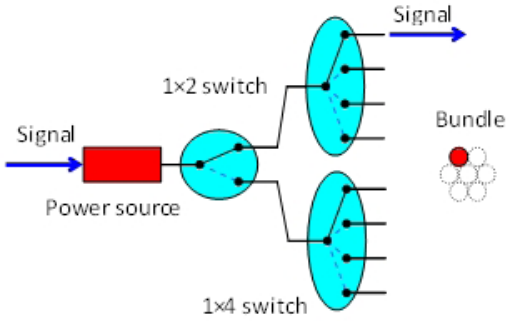

(b)

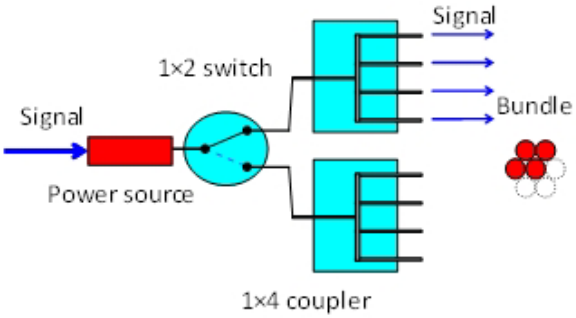

(c)

Figure 5.2: Transmitter Designs(a) “All Couplers” Design, (b) “All Switches” Design, (c) “Hybrid” Design.

5.2 Control Algorithm

The optical control algorithm contains three phases in sequence: System Starting, Finer Correction and T-R Link Checking. Figure 5.3 shows the optical alignment control flow chart.

5.2.1 Phase A: System Starting

At the System Starting phase, the distance *L* between the two mobile nodes is calculated with the information collected from the GPS location data for each balloon, and then an optimal fiber-lens distance at the receiver is selected that optimizes the likelihood of a successful connection based on the value *L*, the specifics of the particular transmitter design and a particular link acquisition strategy. While these adjustments are taking place at the optical transceiver level, the BCS takes action to adjust the orientation of the balloon (or other relevant platform) to achieve a basic level of alignment between the transceivers. The control system must then wait for the BCS to stabilize on a final position before continuing the alignment process.

5.2.2 Phase B: Finer Correction

For the second phase, the fisheye systems are utilized to make finer corrections. The first step is to get the magnitude and direction of error as interpreted by the quadrant detector behind the fisheye lens. This action is taken for both nodes in the link, with each node acting only on its own information. For reference for this discussion, the plane of movement parallel to the ground is considered the x-y plane, and the direction perpendicular to the ground is the z axis.

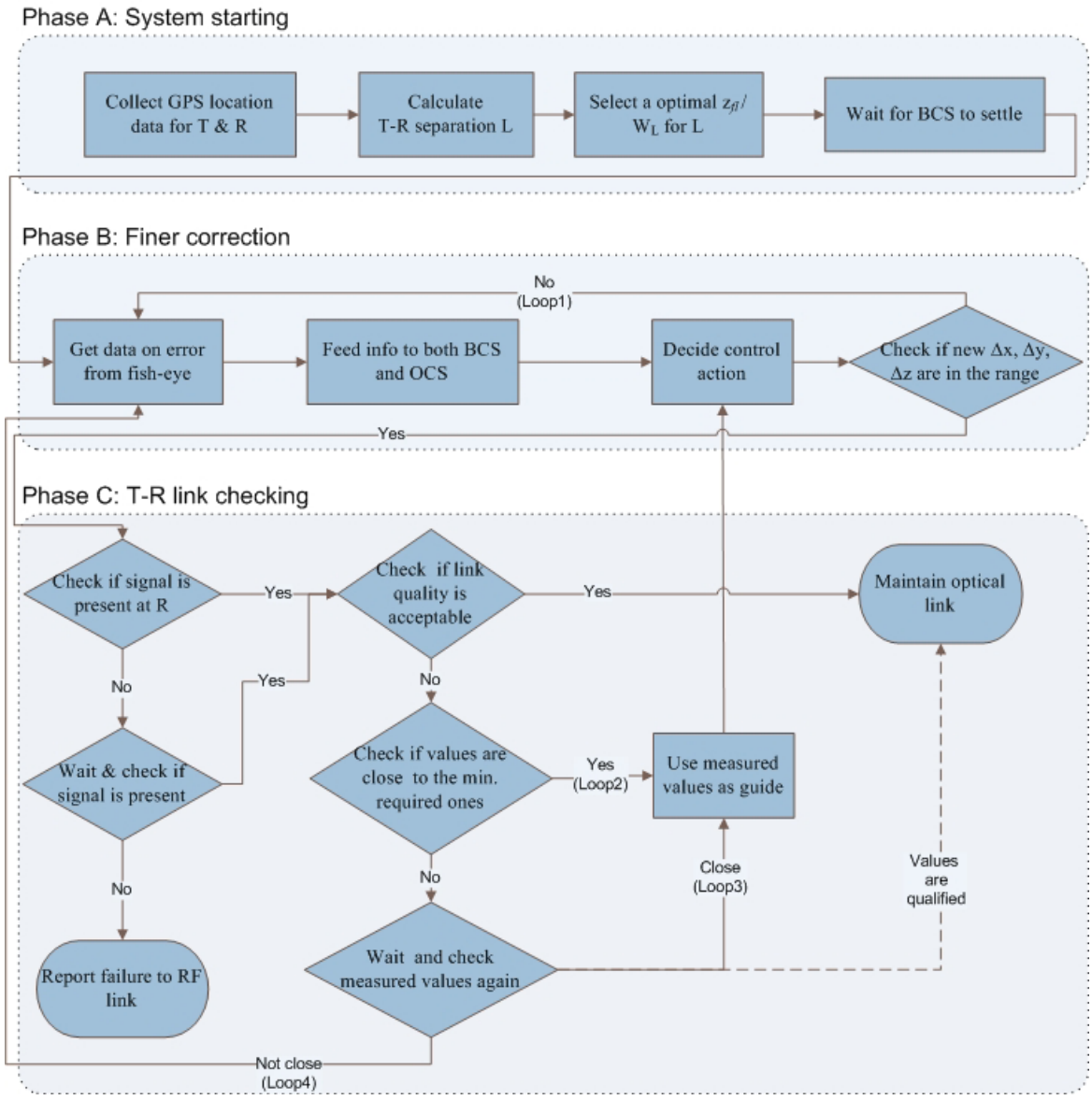

Figure 5.3: Control Algorithm Flow Chart

In the second step, the errors Δx, Δy and Δz, for the x, y, and z directions respectively, are calculated and fed to the appropriate controllers. The balloon adjustment is limited by the control components, and for this discussion movement is possible only within the x-y plane, so only the Δx and Δy data is needed for BCS. Since the OCS has

the ability to make adjustments in all directions, the OCS requires Δx, Δy and Δz information.

In the third step, the two control systems determine whether control actions will be executed by the respective system, and what the appropriate action should be. To determine which control system should take action, control boundaries are constructed that divide the control space. Two factors determine these boundaries: the dynamic range of the optical transmitter (switching angle, optical power, and optical divergence) and foreknowledge of which actions are potentially beneficial and which actions are self defeating. If the error calculation indicates that the corrective action required is outside the capabilities of the OCS, then the BCS is directed to act in an effort to achieve a better initial alignment condition. If the error calculation indicates that the corrective action is within the capabilities of the OCS, then action is requested of that system.

The final step is to check the fisheye system again to determine whether the new Δx, Δy and Δz values are within an acceptable range for transceivers. Here, an acceptable range is defined as a misalignment that is within the tolerance of the link design and for which a successful link is therefore likely to occur. If the misalignment is tolerable, then the system can proceed to the next phase; if not, the system updates the error information through quadrant detector and returns to the first step in the cycle.

5.2.3 Phase C: T-R Link Checking

The first step in this cycle is to determine whether a viable link is available for transmission.

If a signal is present at the receiver, then the link quality is checked by measuring the received power Pr, the bit error rate (BER) and the optical signal-noise ratio (OSNR). If the quality is acceptable, the fisheye system and the procedure in Phase B is used to maintain the FSO link. Additional steps may be added to provide a predictive capability, where successive position readings, along with any motion related data provided by the GPS unit, are used to determine control actions in advance, with the goal of minimizing gaps in the link up-time.

If the link quality is poor, it is determined whether the measured performance quantities are close enough (within some predetermined limit) to the minimum required values. If the performance is close, indicating that only minor adjustments are required to improve the link operation, the measured values are used as a guide to perform fine correction at OCS level. If the performance is too degraded, wait a short time and measure the performance again before taking any large-scale corrective action. The purpose of this short delay is to prevent major corrective action if the degradation in performance is caused by some temporary obstruction or event rather than an actual system misalignment.

If the new measured values are still not acceptable, then the control system returns to the Finer Correction phase to implement a more significant control action as needed. If signal is not present at receiver at all, wait for a predetermined time interval and then check again to see if a signal is present. If the signal now appears, follow the procedure just described. If there is still no signal a link failure report is generated to the network so that data can be sent over a different path until the optical link can be reconnected. Note that it is assumed that the fine correction, using the guide laser and the fisheye system,

would at least provide sufficient alignment to detect the presence of the transmitted beam energy, if not recover the signal. Therefore, it is acceptable to report a link failure when repeated attempts to detect the signal power fail.

5.2.4 Laser Beam Adjustment at OCS

At the Finer Correction phase, the details of the beam adjustments performed by the OCS depend necessarily on which of the transmitter designs have been implemented. Details of the process for each of the previously described designs are as follows.

Since the "All Couplers" design uses all of the fibers simultaneously, the main question is whether or not the existing misalignment places the target within or near the coverage area for which the ability to achieve a viable link is projected. If the target is within the coverage area, then no further control action is required, and the process can proceed to the link-checking phase. If the target is close to the edge of the beam coverage area, then the appropriate control action is to adjust Pt and/or z_{fl} to increase the coverage area slightly. If this is done properly, the new coverage area will now include the target location, and the system can now focus on link acquisition. The definition of close depends on the limits on the control system's dynamic range and the current state of the transmitter parameters. If the target position is deemed to be too far from the coverage area for acquisition by only the OCS adjustments, then control actions are requested from the BCS to perform corrections to the balloon orientation. The flowchart for this process is shown in Figure 5.4(a).

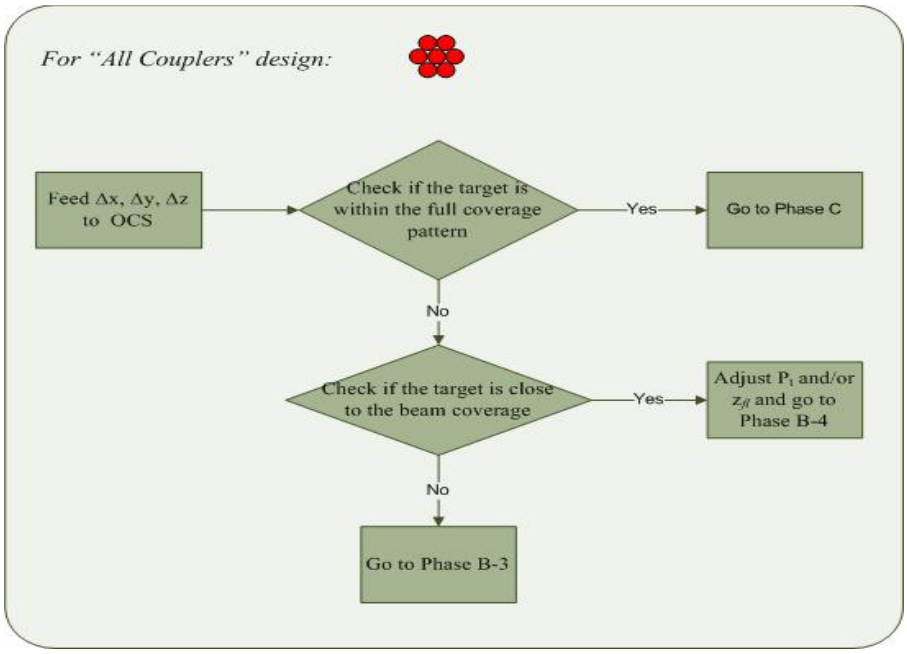
For "All Couplers" design:
Feed Δx, Δy, Δz to OCS
Check if the target is within the full coverage pattern
Yes
Go to Phase C
No
Check if the target is close to the beam coverage
Yes
Adjust P_t and/or z_{fl} and go to Phase B-4
No
Go to Phase B-3

(a)

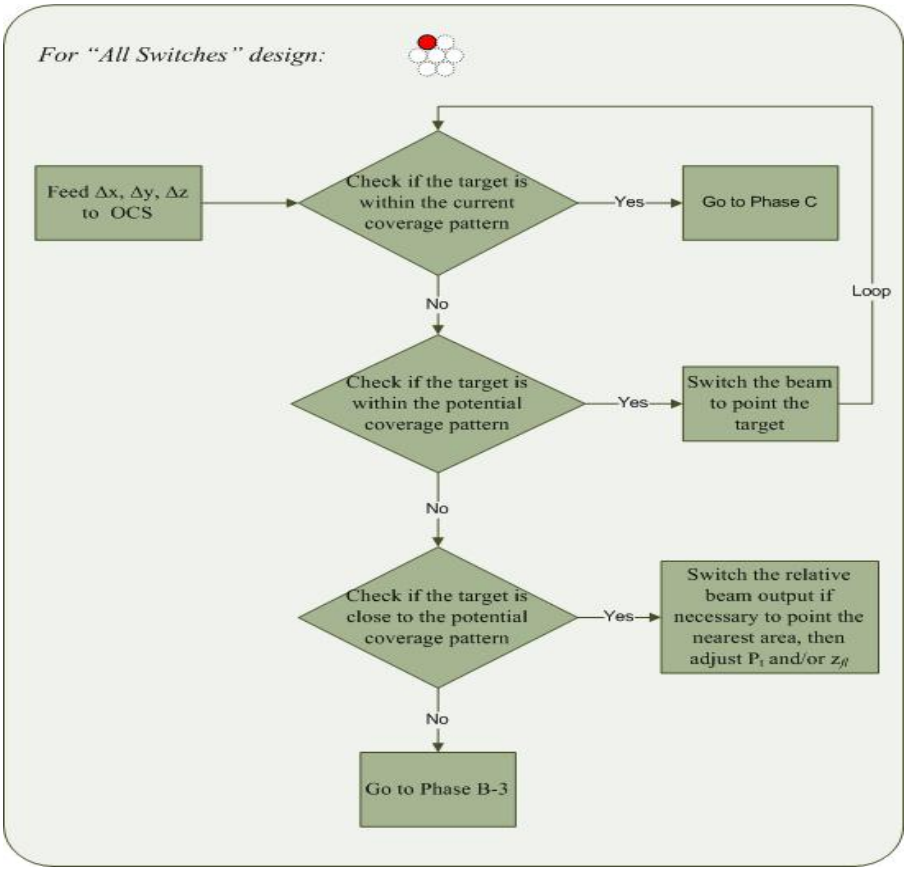
For "All Switches" design:
Feed Δx, Δy, Δz to OCS
Check if the target is within the current coverage pattern
Yes
Go to Phase C
No
Loop
Check if the target is within the potential coverage pattern
Yes
Switch the beam to point the target
No
Check if the target is close to the potential coverage pattern
Yes
Switch the relative beam output if necessary to point the nearest area, then adjust P_t and/or z_{fl}
No
Go to Phase B-3

(b)

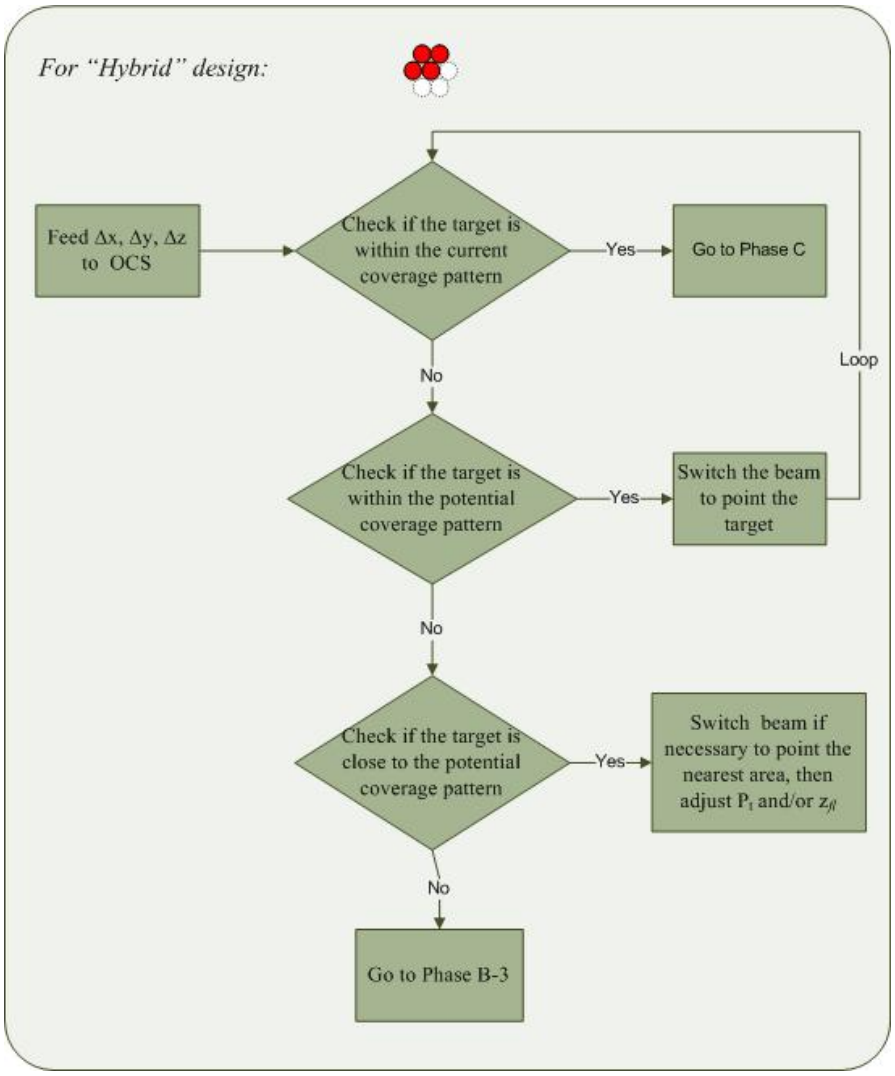

(c)

Figure 5.4: Control Flow for (a) "All Couplers" Design, (b) "All Switches" Design, (c) "Hybrid" Design.

For the "All Switches" design, the goal is twofold: choose the fiber most likely to direct the signal toward the target location, and adjust the beam divergence and power as necessary to insure a connection. Therefore, the first step is to check if the target is within the current coverage pattern as defined by which fiber in the bundle is currently lit. If the target is so positioned, then no further control action is required, and the process can proceed to the link checking phase. Some adjustment of the beam power and divergence

may be required if the target location is located at the very edge of the coverage area, since switching to a different fiber will only put the target on the edge of that fiber's coverage area. If the target is not within the current coverage area, a quick calculation determines which fiber of the transmitter bundle would cover the target's location. This calculation includes the potential coverage pattern of each fiber, as determined by the outer limits on beam divergence and transmitter power. If the target lies within the coverage area of one of the fibers in the bundle, then the optical power is switched to that fiber and necessary adjustments to the transmitted beam are made. If the target is outside of the potential coverage area, then control actions are requested from the BCS. A flowchart of this process is shown in Figure 5.4(b).

For the "Hybrid" design, the control process is necessarily a hybrid of the processes for the other two design choices. The first step is to check if the target is within the current coverage pattern determined by which fibers are lit and the optical beam parameters currently in use. If so, then no further control actions are necessary and the process can proceed to the link checking phase. If the target is not in the current coverage pattern, the next choice is to determine whether the target is close enough to the current coverage pattern that allowable changes in the beam divergence and power would capture the target within an expanded coverage area. If this is so, then the OCS makes the necessary changes and beam acquisition can proceed. If not, the control algorithm determines if there is another setting of the switches that produces a coverage pattern that potentially includes the target. If such a setting exists, the OCS sets the necessary switches and adjusts the beam parameters to capture the target within the coverage area

of the transmitter. The exact details of the switch settings depend on the combination of switches and couplers used in the transmitter design. For the simplest case shown in Figure 5.2(c), the control system only has to choose from two possible switch positions. There is necessarily a trade-off in the "Hybrid" design, as more switches reduce the power splitting losses of the couplers but increase the complexity of the control process. If the target is outside of the potential coverage area for any switch combination, then control actions are requested from the BCS. A flowchart of this process is shown in Figure 5.4(c).

5.3 Initial Evaluation

The initial evaluation of the control process was performed theoretically by projecting its performance in a generic scenario. For this scenario, a unidirectional link was assumed, where one node was attempting to transfer data to a target node. For initial assessment, the transmitting node was considered strongly tethered, so that any movement of the node was negligible with respect to the errors inherent to the GPS system. A GPS error of 3 meters was assumed. The target node was allowed to move, whether due its own propulsion or in response to wind forces acting on the node. The effects of atmospheric turbulence were not accounted for in the initial assessment. At this stage, several key parameters impacting the success of the control system have been identified.

One key parameter is the rate at which the nodes update their GPS data with adjacent nodes in the network. This directly impacts the initial success of the BCS in effectively aligning the transmitter optics toward the receiver. Depending on the timing

of a link request and the velocity of the target's motion, it is quite possible that the transmitter will be directed such that no connection between the transmitter and target is possible, even if both nodes are functioning properly. A long delay between updates also adversely impacts attempts to track the target node, making control difficult and the link unreliable under all except the best of operating conditions, regardless of the speed of the controller.

A second key parameter is the error inherent in each of the positioning and data systems with which the control system interacts. A primary source of error is the accuracy of the GPS data. The 3-meter error assumed is quite significant for FSO links of even relatively short distances, even with the larger coverage areas available with advanced receiver designs. Additional sources of error include the accuracy of the BCS (determined by the BCS control algorithm and the limitations of the mechanisms used to move the platform) and smaller error sources in the optical systems under the OCS jurisdiction. Even if the BCS and OCS are able to point the transmitter exactly at where the target is thought to be, the cumulative errors can cause the target to be missed.

The implication is that an additional control sequence must be added to the proposed algorithm to allow the control systems to perform some sort of search for the target node. The control calculations must be amended to account for the range of target locations, as dictated by the error expected, rather than assume that the target location is uniquely defined by the GPS data. The details of the search and the control level at which it is implemented depend on what search options are selected. The most direct search method would involve larger movement of the platform through the existing control options, with the BCS as the primary director. An alternate approach is to have the

optical components mounted below the platform with a separate pointing control such as a gimbal or motor. Whether this search is controlled by the OCS or by the BCS depends on where the search process is situated within the overall control algorithm and whether it is coupled with a beam power and/or divergence adjustment.

Accounting for these key parameters requires significant adjustments to the nature of the proposed control algorithm. These adjustments are in the process of being implemented, and a more rigorous, simulation based assessment of the algorithm is planned once these adjustments are completed.

5.4 Experimental Evaluation

The experimental system and its attendant control components used in the evaluation are shown in Figure 5.5. A bit-error-rate tester (BERT) operating at 1310 nm wavelength and SONET protocols was used as the signal source and signal sink for the link, and provided link analysis functions for the evaluation. The output from the BERT transmitter was passed through an amplifier to control the transmitted power and then delivered to a switching fabric to affect beam steering.

The transmitter consists of three single-mode fibers cemented together in a linear configuration, a coupling lens (biconvex, 75mm focal length), and micropositioners to control the alignment between the fiber ends and the lens. Each fiber in the transmitter is connected to one output of the switching fabric so that only one of the fibers can transmit optical power at any time. The switch fabric consisted of cascaded 1x2 electro-mechanical switches, and the connectivity is shown in Figure 5.6. A motorized linear translation stage controlled the distance between the fiber ends and the lens, denoted by

z_{fl} in Figure 5.5, and this controlled the beam divergence and hence the overlap between the power distributions of the transmitting fibers at the receiving plane.

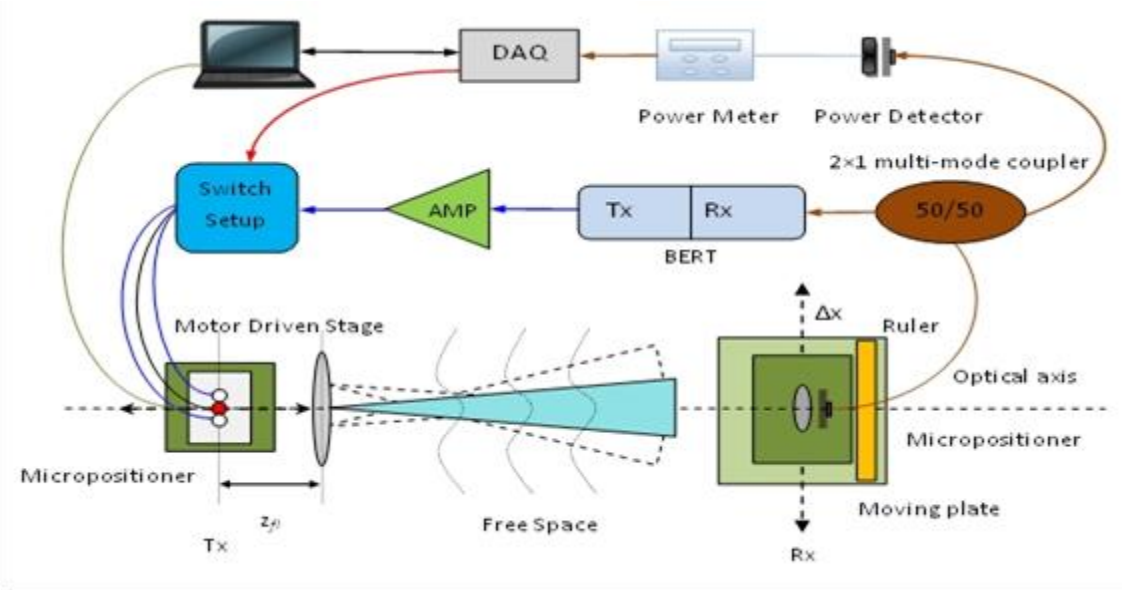

Figure 5.5: Configuration of System Showing Major Transmitter, Receiver and Control Components.

The receiver was kept simple in construction for the study, and consisted of a single, graded-index, multi-mode fiber aligned behind a single collecting lens (20 mm focal length, 12mm diameter, biconvex). The curved side of the lens was placed towards the collecting fiber to minimize the spherical aberration due to divergent incident beam in most cases. The fiber was the input arm of a 1x2 multi-mode coupler with 0.5 splitting ratio. One output of the coupler was connected to the receiver side of the BERT to complete the link, while the other output of the coupler was coupled to a detector to provide a monitoring input for the control system. The receiver was located 1.95 meters from the output lens of the transmitter.

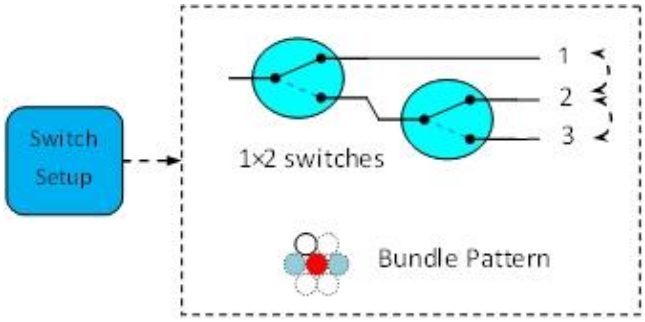

Figure 5.6: Details of Transmitter Switch Fabric.

The control system consisted of a power meter and detector for collecting power, a digital acquisition board (DAQ) for interfacing with a laptop computer, and control connections between the DAQ and the switches in the switch fabric. The data collection, data analysis, and control algorithm were implemented on the laptop using LabView. The power delivered to the detector by the output coupler was converted to power values by the meter and these values were sampled through the DAQ by LabView. The control algorithm, described in the next section, determined if and when the power from the BERT should be switched to a different transmitting fiber to re-establish the connection between the transmitter and receiver. LabView allowed several key aspects of the algorithm to be changed easily for analysis of their effects on the overall system.

5.5 Control Algorithm under Experimental Evaluation

5.5.1 Power Monitoring

The power collected by the receiver was monitored using the detector and power meter, which were calibrated prior to the experiment. The power reading was output by the meter as a voltage, and this voltage was sampled by the DAQ at rates of 12 kHz, 24 kHz, or 48 kHz. The samples were input into LabView and passed through an averaging

loop of variable length. The averaging loop was used to prevent switching from occurring due to one poor reading or to ensure that switching occurred even though one or two abnormally high power readings may occur. Averaging loops of 5, 10, and 15 samples in length were investigated. Noise sources that could produce errant readings include fluctuations in the transmitted power, particularly due to reflections in the transmitter path that impacted the amplifier, vibration in the optical components, and electrical noise within the detector and power meter. In a case where more than one transmitter fiber is emitting power, interference between overlapping beams may also cause power fluctuations. Turbulence was not a factor in the experiment due to the short distance and controlled laboratory environment.

5.5.2 Decision Making

Once an averaged power reading is collected from the detector, the reading is compared to a threshold power (P_{th}) to determine whether enough power is present at the receiver to maintain the link at a particular bit error rate (BER). The value of P_{th} can be chosen randomly or it can be determined experimentally. The experimental value is determined by scanning the receiver through the beam emitted by a single transmitter fiber and recording the collected power at which the link either exceeds a desired BER or the link fails completely. When using the BERT, a complete link failure is defined as the point where Unavailable Seconds (UAS) are recorded in the SONET protocol or a Frame Loss error is recorded, whichever is encountered first. When the collected power falls below P_{th}, the algorithm initiates a process for reconnecting the transmitter to the receiver.

5.5.3 Link Recapturing

The link recapturing process consists of scanning the transmitted beam over the receiver plane and determining which beam position recaptures the link above the desired BER. For the current transmitter design, the beam is scanned by selecting different fibers within the transmitting fiber array, as fibers aligned away from the center of the lens have their output deflected through an angle determined by their position with respect to the central axis and by the lens construction. Since no information regarding the direction of movement of the receiver is available to the transmitter for the current implementation, the transmitting fibers are illuminated in a fixed pattern, with fiber number two selected first followed by fiber number three and then fiber number one selected last. Figure 5.6 shows the fibers and their corresponding numbers.

As each fiber is illuminated, the power sampling and averaging process described previously is repeated. The average power collected is again compared to P_{th} to determine whether there is sufficient signal available to complete the link. If there is not, then the next fiber in sequence is illuminated. The attempt to recapture the link continues until either one of the transmitter fibers is able to recapture communication with the receiver or a set time for recapturing the link expires, at which point the control system determines that the link has failed.

5.6 Experimental Results

5.6.1 Experimental Procedure

At the beginning of each experiment, the initial alignment and calibration of the apparatus was performed. The axes of the transmitter and receiver were initially aligned

to produce the largest collected power, as measured by the BERT, when the center (on-axis) fiber of the transmitter array was illuminated at the focal point of Tx lens. The detector and power meter were then calibrated to produce the same power reading as the BERT. The receiver was then scanned to determine the value of P_{th} for the BERT for the given alignment. This value of P_{th} would be the minimum value entered into the control algorithm. A more appropriate value of P_{th} was determined by measuring the power distribution of each transmitter fiber at the receiver plane, and determining the most likely value of P_{th} needed to maintain the link. The power distribution was measured by recording the collected power from the detector as the receiver was scanned in fixed steps through the transmitted beam. Larger or smaller values might also be entered to determine how the choice of P_{th} impacts the control process and link performance. The receiver is then placed at one end of the stage's range to start the test and the control algorithm begins execution on the laptop. A single test consists of moving the receiver on its plate in random direction and speeds. For the tests reported here, the receiver's plate was moved manually, so that the exact speed of movement was different for each test, even if the intermediate positions in the movement sequence might be the same. The control algorithm was allowed to determine which of the transmitting fibers to be illuminated at any time during the receiver's movement. The BERT was used to monitor the status of the link and measure the time required to recapture the link once the decision to switch fibers was made by the control system. A set of tests consisted of repeating the basic single test as key parameters of the link and the control algorithm were systematically varied.

5.6.2 Experimental Results

The first experiment conducted was a single test where the receiver was moved over time and the status of the link monitored using the BERT. During the initialization of the experiment, the power distribution at the receiver due to each individual transmitting fiber was determined, and these distributions are shown in Figure 5.7. Note that transmitting fiber number one, which is to the right of the transmitter axis, has its beam deflected to the left side of the receiver, while transmitting fiber three, which is to the left of the axis, is deflected to the right side of the receiver, as expected. From this data and error information from the BERT, the value of P_{th} was set to -35dBm.

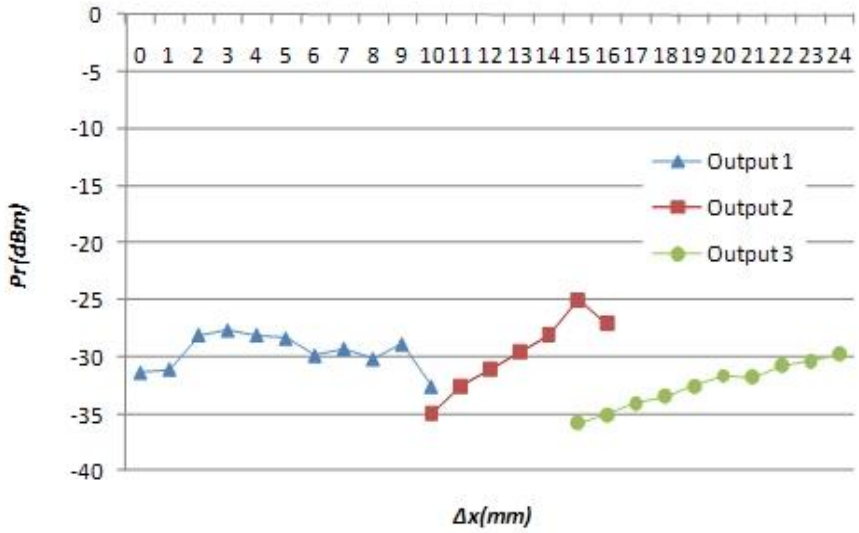

Figure 5.7: Power Distributions at the Receiver for the Three Transmitting Fibers

The control algorithm was then activated and the receiver motion initiated. Two aspects of the operation were then studied. First, the actual power measured by the detector as the receiver was recorded at each point as the receiver was moved. The result of a single pass from left to right is shown in Figure 5.8. At points where the power distribution from more than one of the transmitting fibers overlapped, the algorithm selected the fiber that

resulted in the larger collected power at the receiver. This result was repeatable as long as the power from one of the overlapping distributions was close to or below the value of P_{th}. If there was more significant overlap between the distributions, the algorithm did not switch to a fiber that might result in a higher collected power at the receiver as long as the power collected from the current fiber was above threshold. This behavior can be seen in Figure 5.9. The behavior is particularly noticeable in the transition between the center fiber (output 2) and transmitter fiber three (output 3). At x = 27 mm and 28 mm, the algorithm continues to collect power from the center fiber even though the power available from the side fiber is higher. The data in Figure 5.9 was taken using a source at 1550 nm wavelength coupled through a power amplifier rather than at 1310 nm, which accounts for the larger available powers in Figure 5.9 as compared to Figure 5.8. All of the data was taken for the case of a 48 kHz sampling rate at the DAQ and averaging of five power samples within the control algorithm.

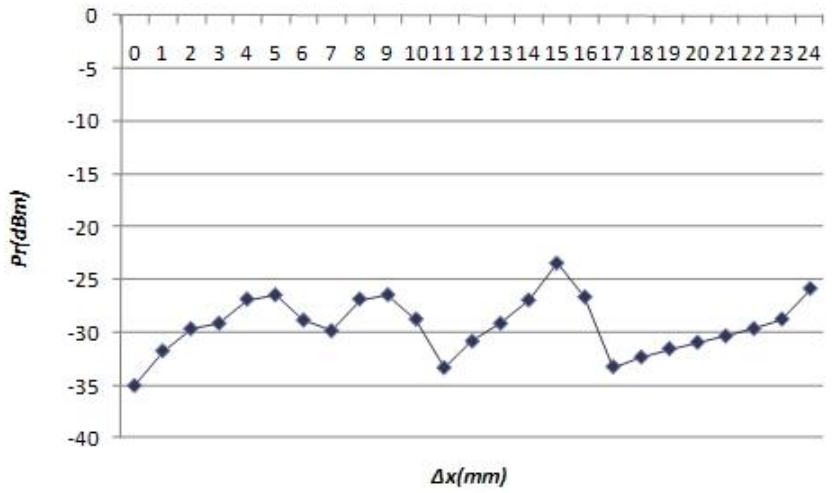

Figure 5.8: Received Power Measured as the Receiver Moved from Left to Right with The Control Algorithm Active.

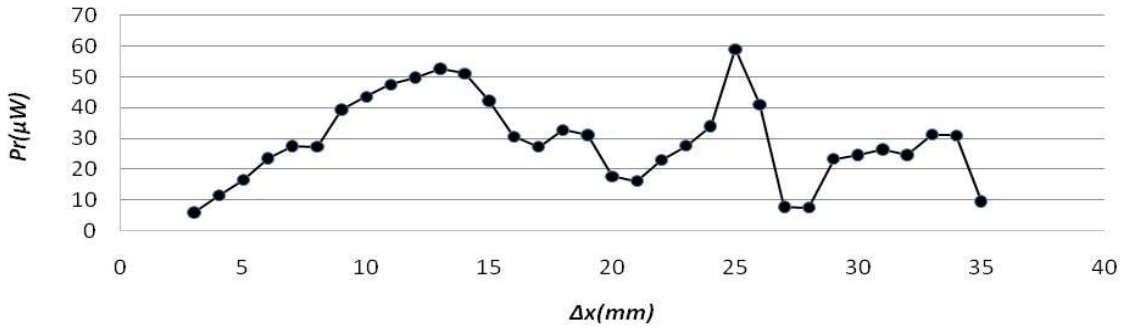

(a)

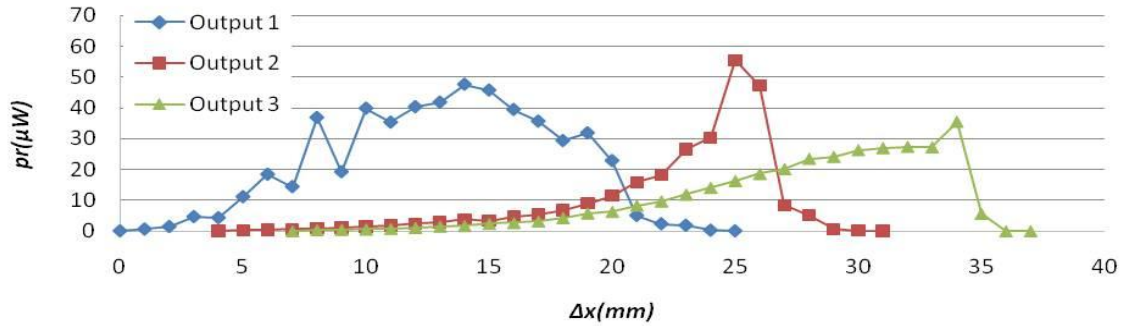

(b)

Figure 5.9: (a) Received Power Measured as the Receiver Moved Left to Right with the Control Algorithm Active. (b) Individual Power Distributions of the Three Transmitting Fibers at the Receiver.

The performance of the control algorithm was critically dependent on the choice of P_{th}. If P_{th} was set too low, the BERT would register a link failure before the transmitter would execute a switch and track the receiver movement. As a result, either a prolonged switching delay would be recorded while the receiver moved through the overlap points between the transmitted beams, or the receiver could be positioned such that the link failed without any corrective action was taken by the transmitter. If P_{th} was

set too high, a situation could occur where the output from none of the transmitter fibers produced a collected power above P_{th}, but there was sufficient power from at least one of the fibers to maintain the link. In this case the control algorithm timed out and indicated that the link had failed. In practice the value of P_{th} may need to be dynamically adjusted for changing operating conditions on the link – weather, turbulence, variations in transmitter power – in order to maintain the desired up time for the link.

The second aspect of the link performance that was studied was the time required to recapture the link once the switching process was initiated. For the motion patterns and velocities used, the switching occurred between adjacent fibers in the transmitter array. The link-recapture time for switching between adjacent transmitter fibers was averaged over at least ten switches and the results are shown in Figure 5.10. Previous investigations determined that the physical switching of the 1x2 switches was at the limit of the measurement capabilities of the BERT, on the order of 1 – 2 ms [10]. Therefore, the times indicated in Figure 5.10 are entirely determined by the operation of the control algorithm. The most significant discrepancy occurred for switching between fibers one and two, with a difference of approximately 240 ms. The discrepancy is easily explained by the choice of search pattern once the collected power fell below P_{th}. Since the search pattern always started with fiber two and ended with fiber one, if the receiver moved from the area covered by fiber two into the area covered by fiber one, then the control algorithm would execute two switches – 2 → 3, and 3 → 1 – before a collected power above P_{th} was found. If the receiver was moving the other direction, the start of the search pattern (fiber two) would coincide with the new position of the receiver, resulting in the execution of only one switch and thus a shorter recapture time for the link. It is

expected that any scanning pattern will result in such discrepancies in switching time unless additional information is available regarding the motion of the receiver. Existing solutions such as a guide beam could potentially provide this information.

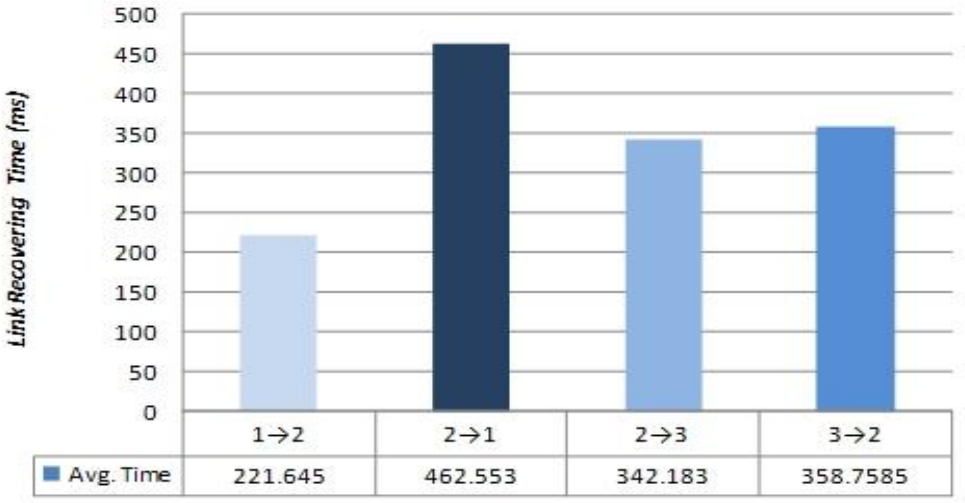

Figure 5.10: Average Link Recapture Times When Switching between Different Pairs of Fibers in Different Directions.

The second test conducted was a series of experiments to examine how the number of averages used to compute the collected power impacted the link-recovery time during receiver movement. Increasing the number of data points averaged together could potentially reduce the number of events where switching occurred due to anomalous readings or temporary changes in value due to interference between overlapping beams or vibration, but also incurs a penalty for increased computational time. For the conditions existing in the laboratory during the experiments, the increased computational time significantly outweighed any potential benefits, as seen in Figure 5.11.

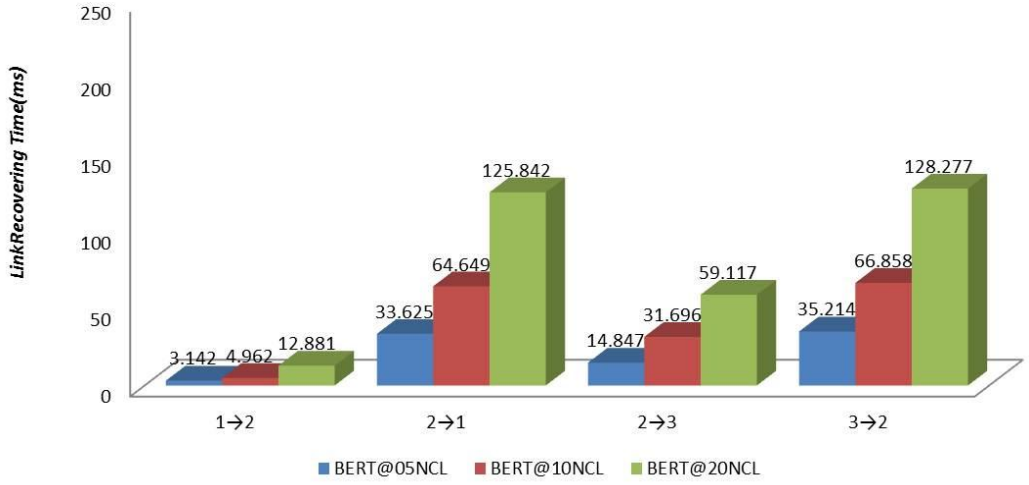

Figure 5.11: Link Recovery Time as a Function of Switching Direction and Number of Averages (NCL in legend). Blue bars are 5 averages, red bars are 10 averages, and green bars are 20 averages.

5.7 Summary of Experimental Evaluation

The basic elements of a previously proposed control algorithm have been implemented and investigated experimentally for a novel optical wireless link utilizing fiber optic bundles at the transmitter and receiver for beam steering and improved misalignment tolerance respectively. The ability of the control algorithm to track the movement of the receiver has been demonstrated, and the effects of design choices on the performance of the control system have been investigated. Further development and evaluation of a more complete system based on these initial successes is described in Chapter 6.

Chapter 6

Evaluation of Fiber-bundle Based Transmitter Configurations with Alignment Control Algorithm for Mobile FSO Nodes

This chapter evaluates a set of transmitter configurations along with the previously proposed alignment control algorithm to facilitate tracking of the receiver and hence maximizing up time of the link. The configurations include switching light between individual fibers in the bundle, splitting of light amongst multiple fibers and switching between groups of fibers, and splitting light between all of the fibers. Each approach is evaluated on key parameters including power at the receiver, switching time, link recovery time, and coverage area at the receiver plane. The study is expected to find the best applicable case for each configuration. The performance of the proposed control algorithm with different approaches for locating the target is also evaluated. Furthermore, the control system's adaptability to wavelength diversity is also examined. The results define guidance to improve the overall system robustness.

6.1 Experimental System

6.1.1 Experimental Setup

The experimental setup constructed for the test is shown in Figure 6.1. Compared to the setup shown in Figure 4.1, the major transmitter, receiver and control components in both setups are basically the same. The guide beam and quadrant detector were added to the test setup to construct an alignment assistant system which provides information about the receiver's misalignment and thus allows the control system to locate the target

faster. The quadrant detector provides x-axis and y-axis alignment difference signals (x_{diff} and y_{diff}) from the guide beam. The guide beam was produced by a red laser diode and received by a fisheye lens placed directly in front of the detector. Since the receiver motion in the tests only occurs along the x axis, we only use x_{diff} here. The guide beam system is calibrated to match the receiver's position. When x_{diff} is equal to zero, it means the receiver is on the optical axis without misalignment; when x_{diff} is positive, the receiver is misaligned to the right of the optical axis; and when x_{diff} is negative, the target is misaligned to the left. The receiver moving towards the left increases x_{diff} with time and moving towards the right decreases x_{diff} with time.

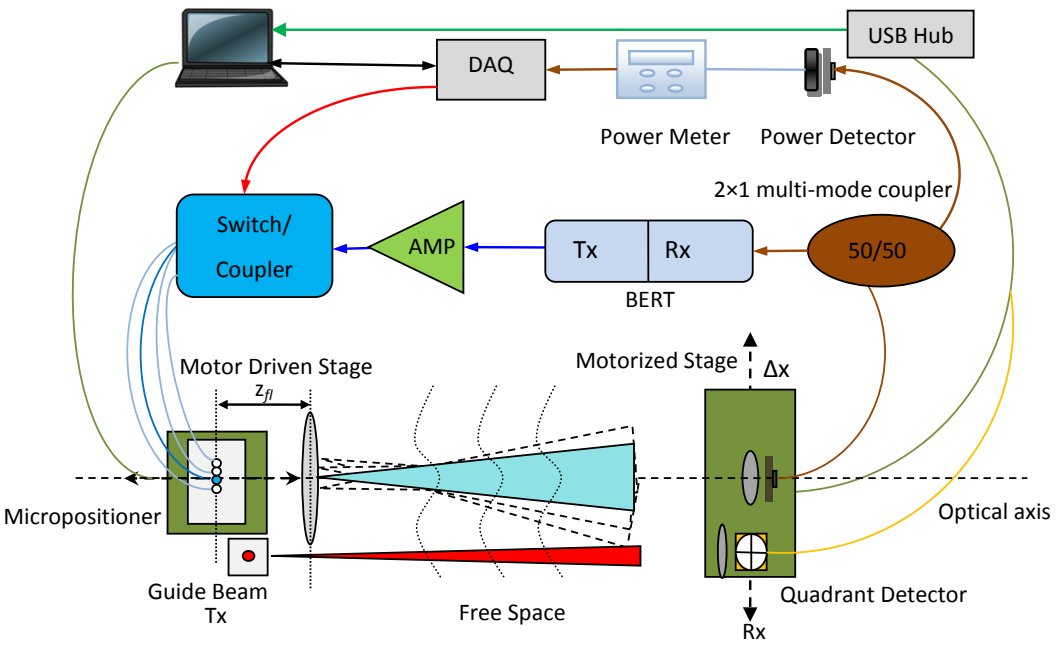

Figure 6.1: Experimental Setup showing Alignment Assistant System.

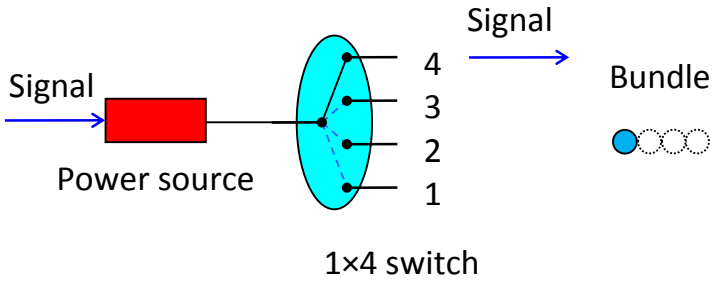

(a)

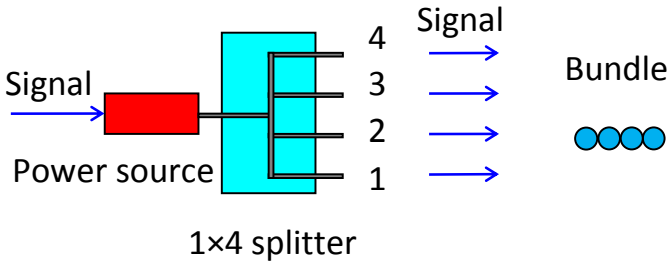

(b)

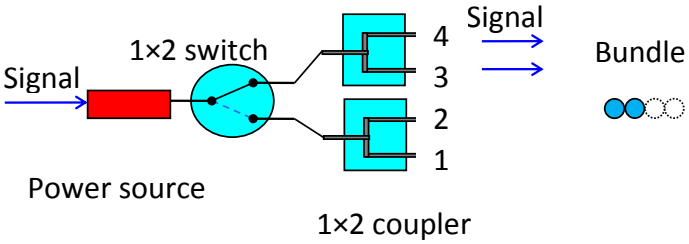

(c)

Figure 6.2: Transmitter Configurations Investigated in Lab: (a) All-Switch design (b) All-Coupler design (c) Hybrid design

The BERT here still functioned as the optical signal source, sink, and analyzer. Four single-mode transmitter fibers are cemented together in a linear ribbon cable. Each fiber in the transmitter was connected to one output of the configurations under test. The concepts of All-Switch design, All-Coupler design and Hybrid design have been

introduced in Chapter 5. Figure 6.2 shows the laboratory versions of these three transmitter configurations. Under this test, "All Switch" design uses one 1×4 switch to concentrates the optical power to only one output; "All Coupler" design uses one 1×4 coupler to distributes optical power simultaneously to all of the fiber outputs; " Coupler/Switch Hybrid" design contains one 1×2 switch and two 1×2 couplers to reach a compromise between the other two types of designs. The switches used in the experiment were MEMS-based switches having a switching time of 1.229 ms to 2.458 ms and an insertion loss of approximately 8.5 dB. The receiver was assembled on a motorized stage instead of a manual stage to enhance test accuracy. The distance between input lens of the receiver and the output lens of the transmitter was 2.1 meters. The link data rate was set as OC-1.

6.1.2 Alignment Control Algorithm

The control algorithm follows the phases: power monitoring, decision making and link recapturing to maintain the optical link. Each algorithm phase's experimental function was described in Section 5.5. In addition, the received power was sampled by the DAQ at rate of 48 kHz as a voltage reading. All the tests were investigated with averaging loops of five samples in length. The amount of information about the receiver movement that is available to the control algorithm results in different operating scenarios, each of which was evaluated.

In the first scenario, no information regarding the receiver's direction of movement is available. In this scenario, the transmitter uses a preset procedure for conducting the search, illuminating each fiber or set of fibers in a particular sequence.

For example, with the all-switch design shown in Figure 6.2(a), the transmitting fibers are illuminated in a fixed pattern, with the fibers illuminated in order from 1 to 4, always starting at the currently illuminated fiber. So, if fiber 2 is transmitting and the algorithm detects a loss of power, the sequence dictates that the next fiber illuminated is fiber 3. Fiber 4 would then be illuminated if the signal is still not recovered, and so on. As each fiber is illuminated, the power sampling and averaging process described previously is repeated and the power is compared to P_{th}. The attempt to recapture the link continues until either one of the transmitter fibers can re-establish the link or a set time for recapturing the link expires, at which point the control system determines that the link has failed.

In the second scenario, the guide laser and quadrant detector provide sufficient information to determine the receiver's direction of movement. For the case in Figure 6.2(a), if the signal is lost at fiber number two and x_{diff} was decreasing with time, thus indicating that receiver was moving left, then the control algorithm could decide to start the search by illuminating fiber number one first, instead of illuminating number three as it does in the first scenario, to minimize the recapturing time.

This concept is depicted graphically in Figure 6.3. If the receiver moved to the right, the input to the algorithm from the quadrant detector would become more positive. If the transmitter is configured correctly, the coverage areas for transmitting fibers one and two would overlap between point *D* and point *C* in Figure 6.3. So, as the signal from fiber two fades, the transmitter will know to switch to fiber one based on the quadrant detector's signal and the link recapture should only be a function of the time required to switch between fibers.

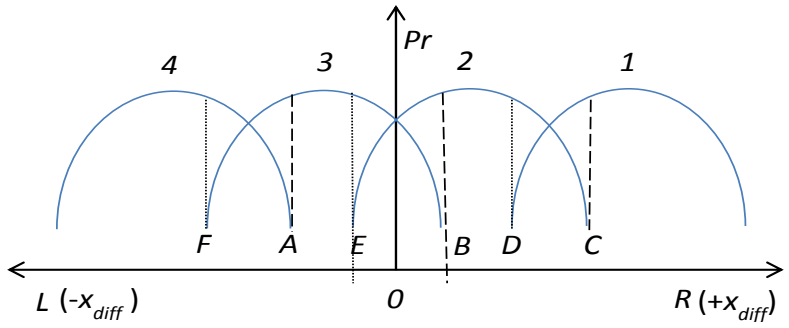

Figure 6.3: Decision making according to guide beam for all-switch design during test. The four curved lines represent the power distribution from each output of the switch.

Ideally, the detection range of the guide beam system is large enough to cover the whole receiver movement area, and should be able to provide a value of x_{diff} changing linearly with position. Experimentally, due to the restriction of the fisheye lens's aperture and other difficulties, the change of x_{diff} with the receiver's position is only linear in a very limited range before reaching its saturation point. To address this problem, a compromise solution was adopted. For the 1×4 switch configuration under test, by only knowing the sign of x_{diff}, the algorithm could decide which direction to switch towards when the signal is lost. For instance, once the power from fiber two fades, if x_{diff} is positive, the signal will be switched to fiber three; if x_{diff} is negative, then the algorithm will light up fiber one. In the experiment, the zero point of x_{diff} was calibrated between the overlapping points B and E in Figure 6.3 to allow the motion detection to be implemented.

6.2 Results

Initial system alignment, power meter calibration and determination of threshold power P_{th} for the BERT for the given alignment were executed before starting each experiment. The total transmission power was set as 3 mW.

For the power distribution tests, the receiver's plate moved 1 mm per step using a motorized stage, and the speed of movement was very similar for each test. For the link recapture time tests, the movement of the receiver's plate was set at a constant speed of 2 mm/s. The stage was swept 10 times between the extremes of the transmitter's coverage range, with sweeps occurring continuously over the duration of the test. The link recapture time for switching between transmitter fibers was averaged over all sweeps to obtain the final results. After the valid transmitter's coverage range at the receiving end was recorded, the receiver was scanned from one end of the coverage's range to the other end for each test, and the control algorithm determined which of the transmitting fibers to be illuminated during the receiver's movement. Both the BERT and the algorithm were used to measure the time required to recapture the link. The BERT measured the link restoration time as the time when the link becomes error-free again, while the algorithm measured the link recovery time by the time when the received power rose above P_{th}.

6.2.1 Transmitter Configurations Evaluation

The first experiments that were conducted investigated the relative capabilities of the three transmitter configurations. For all of these experiments, four fibers were available for use at the transmitter, and the same alignment control algorithm was used.

The algorithm monitored the received power and began a preset search pattern to recapture the link when the received power fell below threshold. The search pattern simply selected the output fibers in order from one through four. No attempt was made to use information from the quadrant detector to optimize the search pattern.

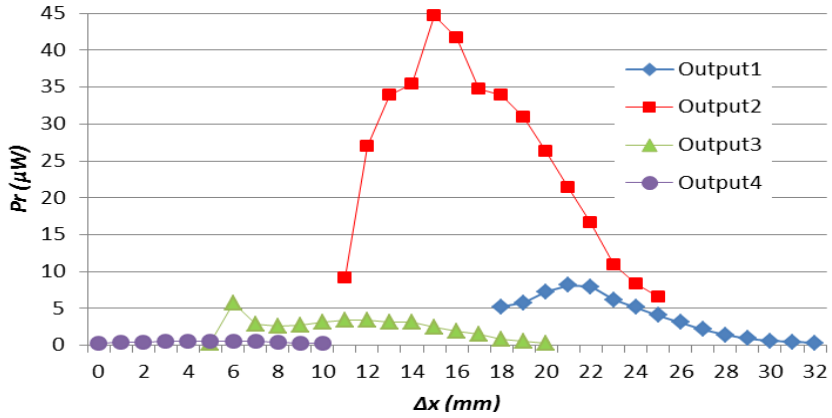

(a)

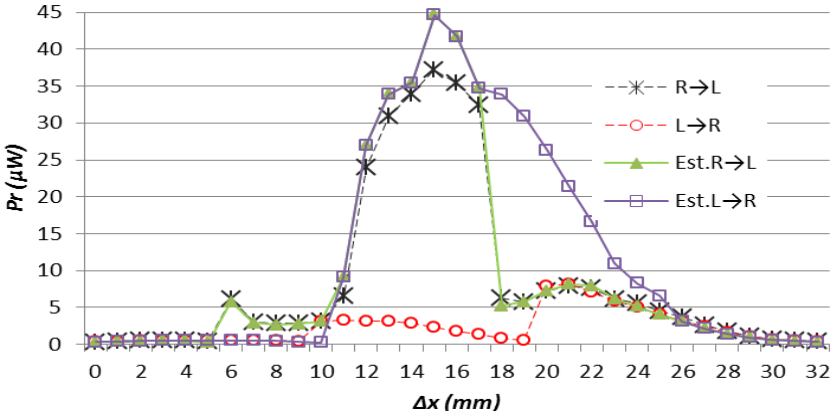

(b)

Figure 6.4: (a) Received power distributions for the four individual transmitting fibers (b) Received power measured and estimated response as the receiver moved with the control algorithm active for all-switch design.

6.2.1.1 All Switch Design

Since the all-switch design illuminates only one of the transmitting fibers at any one time, it was necessary to first measure the receiver response to each individual transmitting fiber in order to evaluate and understand the characteristics of this design. As each transmitting fiber was illuminated, the receiver was scanned along the horizontal direction and the collected power was monitored. The results are shown in Figure 6.4(a). Output two is the transmitting fiber centered on the axis of the transmitting lens, resulting in a transmitted beam propagating parallel to the optical axis. As a result, the receiver collects light from output two very well. The other transmitting fibers are located away from the optical axis of the lens, and thus the optical power travels at an angle with the optical axis. As the field of view of a single-lens receiver is rather narrow, less optical power is coupled into the receiving fiber, resulting in a weaker response. Note that the collected power curves for individual outputs overlap, so that continuous coverage is possible over much of the 32 mm range.

Experiments were conducted with the receiver moving from left to right and from right to left, and the results are presented in Figure 6.4(b), along with estimates of the response for both cases based on the data in Figure 6.4(a). For the BERT, error-free operation was maintained for received powers near -35 dBm, or 0.32 μW, after which the BER degraded rapidly, so this number was used for P_{th} in the control algorithm. For left-to-right movement (moving from 0 to 32 mm), the receiver first detected the signal from output four. In estimate, when the power collected from output four dropped below P_{th} at 10 mm, both output two and three were providing signal above P_{th}. Since the simple search pattern used in this experiment always followed the order 1 → 2 → 3 → 4 in

sequence, starting with the currently lit fiber, the algorithm was expected to select output two to recapture the link. While in the test, the power collected from output four faded at 9 mm in advance, at which point only output three was providing signal above P_{th}, and this output was selected by the algorithm. When the power from output three falls below threshold around 19 mm, the control system chose output one instead of output two, even though the power collected from output two would be larger and provide a better operating margin, because of the chosen search pattern. For the same reason, when the receiver is traveling from right to left (from 32 mm to 0 mm), the switching around 18 mm favors output two over output three. The estimated response is in good agreement for right-to-left movement, but not for left-to-right due to experimental variability. This was the only case where the estimate did not accurately predict the measured results.

6.2.1.2 All Coupler Design

For the all-coupler design case, the power collected by the receiver is shown in Figure 6.5, the open circles indicate invalid and zero values. The power collected is lower at most positions than the power collected by the receiver for the all-switch design. This results from a combination of the lower antenna gains for the outer transmitting fibers and the lower power available in all of the fibers, even the center fiber.

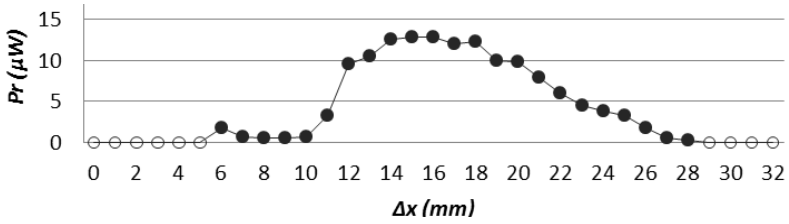

Figure 6.5: Power Distributions at the Receiver for All Transmitting Fibers for the All-Coupler Design

Comparing the all-coupler design and the all-switch design, there are some clear trade-offs with respect to the operation of the link. The all-switch design is able to recapture the link over a wider range of misalignment, essentially over the entire 32 mm range, than the all-coupler design, which captures measurable signals over a more limited 22 mm range (from 6 to 28mm). This issue would be magnified if transmitting fibers covering the vertical directions were also employed, further dividing up the available transmitter power or requiring a higher initial transmitter power to maintain an acceptable coverage area at the receiver. The all-coupler design, though, does not incur any temporary link outage due to switching. Few additional control software or hardware components are needed, saving both power and space in an environment (such as a UAV) where both are in limited supply.

6.2.1.3 Hybrid Design

The hybrid design is depicted in Figure 6.2(c). As in the other designs, the power collected by the receiver was measured for each output case. The results are shown in Figure 6.6(a). As expected, the collected power is less than that achieved with the all-switch design but larger than that with the all-coupler design. As in the all-switch case, there is a region where the two output choices overlap in their coverage at the receiver, and the control algorithm will need to initiate switching between the outputs when the collected power falls below P_{th}.

The results of the experiments conducted on this design are shown in Figure 6.6(b), along with estimates of the response based on the data in Figure 6.6(a). As before, the power collected at any given position depends upon the control algorithm and the

direction of movement. The estimated response is in good agreement, with only slight differences due to experimental variability. Compared to the all-switch case, the hybrid design has a slightly smaller coverage range – 26 mm instead of 32 mm – but only interrupts the transmission with one switch instead of the two or three switches for the all-switch case.

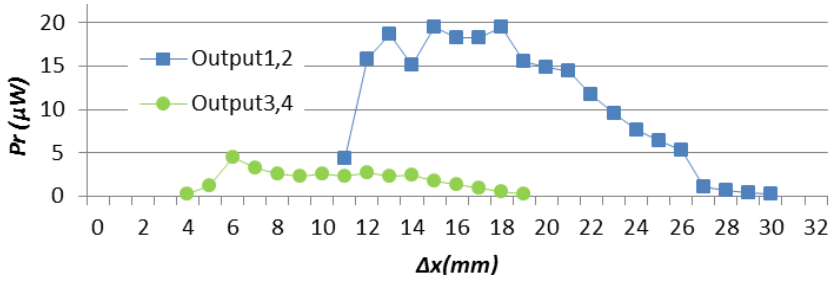

(a)

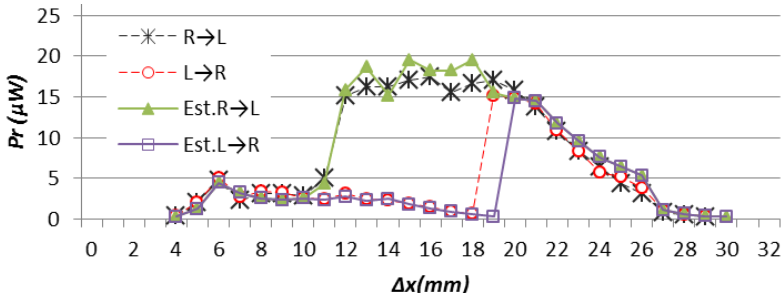

(b)

Figure 6.6: (a) Power distributions at the receiver for transmitting fibers combined by the 1-by-2 couplers (b) Received power measured and estimated response as the receiver moved with the control algorithm active for hybrid design.

6.2.1.4 Link Recapturing Time

For the all-switch and hybrid cases, a key consideration is the time required to recapture the link. The recapture time encompasses three components: the time required

to detect a link failure, the time required to execute switching to the new output fiber(s), and the time required for the receiving electronics to resynchronize with the recaptured optical signal.

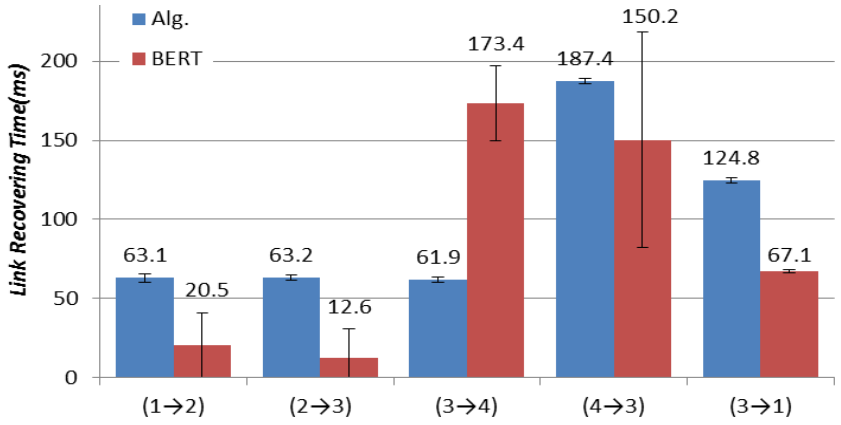

(a)

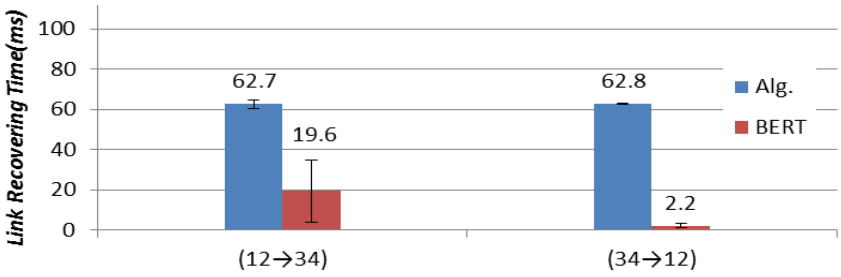

(b)

Figure 6.7: Link Recapturing Time with Error Bars (±standard deviation) for (a) All-switch design (b) Hybrid design.

Figure 6.7 presents measurements of the link recovery time measured by the BERT and the control algorithm. Figure 6.7(a) presents the measurements for all of the switching cases that occurred during the experiments described in Figure 6.4. For most of the cases, the BERT detects that the link is restored in less time than the algorithm requires. This is in part due to the averaging cycle used in the algorithm, and in part due

to the operating delays in LabView, which must execute the switch and then resume the functional block that performs the power detection. The switch from outputs 1 to 2, 2 to 3 and 3 to 4 are short because the algorithm executed only one switch for each case. The switch from outputs 3 to 4 measured by the BERT is much longer than the one counted by the algorithm. It indicates that signal errors occurred during this single switch, which resulted in a longer time for error-free link restoration, even though the power recovery required about the same time as the other switches. Switching from outputs 4 to 3 takes by far the longest time to execute, because the algorithm implemented three switches – 4 to 1, 1 to 2, and 2 to 3 – before a collected power above P_{th} is found. The link recovery time in this multi-switch is approximately triple the time required by each single-switch case. The switch from 3 to 1 takes longer because two switches are executed: 3 to 4 and 4 to 1, and the recovery time is nearly twice the single-switch time.

Figure 6.7(b) shows the recapture times measured for the hybrid case. Both switching times are short, as they are one switch operations, and the BERT again outperforms the algorithm for the reasons noted previously. For the BERT, the (12→34) switching case took much longer to restore the link quality due to the attendant errors than the reverse case did.

6.2.2 Behavior in Theory

The trade-offs found in the experiment are also discovered in the theoretical treatment for the three configurations. Figure 6.8 shows a comparison of power distributions calculated from the simulation model in Chapter 3 by limiting which transmitting fibers contained optical power.

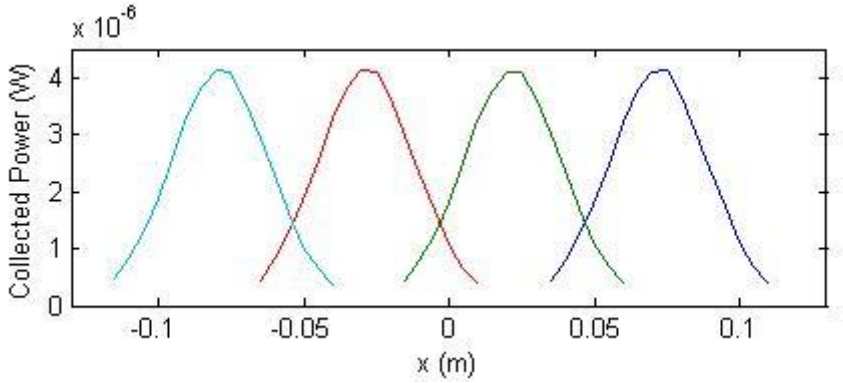

(a)

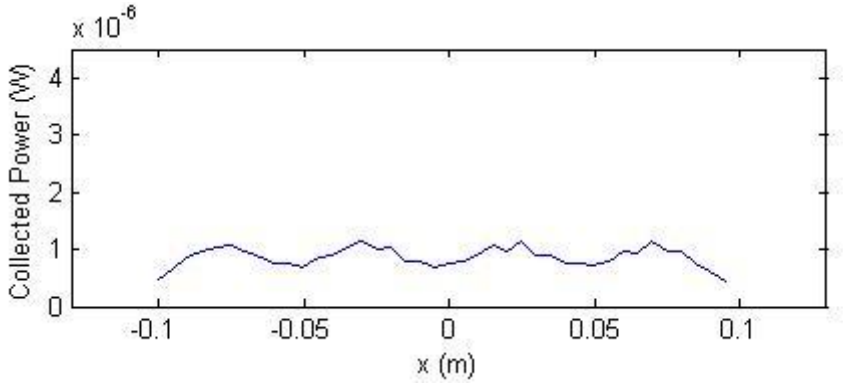

(b)

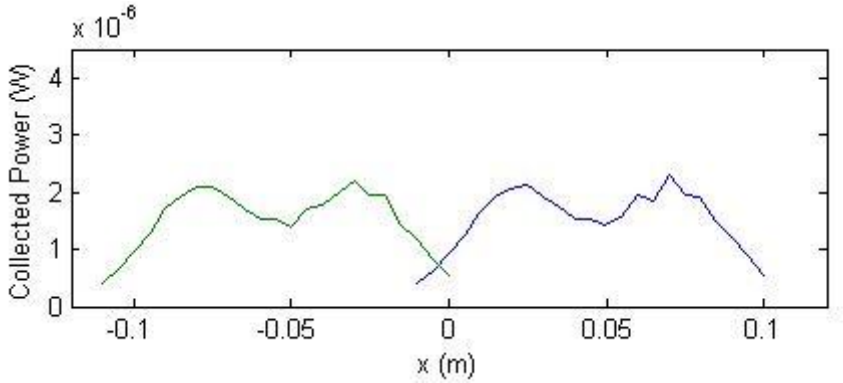

(c)

Figure 6.8: Calculated Power Collected by the Receiver at 1310 nm, total Pt = 4 mW, z_L= 20m, z_{fl} = 48.75mm, P_{th}= -35dBm (a) for the four individual transmitting fibers in the all-switch design (b) for all transmitting fibers in the all-coupler design (c) for transmitting fibers combined by the 1-by-2 couplers in hybrid design

The highest peak power was achieved by the all switch design in Figure 6.8 (a), and the overlapping of four individual outputs could create the widest continuous coverage for the receiver with temporary link suspension due to switching; For the all coupler design in Figure 6.8 (b), the loss of power due to power splitting would make valid beam coverage least desirable, even with the counter-active effect of power summing due to the overlap; For the hybrid design in Figure 6.8 (c), both the collected power and the valid coverage are less than the ones achieved with the all-switch design but larger than those with the all-coupler design. None of the transmitter configurations can complete a link where the collected power is below threshold, but increasing the collected power (by increasing the transmitter power or the power collecting capacity of the receiver) would permit the use of lower-divergence transmitted beams to obtain continuous coverage range, and would provide larger peak powers. The hybrid design would best take advantage of this situation, especially if the transmitter could switch from, in Figure 6.8(c), the left-center pair to the right-center pair.

6.2.3 Algorithm Evaluation

A second set of experiments was conducted to evaluate the algorithm's performance for scenarios where different amounts of information about the receiver's movement were available. For these experiments, the transmitter was constructed with an all-switch design. A realignment of the system was required due to a physical disruption of the receiver setup, so a new sampling of the power collected by the receiver was taken and presented in Figure 6.9(a). The remainder of Figure 6.9 shows the performance for the two scenarios under consideration in this work. Figure 6.10 shows the associated switching times.

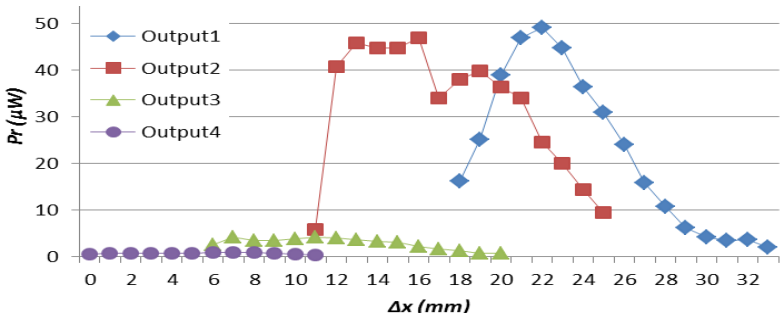

(a)

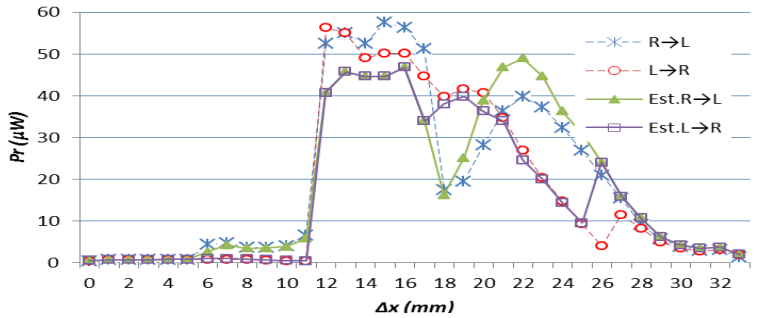

(b)

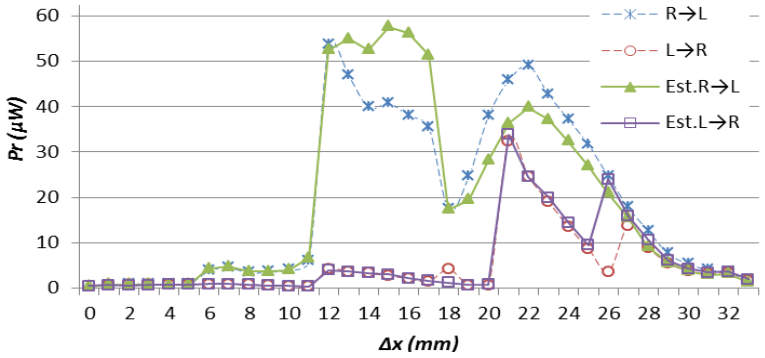

(c)

Figure 6.9: (a) Individual power distributions at the receiver for all-switch design. Received power measured and estimated response with the control algorithm active for (b) fixed scanning pattern. (c) motion detection by quadrant detector.

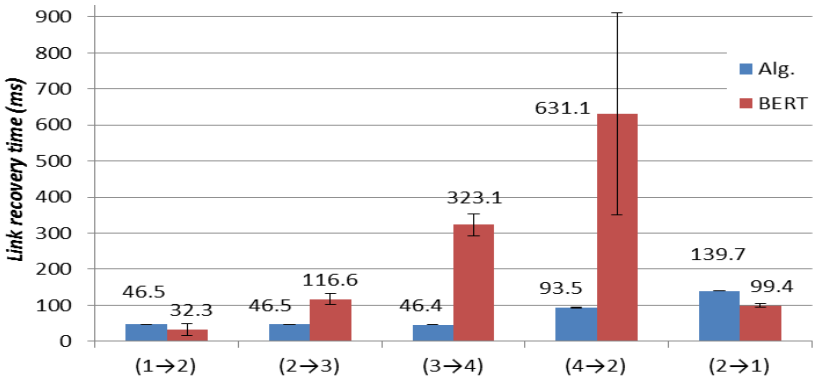

(a)

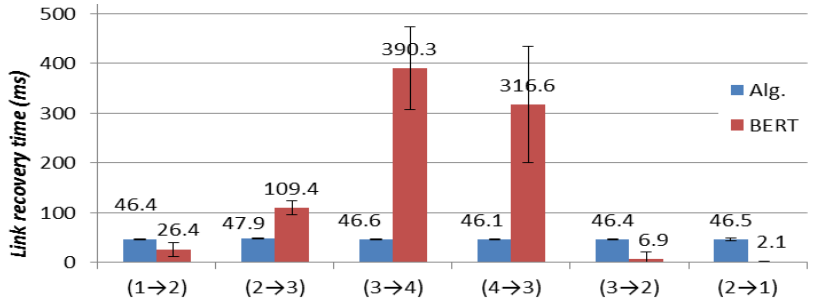

(b)

Figure 6.10: Link Recapturing Time with Error Bars (± standard deviation) for (a) fixed scanning pattern. (b) motion detection by quadrant detector.

Figures 5.9(b) and 5.10(a) show the behavior of the algorithm for the same scenario used in Figures 5.4(b) and 7(a). The behavior observed was consistent with the previous results.

Figures 5.9(c) and 5.10(b) show the behavior of the algorithm where switching was guided by motion detection information from the quadrant detector. By determining whether the output of the quadrant detector is positive or negative, the algorithm made a best determination of which direction the receiver is moving, and then chose the first fiber in its search accordingly. The expectation was that the recapture time would

decrease with respect to the fixed pattern scenario in the majority of the switching cases. When comparing Figures 5.10(a) and 5.10(b), this decrease is indeed observed when the receiver was moving left to right, as the algorithm no longer needs to execute multiple switches, but instead switches to adjacent output fibers. The error-free link restoration time measured by the BERT was improved by at least 50% compared to the unguided algorithm. Thus a benefit is observed, even in these simple experiments.

It is also worth noting that the power collected as a function of the receiver position is quite different for the two different implementations of the algorithm. Comparing Figures 5.9 (b) and 5.9 (c), switching from output four to output three for the guided algorithm, instead of output two for the unguided algorithm, when moving left to right results in a lower average collected power over the movement range. While this may be in part attributed to the specifics of the system under study, it is realistic to expect that similar results may occur in general systems, especially near the outer limits of the coverage range.

6.2.4 Multi-wavelength Operation

The test in the scenario used for Figures 5.9(c) and 5.10(b) was repeated for the two different wavelengths with different choices of beam divergence. For this experiment, the test setup was slightly modified, which is shown in Figure 6.11. Since the BERT in lab only operates at 1310nm, a laser supply operating at either 1310 nm or 1550 nm wavelength was used as the signal source instead. The number of transmitter fiber outputs in use was reduced from four to three to enhance the overall test efficiency. A power meter was connected to one output of the 1×4 switch to monitor the transmission

power for calibration when switching wavelength operation. The receiver fiber was directly coupled to the detector as a reading input of the control system. . For all of the wavelengths used here, the receiver was assumed to have a threshold for error-free operation of -31.4 dBm, which is the threshold value obtained for the BERT, operating at 1310 nm and data rate of OC-48, used in the laboratory.

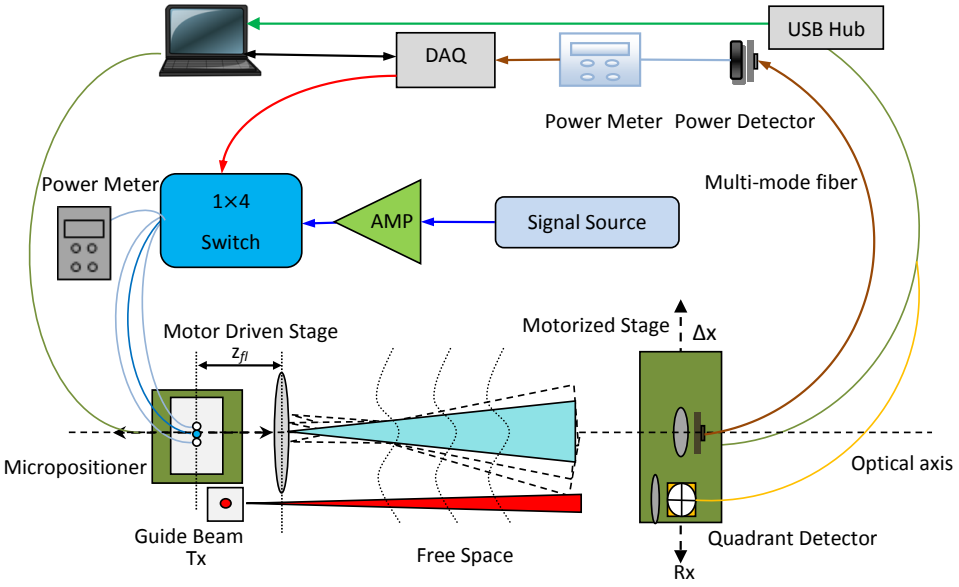

Figure 6.11: Experimental Setup for Multi-wavelength Operation

The experiment was initially conducted at the 1310 nm wavelength for four different beam divergences. The beam divergence was set by the distance z_{fl} between the output of the fiber array and the transmitting lens. The power collected from each of the transmitting fibers as a function of the receiver's position was then measured, and the results are shown in Figure 6.12. As can be seen in the graphs, the divergence of the beam is decreasing with increasing values of z_{fl}, resulting in a narrower range over which measurable power can be collected by the receiver's optical system. The distribution

measured at z_{fl} = 78 mm for output 1 was cut off due to the limited resolution along the *x* direction used in the experiment, and it is common in the graphs for the curve to be asymmetrical with *x*, which is an artifact of the alignment of the receiver optics. For control-related operations, it is important to note that overlapping of the curves decreases as the beam divergence increases. The lack of overlapping causes there to be only one correct decision for the control algorithm, but also leads to potential dead zones or switching drops when small perturbations in the overall link produce areas where there is no choice of output fiber that re-establishes the link.

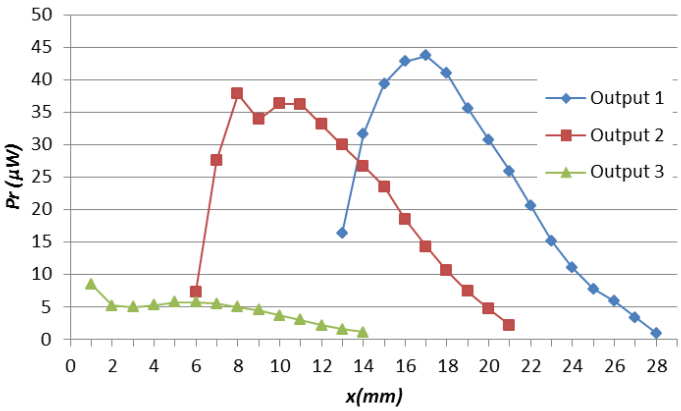

(a)

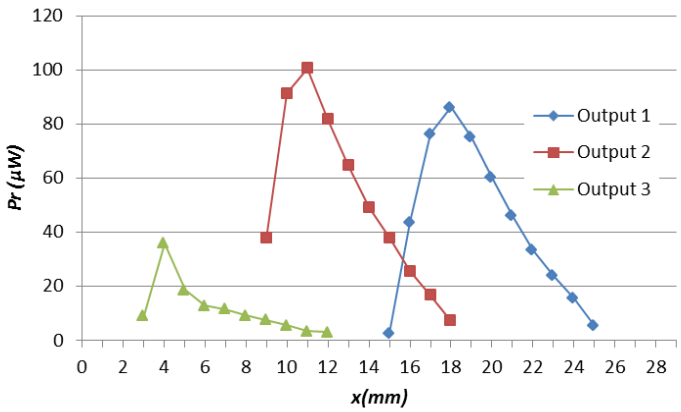

(b)

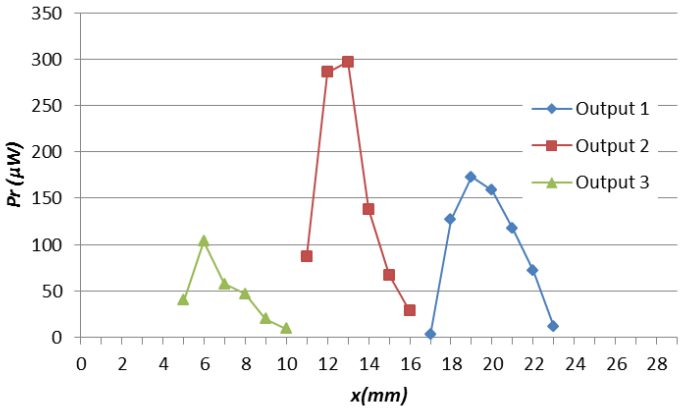

(c)

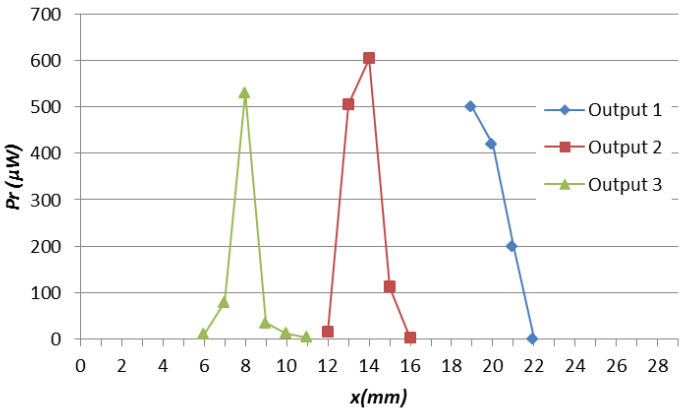

(d)

Figure 6.12: Received Power Distributions for the Three Individual Transmitting Fibers at 1310nm Wavelength with z_{fl} Value of (a) 75mm (b) 76mm (c) 77mm (d) 78mm

Figure 6.13 shows the resulting actions of the control system for the first three cases shown in Figure 6.12. The 78 mm case is not shown as its results are the same as for the 77 mm case, except that there were some points where the control algorithm failed to find a "correct" fiber to select because insufficient power was available at the receiver to complete the link. In this situation, the control system timed out and produced a link failure condition until the receiver moved back within the coverage range of one of the

transmitting fibers. The data was taken for movement of the receiver from left to right through the transmitting beams and from right to left. There exist very distinct differences in the collected power as a function of position for the two directions, and this is entirely a result of the way the control algorithm was conceived and implemented. In moving left to right, the control algorithm encountered the wide tails of the right side of the collected power distributions, and so did not make a decision to switch even though selecting another fiber would produce greater power. To perform such a switch would require the control algorithm to have a prior knowledge of the distributions, which was not assumed here. This choice reflects the assumption that in practical systems the transmitter may be moving as well as the receiver, and so it is dangerous to assume where the peak power may be. For the right to left case, the left side of the individual curves is much sharper and less overlap exists, so the transition to the next transmitting fiber occurred, in general, at a higher collected power. If overlap is known to exist, or if the system is designed properly such that overlap is always expected, then the left-to-right and right-to-left performance of the algorithm may be made to better coincide if a slightly higher threshold power was used for initiating a switch. Although, for the current implementation, the link is maintained for the entire range for both movement directions, having a higher average power in both directions would reduce the maximum BER expected. Figure 6.13(c) shows that both directions produce the same result if the beams just barely overlap, which provides more predictable performance but requires that the small areas of overlap are not erased by atmospheric turbulence and weather effects.

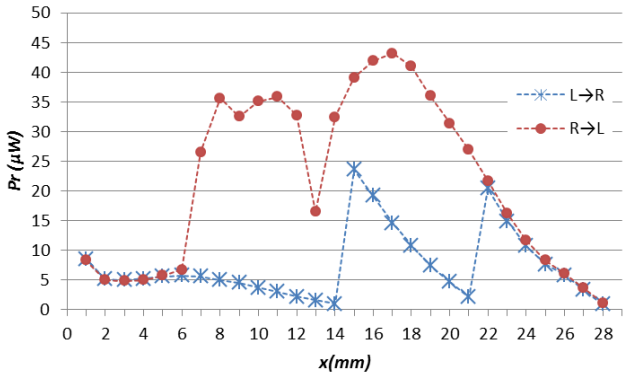

(a)

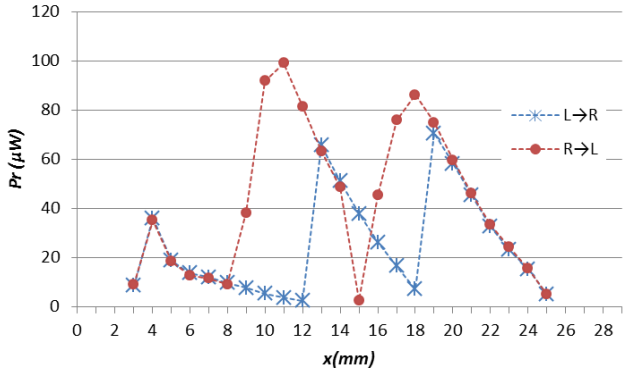

(b)

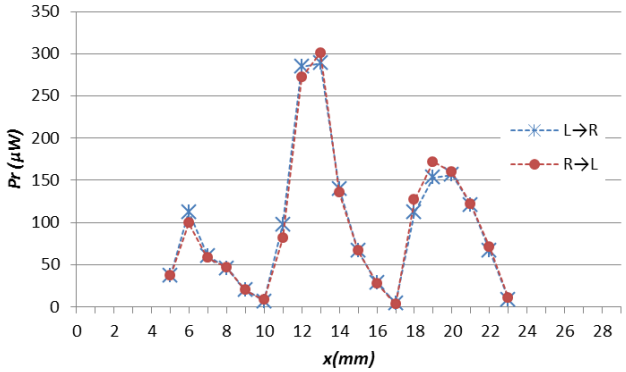

(c)

Figure 6.13: Received Power Measured as the Receiver Moved with the Control Algorithm Active at 1310nm Wavelength with z_{fl} Value of (a) 75mm (b) 76mm (c) 77mm

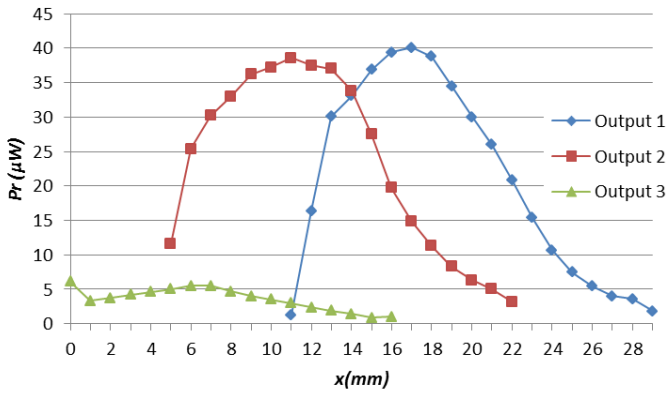
45
40
35
30
25
20
15
10
5
0
Pr (μW)
0 2 4 6 8 10 12 14 16 18 20 22 24 26 28
x(mm)
Output 1
Output 2
Output 3

(a)

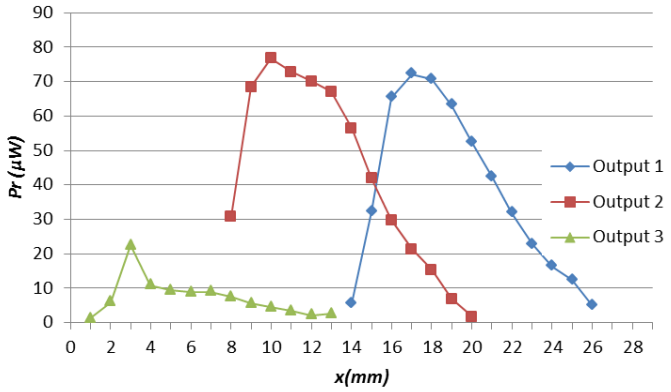
90
80
70
60
50
40
30
20
10
0
Pr (μW)
0 2 4 6 8 10 12 14 16 18 20 22 24 26 28
x(mm)
Output 1
Output 2
Output 3

(b)

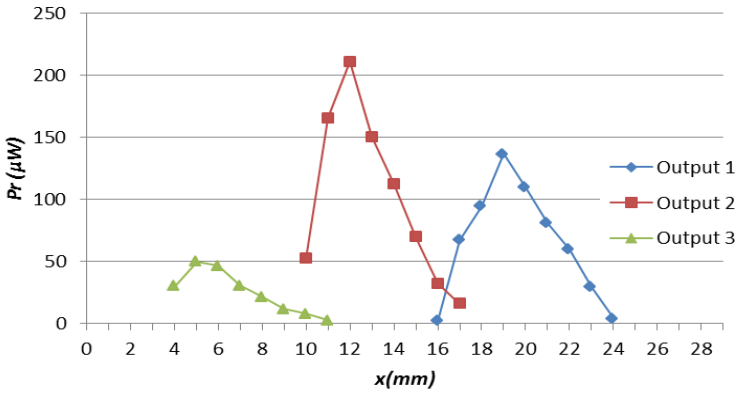
250
200
150
100
50
0
Pr (μW)
0 2 4 6 8 10 12 14 16 18 20 22 24 26 28
x(mm)
Output 1
Output 2
Output 3

(c)

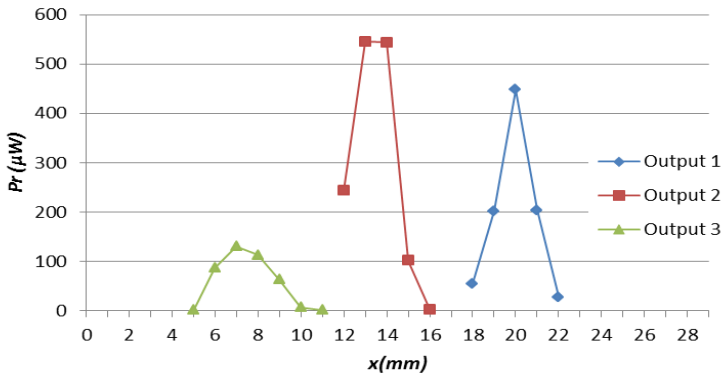

(d)

Figure 6.14: Received Power Distributions for the Three Individual Transmitting Fibers at 1550nm Wavelength with z_{fl} Value of (a) 75mm (b) 76mm (c) 77mm (d) 78mm

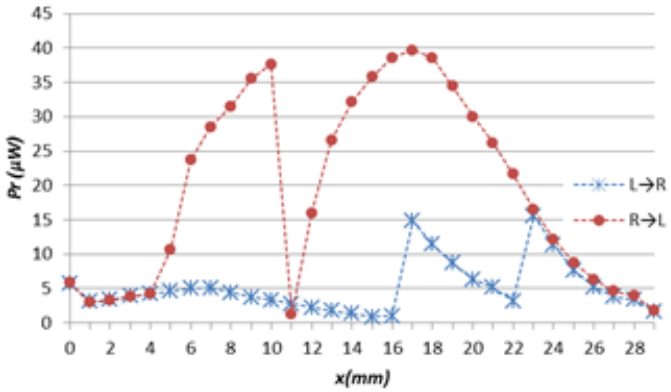

(a)

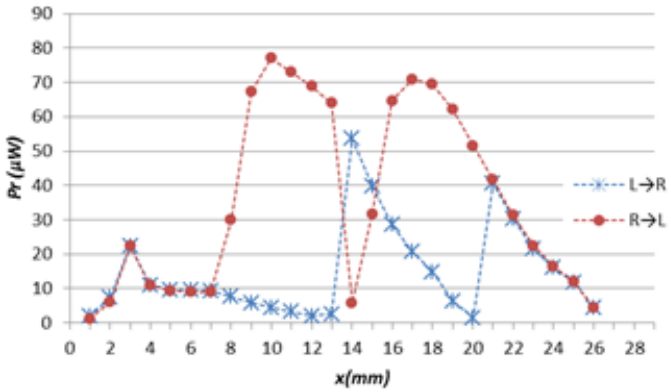

(b)

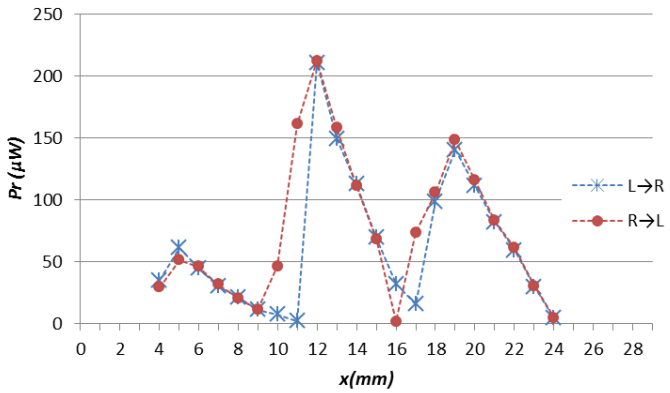

(c)

Figure 6.15: Received Power Measured as the Receiver Moved with the Control Algorithm Active at 1510nm Wavelength with z_{fl} Value of (a) 75mm (b) 76mm (c) 77mm

The measurements of Figures 5.12 and 5.13 are repeated for a 1550 nm source and presented in Figures 5.14 and 5.15. A higher available transmitter power and broader divergence resulted in a larger overlap between the coverage curves of the three transmitting fibers, which can be observed by comparing Figures 5.12 and 5.14 for 1310 nm and 1550 nm respectively. When comparing Figures 5.13 and 5.15, the effects of this increased overlap can be readily observed, especially for the right-to-left case. For this case at 1550 nm, there are now several large dips in the collected power, corresponding to the edge of the overlap region on the left side and then a sudden jump to the middle of the large tail on the right side of the individual responses. Although the link is not lost during these dips, the quality of the signal might indeed suffer if the BER increases with the increase in signal-to-noise ratio at the receiver that would accompany these dips. It must be noted that the dip's effect could be accentuated when the velocity of the receiver is high enough that the receiver moves beyond the edge of the current transmitting fiber's

response before the control system can act on the current information. The link could be temporarily lost (in addition to the switching-induced loss) if the next control cycle does not start before the power collected by the receiver falls before threshold. Based on these results alone, the ability of the receiver to capture different wavelengths equally well means that the impact of wavelength change is felt mostly due to changes in the parameters of the transmitted beam and thus due to the performance of the transmitter, not the control system or the receiver.

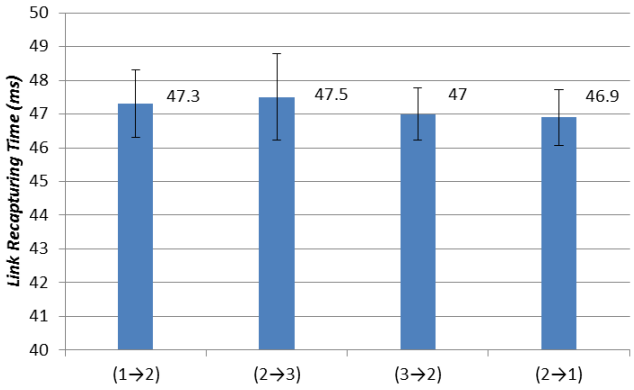

(a)

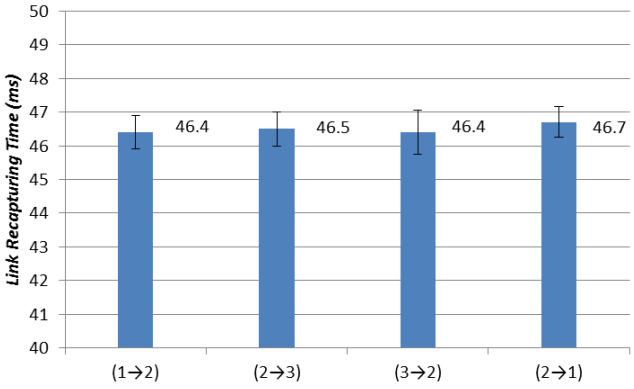

(b)

Figure 6.16: Link Recapturing Time with Error Bars (± standard deviation) for z_{fl} = 75mm at Wavelength of (a) 1310nm (b) 1550nm

The differences in the transmitted beam properties that were observed in the Figures 5.12 and 5.14 are reflected in the link recovery times shown in Figure 6.16. When the switching process was initiated, the power available from the transmitting fiber to which the system was switching was almost always higher for the 1550 nm case than for the 1310 nm case (even for other divergence cases) when moving from right to left. For the 1 → 2 and 2 → 3 cases shown in Figure 6.16, the 1550 nm link responded approximately 1 ms faster, on average, than the 1310 nm link, and the variation in the link recovery times was lower for the 1550 nm case (±0.5 mm standard deviation at 1550 nm, over ±1 mm for 1310 nm). For the left-to-right case, the difference is somewhat less pronounced for both the average and standard deviation of the recapturing time, although the 1550 nm system still has a slight edge.

6.3 Summary

Among the different transmitter configurations investigated, each presented advantages and disadvantages that must be considered when designing a transmitter for a given application. The hybrid design, which combines optical switches and splitters, provides the best compromise between power collected by the receiver and link down time due to switching. The performance of the hybrid design is not expected to degrade significantly as the number of output fibers at the transmitter expands in both the horizontal and vertical directions. The all coupler design would not scale well due to the corresponding decrease in power at each output, and the all-switch design may not scale well depending on the design of the switching fabric and the search algorithm employed. The recovery time for the link can be reduced by supplying the optical tracking system

with some form of target location information, whether from a quadrant detector, accelerometers or GPS data, which would be of great benefit to improving the performance of both designs. The dependence of control system performance on the fiber-lens distance at transmitter was examined, the results show that the alignment control system successfully recovered and maintained the link at each selected wavelength while the receiver was in motion.

Chapter 7

Conclusions

This study investigates the effectiveness of using fiber optic bundles and lens arrays to improve the misalignment tolerance of an FSO receiver and a fiber optic bundle to realize enhanced coverage area and non-mechanical switching at an FSO transmitter.

Both experimental and simulation-based evaluations of the proposed transceiver system demonstrated that the connection between the transmitter and receiver could be maintained over a large coverage area given the proper choice of key parameters, such as beam divergence, the number of transmitting fibers, the switching scheme at the transmitter, and receiver construction, which would strongly support a mobile operating environment. The investigation finds that the coverage area of the receiver can be optimized for a given wavelength by proper choices of these parameters, and that parameter choices exist that minimize the change in performance when switching between wavelengths or for variations in link parameters. The interrelationships between key parameters and their impact on the potential system performance are investigated as well to provide guidance on the further development of the overall system.

In order to take best advantage of the new functionalities and capabilities of this fiber-bundle-based transceiver system, a general algorithm for controlling the transmitter was proposed in order to perform pointing, acquisition and tracking functions. The efficacy of the control algorithm in maintaining a viable connection between the transmitter and receiver was investigated as a factor of transmitter parameters. The investigation finds that a combination of switching combined with splitting of the light

between fibers is a suitable solution to provide the best trade-off between link up time and the coverage area at the receiver, and thus is a good general purpose design choice, the optical tracking system with target location information demands fewer efforts to recover and maintain the dynamic link than the one without the awareness of the receiver location information, and the high wavelength and misalignment tolerance of the receiver appear to place the greater burden on the design and control of the transmitter parameters, as the divergence and power appear to play a larger role in the performance of the control system and the resulting collected power variations at the receiver.

The work described in Chapters 3 and 4 was published in [35 - 37, 43], and the study presented in Chapters 5 and 6 was published in [11, 44 - 46].

References

[1] J.P. Dodley, D.M. Britz, D.J. Bowen, C.W. Lundgren, “Free space optical technology and distribution architecture for broadband metro and local services,” Proc. SPIE, 4214, 72-85, 2001.

[2] S. Arnon, “Optimization of urban optical wireless communication systems,” IEEE Transactions on Wireless Communications 2, 626-629, 2003.

[3] S. Arnon, S. Rotman, N.S. Kopeika, “Beam width and transmitter power adaptive to tracking system performance for free-space optical communication,” Applied Optics 6, 6095-6101, 1997.

[4] J. Wang and J. M. Kahn, “Acquisition in short-range free-space optical communication,” Optical Wireless Communications, Proc. SPIE 4873, pp. 121-132, 2002.

[5] Davis, C. C., I. I. Smolyaninov, S. D. Milner, “Flexible optical wireless links and networks”, IEEE Communications Magazine, pp. 51-57, 2003.

[6] A. Polishuk, S. Arnon, “Communication performance analysis of microsatellites using an optical phased array antenna,” Optical Engineering, 42, no. 7, pp. 2015 – 2024, 2003.

[7] J. Akella, M. Yuksel, S. Kalyanaraman, “Multi-channel communication in free-space optical networks for the last mile,” Proc. of 15th IEEE Workshop on Local and Metropolitan Area Networks, pp. 43 – 48, 2007.

[8] M. Bilgi and M. Yuksel, “Multi-element free-space-optical spherical sructures with intermittent connectivity patterns,” IEEE INFOCOM Student Workshop, Phoenix, AZ, 2008.

[9] A. Sevincer, M. Bilgi, M. Yuksel, and N. Pala, “Prototyping multi-transceiver free-space-Optical communication structures,” IEEE International Conference on Communications, Cape Town, South Africa, pp. 1-5, 2010.

[10] Zhou, D., Refai, H. H., LoPresti, P. G., Atiquzzaman, M, “Control algorithm development for mobile FSO node alignment,” IEEE/AIAA 28th Digital Avionics Systems Conference, pp. 6.A.3-1 - 6.A.3-12, 2009.

[11] Zhou, D., P. G. LoPresti, N. Brooks, H. Refai, “Evaluation of free-space optical fiber bundle transmitter configurations for receiver tracking,” Proc. SPIE, Atmospheric Propagation VI, vol. 7324, pp. 73240K-1,2009.

[12] S. Spaunhorst; P. G. LoPresti; S. Pondelik; H. Refai, “Evaluation of a novel FSO receiver for mitigating alignment errors,” Atmospheric Propagation VI, Proceedings of the SPIE, Vol. 7324, pp. 73240-H1, 2009.

[13] H. Wu, B. Hamzeh and M. Kavehrad, “Achieving carrier class availability of FSO link via a complementary RF link,” Conference Record of the Thirty-Eighth Asilomar Conference on Signals, Systems and Computers, 2, 1483-1487, 2004.

[14] S. D. Milner and C. C. Davis, “Hybrid free space optical/RF networks for tactical operations,” IEEE Military Communications Conference, vol. 1, 409-415, 2004.

[15] A. Akbulut, H. Gokhan Ilk and F. Ari, “Design, availability and reliability analysis on and experimental outdoor FSO/RF communication system,” Proceedings of the 7th International Conference on Transparent Optical Networks, vol. 1, 403-406, 2005.

[16] Wikipedia. “Synchronous optical networking”.

<http://en.wikipedia.org/wiki/SONET#Structure_of_SONET.2FSDH_signals> 24 September, 2008.

[17] International Engineering Consortium. “Synchronous Optical Network (SONET)”

<http://www.iec.org/online/tutorials/sonet/topic03.html>24 September, 2008.

[18] TechFest. “SONET/SDH Technical Summary”

<http://www.techfest.com/networking/wan/sonet.htm> 24 September, 2008.

[19] Capybara. “How does SONET work”

<http://www.capybara.org/~dfraser/gaul/CS457/A1/howworks.html>24 September, 2008

[20] Cisco. “A Brief Overview of SONET Technology”

<http://www.cisco.com/en/US/tech/tk482/tk607/technologies_tech_note09186a00800943 13.shtml#intro>24 September, 2008.

[21] Timbercon. “BER Bit Error Rate” <http://www.timbercon.com/BER-Bit-Error-Rate.html>24 September, 2008.

[22] LuxLink. “Multi-Mode versus Single-Mode Fiber”

<http://luxlink.com/faq/multi_or_single.htm>27 September, 2008.

[23] Wikipedia. “Single-mode optical fiber”

< http://en.wikipedia.org/wiki/Single-mode_optical_fiber>27 September, 2008.

[24] Integrated Publishing. “FIBER OPTIC COUPLERS”

<http://www.tpub.com/neets/tm/108-11.htm>27 September, 2008.

[25] P. G. LoPresti, H. H. Refai and J. J. Sluss, “Adaptive power and divergence to improve airborne networking and communications,” IEEE 24th Digital Avionics Systems Conference, Washington, DC, 1.B.1 - 1.1-6, 2005.

[26] A. Yariv, Optical Electronics in Modern Communications, 5th ed. Oxford U. Press, 1997.

[27] Peter G. LoPresti, Hazem Refai, “Mitigating angular misalignment from atmospheric effects in FSO links,” Atmospheric Propagation, Proc. SPIE, Vol. 6551, 65510K, 2007.

[28] P.G. LoPresti, H. Refai, J. Sluss, Jr., I. Varela-Cuadrado, “Adaptive divergence and power for improving connectivity in free space optical mobile networks,” Applied Optics, vol. 45, 25, pp. 6591-6597, 2006.

[29] P.G. LoPresti, N. Brooks, W. Sumpter, H. Refai, “Fiber bundles in transceivers to mitigate scintillation effects on free-space optical networks,” Proc. SPIE, 6551, pp. 65510K, 2007.

[30] P. G. LoPresti, C. Kiister, S. Spaunhorst; H. Refai, “Maximizing receiver misalignment tolerance in a hybrid wireless system,” Proc. SPIE, Atmospheric Propagation V, vol. 6951, 2008.

[31] Schmidt, J. D. “Numerical Simulation of Optical Wave Propagation,” SPIE Publications, Bellingham, WA, 87-92, 2010.

[32] Yu, F. T. S. “Optical Information Processing,” Wiley-Interscience, New York, NY, 148-151, 1983.

[33] S. Pondelik, P. G. LoPresti, H. Refai, “Experimental evaluation of a misalignment tolerant FSO receiver,” Proc. SPIE, vol. 78655, pp. 76850B-1 – 76850B-9, 2010.

[34] D. V. Hahn, D. M. Brown, N. W. Rolander, J. E. Sluz, R. Venkat, “Fiber optic bundle array wide field-of-view optical receiver for free space optical communications,” Optics Letters, vol. 35, no. 21, pp. 3559-3561, 2010.

[35] D. Zhou, P. G. LoPresti, H. H. Refai, “Enlargement of beam coverage in FSO mobile network,” Journal of Lightwave Technology, vol. 29, no. 10, pp. 1583-1589, 2011.

[36]P. G. LoPresti, D. Zhou, H. Refai, "Evaluation of the performance of a fiber-bundle-based optical wireless link," Proc. SPIE, vol. 8038, pp. 80380I-1 – 80380I-7, 2011.

[37]P. G. LoPresti, D. Zhou, Z. Shi, H. H. Refai, "Design simulation and analysis of a fiber-bundle based optical wireless link," Proc. SPIE vol. 8380, pp. 8380E-1-9, 2012.

[38] D. T. Wayne, R. L. Phillips, L. C. Andrews, T. Leclerc, P. Sauer, "Observation and analysis of aero-optic effects on the ORCA laser communication system," Proc. SPIE, vol. 8038, pp. 80380A-1 – 80380A-12, 2011.

[39] M. J. Vilcheck, H. R. Burris, C. I. Moore, W. R. Smith and L. M. Thomas, "Miniature lasercomm module for integration into a small, unmanned, aerial platform," Proc. SPIE, vol. 8380, pp. 8380B-1-8, 2012.

[40]A. Harris, J. J. Sluss, Jr., H. H. Refai, P. G. LoPresti, "Atmospheric turbulence effects on a wavelength diversified ground-to-UAV FSO link," Proc. SPIE, vol. 6105, 2006.

[41]A. Harris, J. J. Sluss, Jr., H. H. Refai, P. G. LoPresti, "Free-space optical wavelength diversity scheme for fog mitigation in a ground-to-unmanned-aerial-vehicle communications link," Optical Engineering, vol. 45, n. 8, p. 86001-1-12, 2006.

[42] Walther, F. G., Nowak, S. M., Parenti, R., Roth, J., Taylor, J., Wilcox, W., Murphy, R., Greco, J., Peters, J., Williams, T., Henion, S., Magliocco, R., Miller, T., Volpicelli, A., "Air-to-ground lasercom system demonstration," MILCOM, 2295 – 2301, 2010.

[43] D. Zhou, P. G. LoPresti, H. H. Refai, "Design Analysis of Fiber-bundle-based Mobile FSO Link with Wavelength Diversity," Applied Optics, Vol. 52, pp. 3689-3697, 2013.

[44] D. Zhou, P. G. LoPresti and H. Refai, "Evaluation of a control algorithm for mobile FSO node alignment", in Proc. SPIE, Atmospheric Propagation VIII, vol. 8038, , pp. 80380E-80380E-7, 2011.

[45] D. Zhou, P. G. LoPresti, H. H. Refai, "Evaluation of Fiber-bundle Based Transmitter Configurations with Alignment Control Algorithm for Mobile FSO Nodes," IEEE Journal of Lightwave Technology, vol. 31, pp. 249-256, 2013.

[46] D. Zhou, P. G. LoPresti and H. Refai, "Multi-wavelength operation of a control algorithm for mobile FSO node alignment ", in Proc. SPIE, Atmospheric Propagation X, 873204, 2013.